Helios NanoLab™ DualBeam™
Combining monochromated sub-nm resolution FE-SEM technology with high-resolution FIB performance delivers the ultimate solution for the most stringent 3D materials characterization, nano-prototyping and sample preparation needs.

Titan Family
The most powerful, flexible ultra high resolution S/TEM for 2D and 3D material characterization, plus ChemiSTEM™ Technology for atomic scale elemental analysis.

Verios Family
The Verios™ is the second generation of FEI's leading XHR (extreme high resolution) SEM family. It provides sub-nanometer resolution from 1 to 30 kV and enhanced contrast needed for precise measurements on materials in advanced semiconductor manufacturing and materials science applications.

Tecnai Osiris™
A fully digital, high performance 200 kV S/TEM system designed to deliver outstanding performance in all imaging and analytical modes with significantly improved sensitivity for light elements.
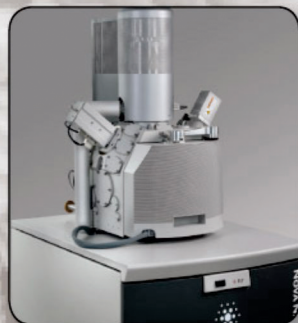
Nova™ NanoSEM Series
An ultra-high resolution FE-SEM combining very low kV imaging and analytical capabilities with unique low vacuum performance to meet your most demanding nanoscale characterization requirements.

V400ACE Focused Ion Beam (FIB)
V400ACE system incorporates the latest developments in ion column design, gas delivery and end point detection to provide fast, efficient, cost-effective editing on advanced integrated circuits. Circuit editing allows product designers to reroute conductive pathways and test the modified circuits in hours, rather than the weeks or months that would be required to generate new masks and process new wafers.

Versa 3D™ DualBeam™
Our most versatile DualBeam, with a highly configurable platform and flexible detector and analytical options providing the flexibility to work with a wide range of samples.

Vion™ Plasma FIB
FIB optics and a plasma ion source deliver highly precise, large-area, high-speed milling and material deposition to enable cross-sectioning of defects, reveal sub-surface structure and deposit materials for prototyping.

Quanta™ SEM Series
The most versatile SEM platform with high, low and ESEM™ vacuum modes for imaging and analysis of your most challenging samples next to support for in situ dynamic experiments.
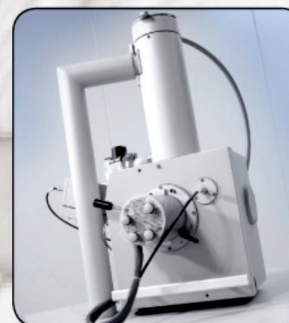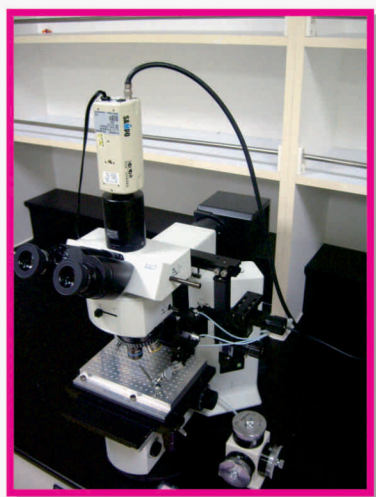
Inspect™ SEM Series
Ideal for routine characterization and inspection, this solid imaging and analytical SEM provides the flexibility and ease of use for a variety of applications, making it ideal for the multi-sample or multi-user laboratory environment.

EBT 超泰科技有限公司
E.B. TECH. CO., LTD

專業的電子顯微鏡,材料分析儀器,耗材,相關設備代理商
Electron Microscope , Analysis instruments, Sample preparation tools

FEI 高低真空場發射掃描電子顯微鏡

FISCHIONE INSTRUMENTS 離子減薄機(Ion Miller)

FEI 場發射掃描/穿透式電子顯微鏡

FISCHIONE INSTRUMENTS 電漿清淨機(Plasma Cleaner)

EBT 光學及試片吸針系統

gatan

OXFORD INSTRUMENTS

EDAX
advanced microanalysis solutions

BRUKER
Innovation with Integrity

ELECTRON MICROSCOPY SCIENCES

電子顯微鏡相關設備耗材

目 錄

台 灣 顯 微 鏡 學 會

第三十三屆學術研討會　102 年 6 月 29 日(星期六) 國立臺灣大學

08:30-09:30	報到
09:30-10:00	開幕
10:00-10:50	**RECENT INVESTIGATIONS IN MY 55-YEAR ELECTRON MICROSCOPY LIFE** Dr. Makoto Shiojiri, Professor Emeritus of Kyoto Inst. Tech
11:00-11:50	**INTRODUCTION OF NEW 120KV TEM HT7700 AND ITS APPLICATION TO BIOMEDICAL AND SOFT-MATERIAL FIELD** Dr. Taro Ogawa, Hitachi High-Technologies
12:00-13:00	第十六屆第一次台灣顯微鏡學會年會會員大會
13:00-14:00	午餐時間
	專題演講
14:00-14:30	**PROBLEMS OF TEM/EDS QUANTITATIVE ANALYSIS** BOW, Jong-Shing (鮑忠興) Center for Micro/Nano Science and Technology, National Cheng Kung University, Tainan, Taiwan
14:30-15:00	**APPLICATIONS OF SCANNING ELECTRON MICROSCOPY FOR BIOLOGICAL SAMPLES** [1]Li-Tzu Li (李莉姿),[1]Chuang-Yu Lin (林壯宇), [2]Tai-Lang Lin (林泰郎) and [2]Tzu-Han Hsu (許子涵) [1]Imaging Core Facilities, ICOB, Academia Sinica,Taipei, Taiwan [2]Instrument Center, Academia Sinica, Taipei, Taiwan
15:00-15:30	**PLASMONS DISPERSION AND NONVERTICAL INTERBAND TRANSITIONS IN SINGLE-CRYSTAL BI2SE3 INVESTIGATED BY ELECTRON ENERGY-LOSS SPECTROSCOPY** S. C. Liou (劉思謙), M. -W. Chu (朱明文), R. Sankar, F. -T. Huang (黃妃婷), G. J. Shu (殳國俊), F. C. Chou (周方正) and C. H. Chen (陳正弦) Center for Condensed Matter Sciences, National Taiwan University, Taipei, Taiwan
15:30-16:00	**ATOMIC-SCALE PROBING OF INTERDIFFUSION AND A LOCALIZED TWO-DIMENSIONAL ELECTRON DENSITY AT AN INSULATING OXIDE INTERFACE** CHANG, Ching-Pin (張景斌),[12] LIN, Jauyn Grace (林昭吟),[2] CHENG, Su-Ling (鄭淑齡),[12] YANG, Jer-Ren (楊哲人),[1] CHU, Ming-Wen (朱明文),[2] and CHEN, Cheng-Hsuan (陳正弦)[2] [1] Department of Materials Science and Engineering, National Taiwan University [2] Center for Condensed Matter Sciences, National Taiwan University
16:00-17:00	討論、頒獎、閉幕

台灣顯微鏡學會

第十六屆理、監事名錄

理 事 長	楊哲人	台灣大學材料科學與工程學系	教授
副理事長	黃玲瓏	台灣大學生命科學系	教授
常務理事	薛富盛	中興大學材料科學與工程學系	教授
	陳福榮	清華大學工程與系統科學系	教授
	劉康庭	友聯光學股份有限公司	董事長
理　　事	胡宇光	中央研究院物理研究所	研究員
	陳香君	台灣大學生命科學系	專任講師
	張　立	交通大學材料科學與工程學系	教授
	劉全璞	成功大學材料科學與工程系	教授
	陳淑華	台灣大學生命科學院	教授
	朱明文	台灣大學凝態中心	研究員
	章為皓	中央研究院化學研究所	副研究員
	謝詠芬	閎康科技股份有限公司	董事長
	蔡定平	台灣大學物理系	教授
侯補理事	李志浩	清華大學工程與系統科學系	教授
	高甫仁	陽明大學生醫光電研究所	教授
	簡萬能	中央研究院植物暨微生物學研究所	研究技師
	薛景中	中央研究院應用科學研究中心	副研究員
	孫啟光	台灣大學電機工程學系	教授
	蘇紘儀	台灣積體電路有限公司	故障分析處處長
常務監事	曾傳銘	中央研究院物理研究所	研究助技師
監　　事	羅聖全	工業技術研究院	研究員
	鮑忠興	成功大學奈米中心	教授
	張　正	國立中興大學園藝學系	副教授
	林招松	台灣大學材料科學與工程學系	教授
侯補監事	劉淦光	國家衛生研究院分子與基因醫學研究所	研究員

RECENT INVESTIGATIONS IN MY 55-YEAR ELECTRON MICROSCOPY LIFE

Makoto Shiojiri

Professor Emeritus of Kyoto Inst. Tech., 1-297 Wakiyama, Kyoto 618-0091, Japan.

I joined in an investigation on oxides for vacuum tube cathods by electron diffraction in 1958 when I was a 4th grade student of Kyoto University. Although I touched an electron microscope in an investigation on alkali antimonides[1], my main interest was X-ray diffraction. My first electron microscopy work was the identification of carbides precipitaed in steel (unpublished) in 1961. After then, I was mainly enagaged in investigations such as (1) crystallization, structure and density of amorphous films, (2) morphology and growth of metallic oxide smoke particles, (3) oxidation, iodidation and chalcogenidation of metal films, (4) crystallographic shears in reduced oxides, (5) growth of compounds in gel, (6) HRTEM image simulation and multi-color reproduction by equidensitometry and (7) anodic oxidation of Al and its resinous coating in 1962-81[2], and (8) structure of cellular and topological random systems, (9) *in-situ* observations of chemical reactions, (10) solid lubricants, (11) ceramic devices, (12) semiconducting devices with heterostructures, (13) tetrapod-like and spindle-like ZnO particles, (14) quantitative HRTEM, (15) surface structures, (16) cross-section preparation of fine particles, (17) photo-sensitive dyes on AgBr microcrystals and (18) electron energy loss spectroscopy (EELS) and energy dispersove X-ray spectrosopy (EDS) mappings in 1981-99[3]. They were studies of the structure analysis, characterization or growth of various materials and devices by means of TEM, SEM, AFM, cathodoluminescence SEM, X-ray diffraction, neutron diffraction and Auger electron spectroscopy. After my retirement from Kyoto Institute of Technology in 1999, I have been interested in HAADF-STEM[4]. Many collaborated works, in particular, on GaN-based blue light emitting diodes (LED)[4] and ZnO-based ultraviolet LED[5] have been achieved with a lot of colleagues in Taiwan. Here, I review some of our recent investigations.

I. Structural analysis of Au/TiO$_2$ thin films deposited on the glass substrate (Appl. Phys. Lett. **102**, (2013) 091603).

M. Kawasaki (JEOL US), M.J. Chen and J.R. Yang (National Taiwan Univ.) W.A. Chiou (Univ. of Maryland) and M. Shiojiri

Recently, Lin *et al*. have proposed an approach to characterize the structure of amorphous nanoscale ultrathin films using surface enhanced Raman scattering (SERS)[6]. They prepared ultrathin TiO_2 films different in thickness by atomic layer deposition (ALD) on the clean glass substrates at a temperature as low as 200ºC, and then deposited a nanostructured Au layer (~5 nm thick) on the TiO_2 surface to provide localized surface plasmon resonance and to enable SERS sensing. As a result, the intensity of the Raman spectra of these films was significantly enhanced and the structural identification of the amorphous nanoscale TiO_2 film as thin as ~2 nm was accomplished. We investigated a similar Au/TiO_2 structure, confirming the propriety of the SERS analysis and disclosing the point at issue. Cross-sectional TEM observation revealed that the Au was grown as particles, with diameter of ~15 nm or less, by Volmer-Weber growth mechanism, distributed two-dimensionally on the TiO_2 layer. The TiO_2 layer that was prepared by 417 ALD cycles using tetrakisdimethylamido titanium and H_2O precursors had a thickness of 11 nm and was amorphous. The formation of the amorphous TiO_2 at 200°C is ascribed to the glass substrate, and the growth rate as small as 0.026 nm/cycle is ascribed to the glass and amorphous TiO_2 underlayers during ALD. EDS and EELS mappings identified the Au particles, TiO_2 layer, the glass substrate and a C coating layer for reinforcing the specimen (Fig. 1). It was found that the glass substrate was common lime glass and Ca atoms migrated to TiO_2 layer (Fig. 2). The Ca atoms diffused into only an area less than a distance of a few nanometers from the substrate during the ALD at 200°C. This suggests that different TiO_2 layers in thickness have different chemical composition and structure, in particular, on its surface. This can explain the difference of the growth behavior of Au particles on different TiO_2 layers in thickness, difference which was reported by Lin *et al*.[6] It might influence the optical properties of TiO_2 layers. The selection of substrate should be careful because it influences not only structure but also purity of the deposited films even by ALD at a low temperature.

II. Structural investigation of Cr(Al)N/SiO$_x$ films prepared on Si substrates by differential pumping co-sputtering (ACS Appl. Mater. Interfaces **5**, (2013) 3833-3838)

M. Kawasaki (JEOL US), H. Takabatake and M. Nose (Univ. Toyama), I. Onishi (JEOL), and M. Shiojiri

Analytical electron microscopy revealed the structure and growth of hard coating Cr(Al)N/SiO$_x$ nanocomposite films prepared in a differential pumping co-sputtering (DPCS) system[7], which has two chambers to sputter different materials and a rotating substrate holder.

The substrate holder was heated at 250ºC and rotated at a speed as low as 1 rpm. In order to promote the adhesion between the substrate and composite film, buffer layers were deposited on a (001) Si substrate by sputtering from the CrAl target with an Ar flow and a mixture flow of Ar and N_2 (Ar/N_2) gasses, subsequently, prior to the composite film deposition (Fig. 3). Then, the Cr(Al)N/SiO$_x$ nanocomposite film was fabricated on the buffer layers by co-sputtering from the CrAl target with the Ar/N_2 gas flow and from the SiO$_2$ target with the Ar gas flow. The film had a multilayer structure of ~1.6 nm thick crystallite layers of Cr(Al)N similar to NaCl-type CrN and ~ 1 nm thick amorphous silicon oxide layers (Figs. 4 and 5). It is found that Cr(Al)N is better component than AlN for hard coating composite films, and that the fast rotation of the substrate holder makes the composite films harder. Thus, the present structural analysis has revealed the formation process of ultrathin nanocomposite films in DPCS system and disclosed some points at issue such as the formation of unexpected oxide interfaces during the low speed sustrate rotation. This helps design and fabrication of new hard coating films.

III. Photonic crystal structure and coloration of wing scales of butterflies exhibiting selective wavelength iridescence (Materials **5**, (2012) 754. Review).

F. Mika and J. Matějková-Plšková (Inst. of Scientific Instruments, Czech Rep.), S. Jiwajinda and P. Dechkrong (Kasetsart University, Thailand), and M. Shiojiri

The coloration of butterflies that exhibit human visible iridescence from violet to green has been elucidated. Highly tilted multilayers of cuticle on the ridges, which were found in the scales of male *S. charonda*[8,9] (Fig. 6b) and *E. mulciber* butterflies[10] (Fig. 6a), produce a limited-view, selective wavelength iridescence (ultraviolet (UV)~green) as a result of multiple interference between the cuticle-air layers (Figs. 7 and 8). The iridescence from *C. ataxus* (Figs. 6c and d*)* originates from multilayers in the groove plates between the ridges and ribs[11]. The interference takes place between the top and bottom surfaces of each layer and incoherently between different layers. Consequently, the male with the layers that are ~270 nm thick reflects light of UV~560 nm (green), and the female with the layers that are ~191 nm thick reflects light of UV~400 nm (violet). *T. aeacus* (Fig. 6e) does not produce the iridescent sheen which *T. magellanus* does[10]. No iridescent sheen is ascribed to microrib layers, which are perpendicular to the scale plane, so that they cannot reflect any backscattering. The structures of these butterflies would provide us helpful hints to manipulate light in photoelectric devices, such as blue or UV LEDs.

IV. *In Situ* study of live specimens in an environmental scanning electron microscope

(Microsco. Micranal. Published online: 02 May 2013)

E. Tihlaříková and V.Neděla (Inst. of Scientific Instruments, Czech Rep.) and M Shiojiri

Observation of biological alive samples was one of the biggest dreams of electron microscopy. The fundamental part of our environmental SEM (ESEM), AQUASEM II is a conventional high vacuum SEM, Tescan VEGA[12]. It has an original differentially-pumped chamber which can be evacuated very slowly and hence gently to the sample. It has also a specific detection system that consists of four detectors. The first part of the detection system is a new scintillation secondary electron (SE) detector, which works continuously in conditions both of SEM and ESEM (gas pressure from 0.001 Pa up to 1000 Pa). The second part comprises three integrated detectors; one scintillation backscattered SE (BSE) detector and two ionization SE detectors (Fig. 9). The BSE detector consists of a $YAG:Ce^{3+}$ scintillation single crystal[13], which has a small hole in its center used as a second pressure-limiting aperture for the differentially-pumped chamber. A newly patented ionization SE detector with an electrostatic separator (ISEDS)[14] uses a biased indium tin oxide electrode sputtered on the $YAG:Ce^{3+}$ crystal of the BSE detector. This electrode works as the detection electrode of the second detector[15]. High pressure of gas in the specimen chamber causes unwanted primary electron beam diffusion but supports gas ionization cascade amplification of the signal of SEs, which are accelerated by an applied field of the detection electrode of ISEDS. The third detector is also an ISEDS, which is a segmented detection ring electrode with a positive bias from 100 to 400 V and placed at the same height as the sample holder. A retarding electrode above the sample and a cylindrical separation electrode between the specimen holder and the ring electrode generate electrostatic field deflecting SEs towards the detection ring electrode, where they land on its inner or outer segment according to their energy and the intensity of the deflection field. The weak electrostatic field does not influence the BSEs emitted from the specimen with higher energy. In addition the AQUASEM-II is equipped with a sophisticated device for measuring water vapor pressure in the specimen chamber and temperature on the sample, a Peltier stage for cooling of wet biological specimens and an originally designed vapor flow control system. A sample of stored-product mite was redeployed with water from dam near Brno. We have recorded the moving of the mite alive for ~5 min at a vapor pressure of 950 Pa at 7°C (Fig. 10). Monte Carlo simulation for the scattering of the incident electron (20 kV) in thin water layers was performed. Our results demonstrate that this microscope is well applicable to *in-situ* observations of natural

structure of biological or organic samples in wet modes, noncoated surfaces of materials such as semiconductors or oxides, growth or reaction processes of nanoparticles in solution, *etc*.

I would like to acknowledge great contributions of my collaborators who were not only coauthors of our papers cited in this article but also coauthors of all our papers cited in the reviews 2-5.

1. J. Chikawa, S. Imamura, K. Tanaka, and M. Shiojiri, J. Phys. Soc. Jpn. **16**, (1961) 1175.

2. M. Shiojiri, C Kaito, Y. Saito, T. Miyana, S. Sekimoto, and K. Fujita, Mem. Fac. Indust. Arts, Kyoto Tech. Univ. **30**, (1981) 14 (review).

3. M, Shiojiri, H. Saijo, T. Isshiki, and K. Nishio, Mem. Fac. Engin. Design, Kyoto Inst. Tech. **47,** (1999) 67 (review).

4. M. Shiojiri, Chiang Mai J. Sci. **35**(3), (2008) 495 (review).

5. M. J. Chen, J. R. Yang, and Makoto Shiojiri, Semicond. Sci. Technol. **27**, (2012) 074005 (review).

6. M. C. Lin, L. W. Nien, C. H. Chen, C. W. Lee, and M. J. Chen, Appl.Phys. Lett. **101**, 023112 (2012).

7. M. Nose, T. Kurimoto, A. Saiki, K. Matsuda, and K. Terayama, J. Vac. Sci. Technol. A, **30**, (2012) 011502.

8. J. Matějková-Plskova, S. Shiojiri and M. Shiojiri, J. Microsc. **236,** (2009) 88.

9. J. Matějková-Plšková, D. Jančik, M. Mašláň, S. Shiojiri, and M. Shiojiri, Mater. Trans. **51**, (2010) 202.

10. P. Dechkrong, S. Jiwajinda, P. Dokchan, M. Kongtungmon, N. Chomsaeng, T. Chairuangsri, C.C. Yu, C.N. Hsiao and M. Shiojiri, J. Structural Biology, **176** (2011) 75.

11. J. Matějková-Plšková, F. Mika, S. Shiojiri, and M. Shiojiri, Mater. Trans. **52**, (2011) 297.

12. V. Neděla, J. Microsc. **237**, (2010) 7.

13. R. Autrata, P. Schauer, J. Kvapil, and J. Kvapil, J. Phys. E: Sci. Instrum. **11**, (1978) 707.

14. V. Neděla and J. Jirák, Patent EP 2195822 (Czech Patent No. 299864).

15. V. Neděla, I. Konvalina, B. Lencová, and J. Zlámal, Nucl. Instrum. Methods Phys. Res. A **645**, (2011) 79.
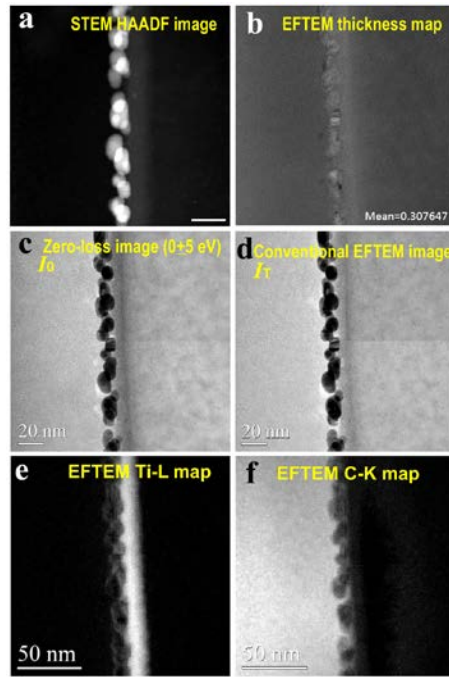
Fig. 1. EFTEM of Au/TiO$_2$ structure. (a) STEM HAADF image. (b) EFTEM thickness map. (c) Zero-loss image. (d) Conventional EFTEM image (e) EFTEM Ti-L map. (f) EFTEM C-K map.
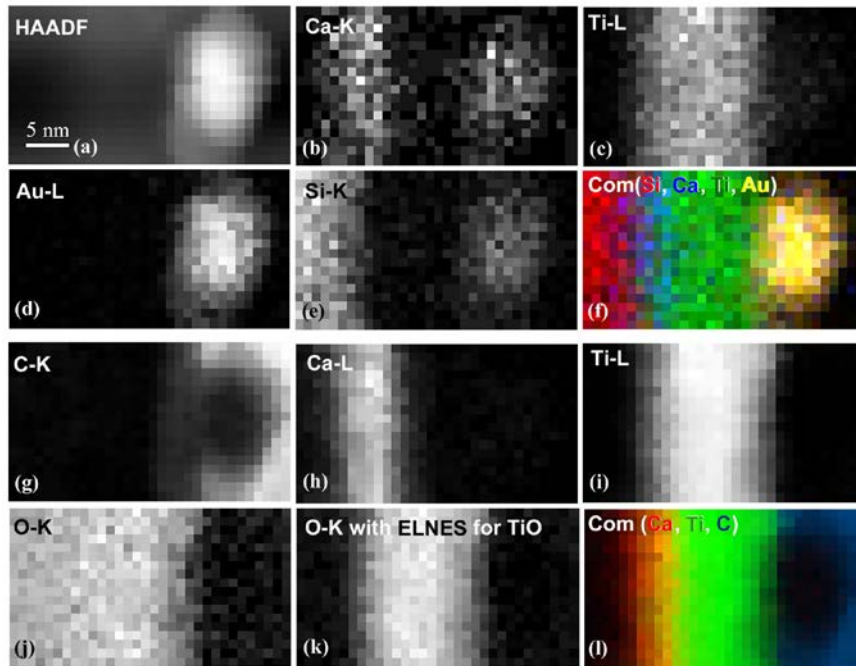

Fig. 2. EDS and EELS mapping of Au/TiO$_2$ structure. (a) HAADF image. (b)–(e) EDS maps of Ca-K, Ti-L, Au-L, and Si-K, respectively. (g) Composite EDS map (Si:red, Ca:blue, Ti:green, and Au:yellow). (g)-(j) EELS maps of C-K, Ca-L, Ti-L, and O-K, respectively. (k) O-K map with energy-loss near-edge structure for Ti-O. (l) Composite EELS map (Ca:red, Ti:green, and C:blue).
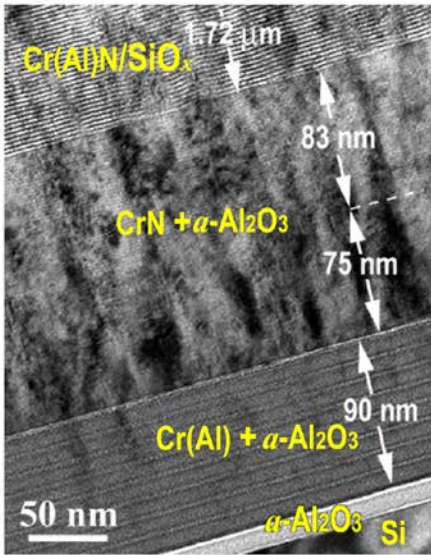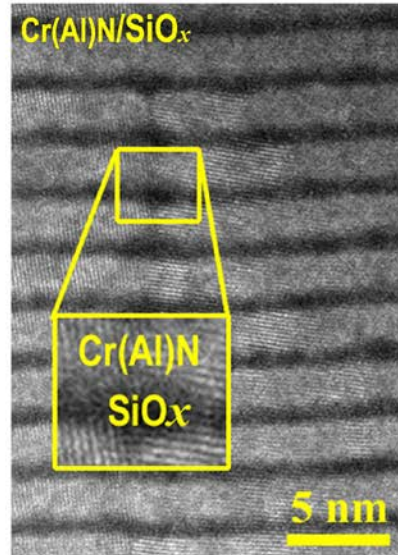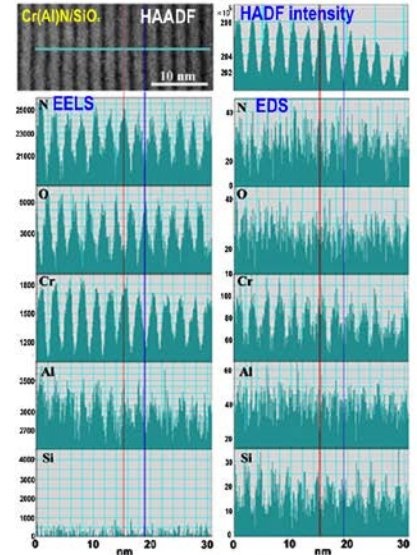
Fig. 3   Fig. 4   Fig. 5

Fig. 3. HR-TEM image of multilayers sputter-deposited from CrAl and SiO_2.targets under different conditions.

Fig. 4. HR STEM-HAADF image of a Cr(Al)N/SiO_x.nano-composite layer.

Fig. 5 STEM-HAADF image, EELS and EDS line profiles in the Cr(Al)N/SiO_x.nano-composite layer.
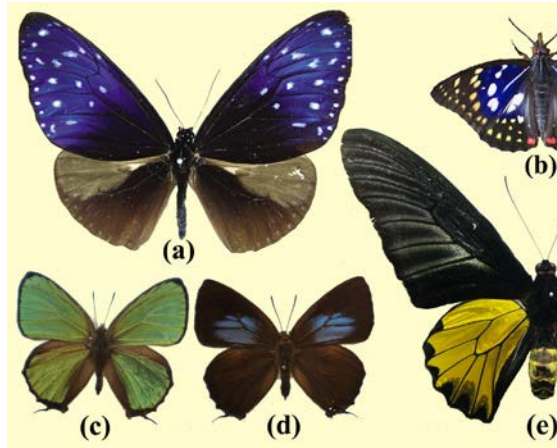

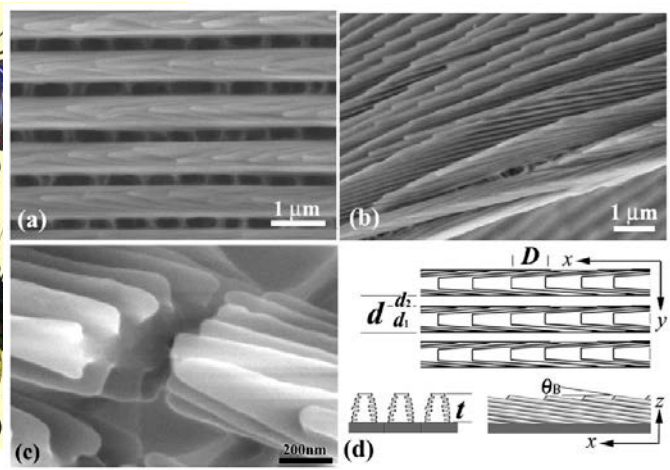
Fig. 6   Fig. 7

Fig. 6. Various butterflies (a) Male *E. mulciber*; (b) Male *S. charonda*; (c) Male *C. ataxus*; (d) Female *C. ataxus*; (e) Male *T. aeacus*.

Fig. 7. SEM images of ridges in a blue-iridescent scale in *Sasakia Charonda* butterfly. (a) The top surfaces of the ridges. (b, c) The top and side surfaces of the cuticles on the ridges. (d) Schematic of the piled cuticles.
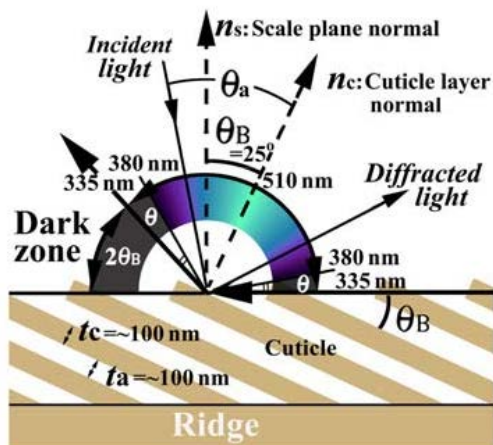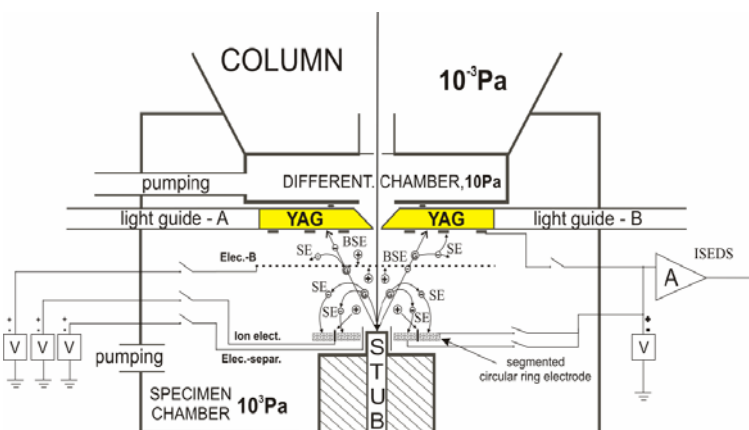
Fig. 8　　　　　　　　　　　　　　　　　　Fig. 9

Fig. 8. Schematic illustration of the selective reflection from cuticle layers piled on the ridge.

Fig. 9. Three integrated detectors (one scintillation BSE detector and two ionization SE detectors) in our ESEM.
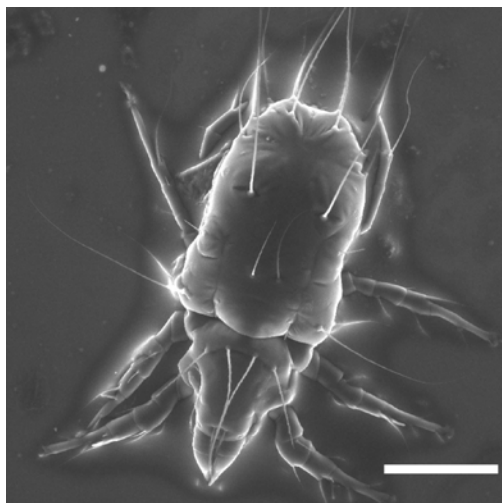

Fig. 10　(Scale: 0.1 mm)

Fig. 10. A still ESEM image of a living mite, whose movement in water was recorded.

INTRODUCTION OF NEW 120KV TEM HT7700 AND ITS APPLICATION TO BIOMEDICAL AND SOFT-MATERIAL FIELD

Taro Ogawa

Marketing Dept. 2, Science Systems Sales & Marketing Div, Hitachi High-Technologies

1. Introduction

The transmission electron microscope (TEM) is a powerful tool for various fields of study.   We have developed the HT7700 TEM having maximum accelerating voltage of 120 kV for research in fields ranging from biology to soft materials and nano-technology.   The HT7700 features an entirely new design in which the operating console and monitor are separated from the TEM main unit.   In the HT7700, a screen camera for fluorescent screen observation is integrated so that all TEM operations are available in a normally lighted room.

2. Outline and Features of the HT7700

Figure 1 shows an outer view of the HT7700 with options.   The instrument enables us to set an accelerating voltage from 40 kV to 120 kV and to vary magnification from 50x to 1000x (in Low Mag Mode) and from 200x to 600,000x (in Zoom mode).

The main features of the instrument are explained below.

(1) Adoption of a screen camera allows centralized monitoring TEM images, and observation/operation in the bright room.   The TEM image of a sample projected on the fluorescent screen is captured by the screen camera and then displayed on the monitor.   This permits the operator to conduct field search with the trackball located.

(2) We newly prepared new 8M-pix integrated CCD camera system for HT7700.   As a result, obtaining fine pixel, large field-of-view images can be possible by this new camera (Fig. 2).

(3) As an option, we prepared scanning transmission electron microscope (STEM) system.   This supports high-resolution STEM observations and high-definition image recording (up to 5.120×3.840 pixels). The unit can be used for observation of sectioned samples with a thickness of 1 μm, and combined with energy-dispersive X-ray spectrometry (EDX) to produce element maps.

(4) As an option, we prepared high-resolution objective lens (EXALENS) with low spherical aberration.   This achieves a lattice resolution of 0.144 nm for an acceleration voltage of 120 kV and provides high-contrast, high-resolution observations with low damage at a low acceleration voltage.

In the presentation, application data by above functions for biomedical and soft-material field will also be shown.

Fig. 1 The HT7700 TEM (with options)

Specimen : Rat sciatic nerve (no stain)
Vacc : 80 kV
Magnification : x 6,000

500 nm

Fig. 2 TEM image by 8M-pix camera (high contrast image is obtained without staining specimen by using high-contrast(HC) mode)

Oral-01
PROBLEMS OF TEM/EDS QUANTITATIVE ANALYSIS

BOW, Jong-Shing(鮑忠興)

Center for Micro/Nano Science and Technology, National Cheng Kung University, Tainan, Taiwan

An EDS, equipped in a TEM/STEM, is an analysis tool of easy operation and offers high spatial resolution chemical information down to several nano-meters scale.   However, for most of cases, the convenience of composition analysis is limited in qualitative analysis only. Once quantitative analysis is required, rare people can guarantee the accuracy of the results. The reason comes from several factors which will be discussed in this presentation. The first one comes to the low energy resolution, around 134 eV, of EDS. This shortage causes many overlaps to occur in cases. When energy peaks of elements involved overlap, it is hard to tell the composition within 10% accuracy unless a very powerful EDS processing software is used or a suitable database is established. Figure 1 illustrates an extremely typical case, EDS analysis of CrOx, where O Kα peak (@ 525 eV) and Cr Lα (@ 573 eV) peak overlap completely. The second factor is spurious electrons and X-rays, which come from C2 aperture and/or pole piece. This will induce unexpected elements in the spectrum and increase the error percentage in composition calculation.

Then comes to the atomic scattering of the sample itself. The situation becomes more serious whenever elements of high z are concerned. Figure 2 illustrates an EDS analysis of a thin film material. The probe size and collection time are same for all layers. It is very obvious that both background and Cu signals in the EDS spectrum of the Pt layer are much higher than those of the Al layer. More data of this thin film material will be discussed in the presentation. Hundreds of similar EDS analyses all pointed to the same direction: TEM/EDS quantitative analysis of thin film materials, especially for those of less than 10 nm and heavy elements involved, is a very hard work due to the effect of atomic scattering.

References
1. David B. Williams and C. Barry Carter, Transmission Electron Microscopy, Microscopy, vol.IV, Spectrometry, Plenum Press, New York (1996) 599-620。
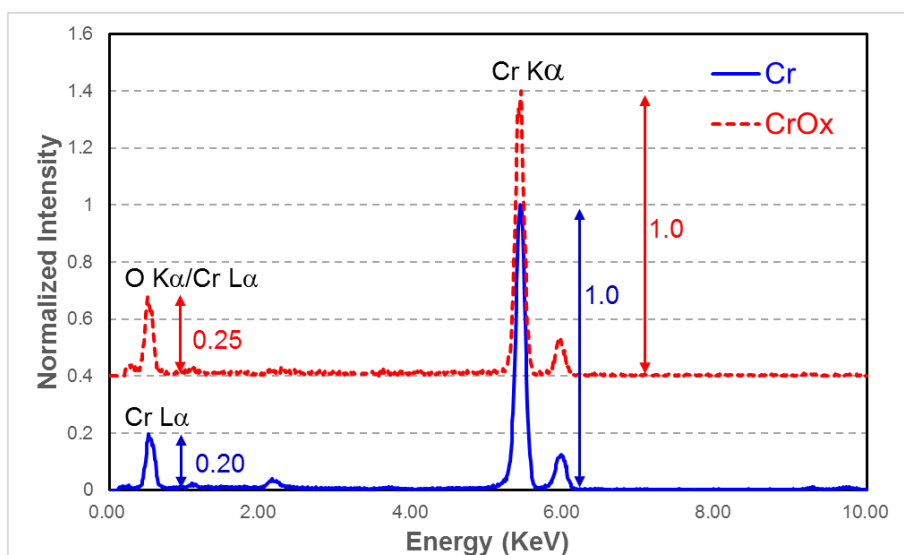
Figure 1 EDS spectra of Cr (solid line) and CrOx(dash line). The concentration of oxygen in the sample CrOx is hard to calculated due to the overlap of O Kα peak and Cr Lα peak.
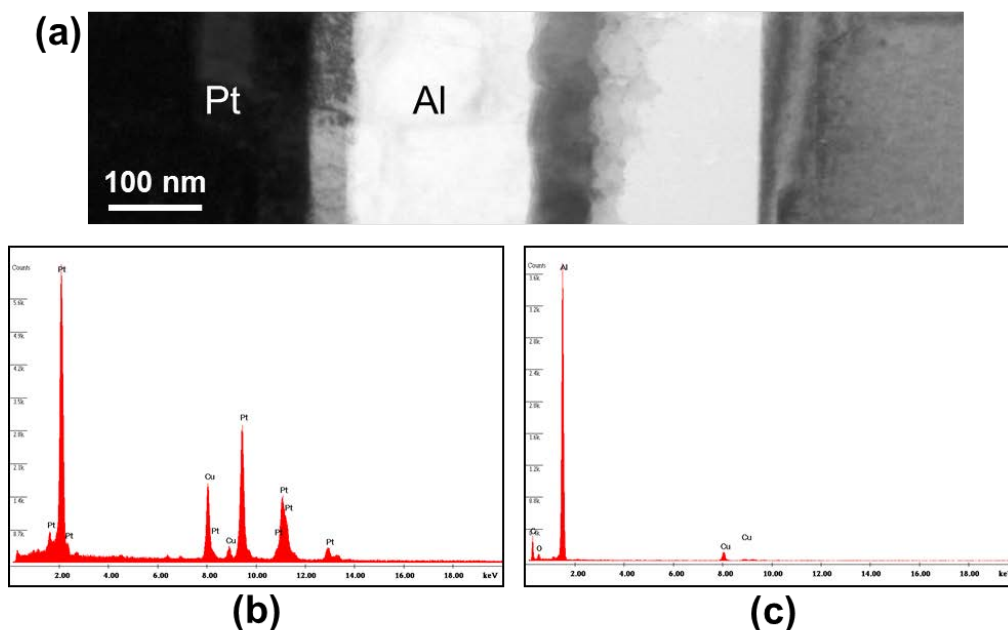

Figure 2 Effect of atomic scatterin in EDS analysis of thin film materials. (a)BF image; (b)EDS spectrum from Pt layer; (c)EDS spectrum from Al layer. The EDS spectrum of Pt layer has higher both background and Cu signals. The former comes to Bremsstrahlung effect and the later is generated from the Cu grid used to hold the TEM sample.

Oral-02

APPLICATIONS OF SCANNING ELECTRON MICROSCOPY FOR BIOLOGICAL SAMPLES

[1]Li-Tzu Li(李莉姿),[1]Chuang-Yu Lin(林壯宇), [2]Tai-Lang Lin(林泰郎) and [2]Tzu-Han Hsu (許子涵)

[1]Imaging Core Facilities, ICOB, Academia Sinica,Taipei, Taiwan
[2]Instrument Center, Academia Sinica, Taipei, Taiwan

Cells are basic units of living organisms of which the major component is water. Three characteristics of living organisms including mostly hydrated, non-electronically conductive and pressure and temperature sensitive make them difficult to observe in an SEM without sample preparation procedures. However, one standard protocol can not fit the great varieties of biological samples, not to mention the specimen with heterogeneous properties. Dehydration and critical point dry in standard sample preparation devastate very hydrated or fragile samples. Without electronic conductivity, only can low vacuum and environmental modes of SEM provide chances to visualize such samples with minimal or even without any preparation by controlling parameters as pressure, accelerating voltage and vapor. The morphology can then be kept as close to the native status of the sample. Different combinations of biological samples with different processing procedures, immunogold labeling and EDX applications were demonstrated.

References
1. J. J. Bozzola and L. D. Russell, 1992

Figure 1. Viewing an ant with gold coating only with high vacuum mode.
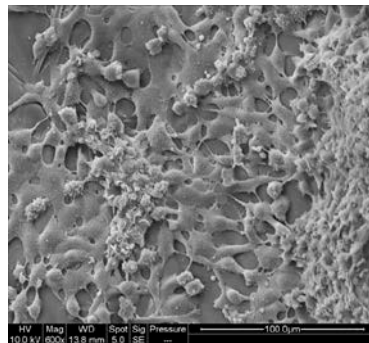

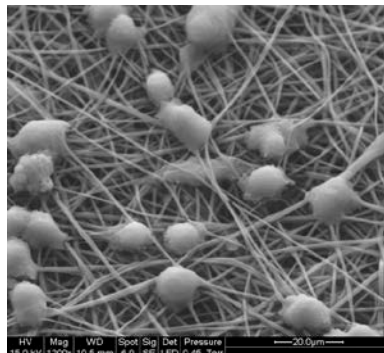Figure 2. Cultured cells viewed by low vacuum mode.

Figure 3. Nanofibers with cultured cells in low vacuum mode

Figure 4. Sex comb of Drosophila in ESEM mode

PLASMONS DISPERSION AND NONVERTICAL INTERBAND TRANSITIONS IN SINGLE-CRYSTAL BI$_2$SE$_3$ INVESTIGATED BY ELECTRON ENERGY-LOSS SPECTROSCOPY

S. C. Liou (劉思謙), M. -W. Chu (朱明文), R. Sankar, F. -T. Huang (黃妃婷)

G. J. Shu (夊國俊), F. C. Chou (周方正) and C. H. Chen (陳正弦)

Center for Condensed Matter Sciences, National Taiwan University, Taipei, Taiwan

Plasmons dispersion and nonvertical interband transitions in Bi$_2$Se$_3$ single crystals were investigated by electron energy-loss spectroscopy in conjunction with (scanning) transmission electron microscopy, (S)TEM-EELS. Both volume plasmons (π plasmon at 7 eV and $\pi+\sigma$ plasmon at 17 eV) and surface plasmons (~5.5 and 10 eV) were demonstrated in STEM-EELS spectra and the corresponding spectral imaging in real space [1]. In the further EELS experiments in reciprocal space, the momentum-dependent spectra reveal very different dispersion behavior between π and $\pi+\sigma$ plasmons, with $\pi+\sigma$ plasmons showing a typical quadratic dependence whereas the π plasmon exhibiting a linear dispersion analogous to what was reported for graphene. Furthermore, a low energy excitation 0.7~1.6 eV was also observed which is attributed to direct nonvertical interband transitions along the ΓF direction [2].

References

1.   S. C. Liou et al., *Phys. Rev. B* 87, 085126 (2013).
2.   S. K. Mishra et al., *J. Phys.:Condens. Matter* 9 (1997) 461.
3.   This research was supported by National Science Council of Taiwan (NSC99-2112-M-002-027-MY3 and NSC101-2811-M-002-130).
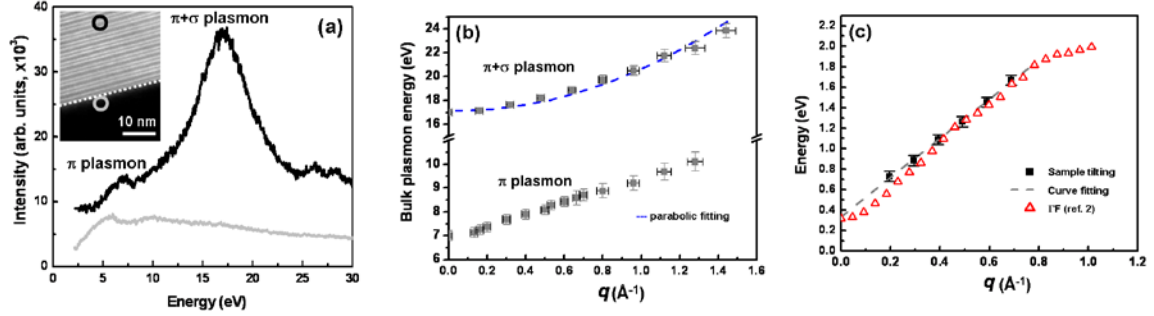
FIG. 1. (a) STEM–EELS spectra acquired on single-crystal Bi$_2$Se$_3$ with the electron probe positioned at the material interior and sample edge (inset HAADF image). (b) The energy of π and $\pi+\sigma$ plasmons as a function as momentum transfer (q), respectively. (c) The dispersion curve of the nonvertical intenband transition peaks as a function of momentum-transfer with sample tilting (marked with black square, respectively). The dashed line is the linear curve fitting. The dispersion of the lowest conduction band along ΓF direction in ref. 2 with energy normalized to the experimental value of energy gap (E$_g$= 0.32 eV) at q= 0 is also plotted for comparison.

ATOMIC-SCALE PROBING OF INTERDIFFUSION AND A LOCALIZED TWO-DIMENSIONAL ELECTRON DENSITY AT AN INSULATING OXIDE INTERFACE

CHANG, Ching-Pin(張景斌),[12] LIN, Jauyn Grace(林昭吟),[2] CHENG, Su-Ling(鄭淑齡),[12] YANG, Jer-Ren(楊哲人),[1] CHU, Ming-Wen(朱明文),[2] and CHEN, Cheng-Hsuan(陳正弦)[2]

[1] Department of Materials Science and Engineering, National Taiwan University, Taipei, Taiwan

[2] Center for Condensed Matter Sciences, National Taiwan University, Taipei 106, Taiwan

Upon joining the non-polar TiO_2 plane of $SrTiO_3$ with the polar atomic plane of an insulating oxide, the heterojunction interface could become metallic. The context of this exotic physics has been known as electronic reconstruction and largely described by the charge transfer from the polar to non-polar planes, forming interfacial two-dimensional electron gas. We explored this wisdom through mixed-valence $(Nd_{0.35}Sr_{0.65})MnO_3$ on TiO_2-terminated $SrTiO_3$, manifesting a primitively polar-discontinuous $(Nd_{0.35}Sr_{0.65}O)^{0.35+}$-$(TiO_2)^0$ interface, while being electrically insulating. Using atomic-plane-by-atomic-plane chemical quantifications and spectroscopy in an aberration-corrected electron microscope, unexpectedly charge transfer across the insulating interface does exist, whereas inversely into $(Nd_{0.35}Sr_{0.65})MnO_3$. The intricate electronic correlations and interfacial strain envisaged by $(Nd_{0.35}Sr_{0.65})MnO_3$ drive the charges otherwise localized, leading to a counter-intuitive inverse charge transfer with an insulating character, in distinct contrast to the electronic-reconstruction framework. Correlations physics underlining this unexpected inverse electronic reconstruction were atomically tackled with new interface-property perspectives.

B-P-01	**THE ANATOMICAL STUDY ON GROWTH DYNAMIC OF CAMBIAL ZONE OF TAIWAN SPRUCE (*PICEA MORRISONICOLA* HAYATA) BY PINNING AND INTACT TISSUE SAMPLING METHODS** [1]Yu-Ming Chang (張育銘) , [1]Biing T. Guan (關秉宗) [2]Ling-Long Kuo-Huang (黃玲瓏) [1] School of Forestry and Resource Conservation, National Taiwan University [2] Institute of Ecology and Evolutionary Biology, National Taiwan University, Taipei, Taiwan
B-P-02	**THREE DIMENSIONAL STRUCTURE OF NATIVE OLIGOMERIC SPROUTY2 DETERMINED BY ELECTRON MICROSCOPY AND ITS ELECTROCONDUCTIVITY** [1]LIU, Bang-Hung (劉邦弘), [1,2]CHEN, Feng-Jung (陳豐榮), [1]LAI, Chun-Chieh (賴俊傑), [1]LEE, Kuan-Wei (李冠緯), [3]LEE, Sue-Ping Lee (李淑萍), [1]SHEN, Hsiao-Hsuian (沈曉瑄), [1]TSAI, Hsieh-Chin (蔡協晉), [3]TSAI, Shu-Ping (蔡淑萍) and [1]LIOU, Gunn-Guang (劉淦光) [1]Institute of Molecular and Genomic Medicine, National Health Research Institutes, Miaoli, Taiwan [2]Department of Photonics & Institute of Electro-Optical Engineering, National Chiao Tung University, Hsinchu, Taiwan [3]Insitute of Molecular Biology, Academia Sinica, Taipei, Taiwan
B-P-03	**BIZONOPLAST: A NOVEL GIANT CHLOROPLAST ADAPTED TO LOW LIGHT WITH DIFFERENTIAL PHOTOSYNTHETIC FUNCTIONING IN ITS DIMORPHIC ULTRASTRUCTURE** [1]SHEUE, Chiou-Rong (許秋容), [2]WU, Yeh-Hua (吳業華), [1,3]CHESSON, Peter, [4]JANE, Wann-Neng (簡萬能), CHEN[5], Shiang-Jiuun (陳香君), KUO-HUANG[6], Ling-Long (黃玲瓏) and [7]KU, Maurice S. B. (古森本) [1]Department of Life Sciences, National Chung Hsing University, Taichung, Taiwan [2]Institute of Biological Resources, National Chiayi University, Chiayi, Taiwan [3]Ecology & Evolutionary Biology, University of Arizona, USA [4]Electron Microscopy Lab, Institute of Botany, Academia Sinica, Taipei, Taiwan [5]Biology and TechComm-5, National Taiwan University, Taipei, Taiwan [6]Institute of Ecology and Evolutionary Biology, National Taiwan University [7]Institute of Bioagricultural Science, National Chiayi University, Chiayi, Taiwan

B-P-04	**INCIDENCE AND MICROSTRUCTURAL COMPARISON OF GALLS INDUCED BY *LEPTOCYBE INVASA* ON LEAVES OF THREE SPECIES OF *EUCALYPTUS* TREES**
	SHIH, Cheng-Kai (石承凱) and LIAO, Gwo-Ing（廖國媖）
	Department of Life Sciences, National Cheng Kung University, Tainan, Taiwan
B-P-05	**COMPARATIVE MORPHOLOGY AND ANATOMY OF FIVE TYPES OF CECIDOMYIID LEAF GALLS ON *MACHILUS ZUIHOENSIS* HAYATA (LAURACEAE)**
	SU, Chi-Hao (蘇棨豪) and LIAO, Gwo-Ing (廖國媖)
	Department of Life Sciences, National Cheng Kung University, Tainan, Taiwan

B-P-01

THE ANATOMICAL STUDY ON GROWTH DYNAMIC OF CAMBIAL ZONE OF TAIWAN SPRUCE (*PICEA MORRISONICOLA* HAYATA) BY PINNING AND INTACT TISSUE SAMPLING METHODS

[1]Yu-Ming Chang（張育銘）, [1]Biing T. Guan（關秉宗）, [2]Ling-Long Kuo-Huang（黃玲瓏）

[1] School of Forestry and Resource Conservation, National Taiwan University
[2] Institute of Ecol. and Evol. Biology; Depart. of Life Science, National Taiwan University

Growth dynamic of cambial zone was studied at tissue level in Taiwan spruce (*Picea. morrisonicola*) located at the Tataka long-term monitoring site in central Taiwan in 2011 and 2012. Xylem radial growth was determined by pinning method (wounding the cambium with an insect needle and then tracing the location of wound cambium during the growth season) (Figs. 1, 2), and intact tissue method (extracting a small tissue block monthly) (Fig. 3).

The pinning method induced necrosis of vascular cambial cells and then formed the callus tissue and the traumatic resin ducts (Fig. 2). The callus was a reliable marker for defining the secondary xylem increment since the time of inserting, but the traumatic resin duct was not. The series of cross sections obtained near the center of pinning site were used to identify and count the layers of xylem cells before and after inserting (Fig. 2). The intact tissue method enabled us relatively easy and unambiguous to define the onset and cessation of xylogenesis (Fig. 3). The results showed that both methods can help us to trace the cambium growth dynamic. However, the intact tissue method was superior for precise study of the cambial activity and the various developmental stages of the secondary xylem tissues.
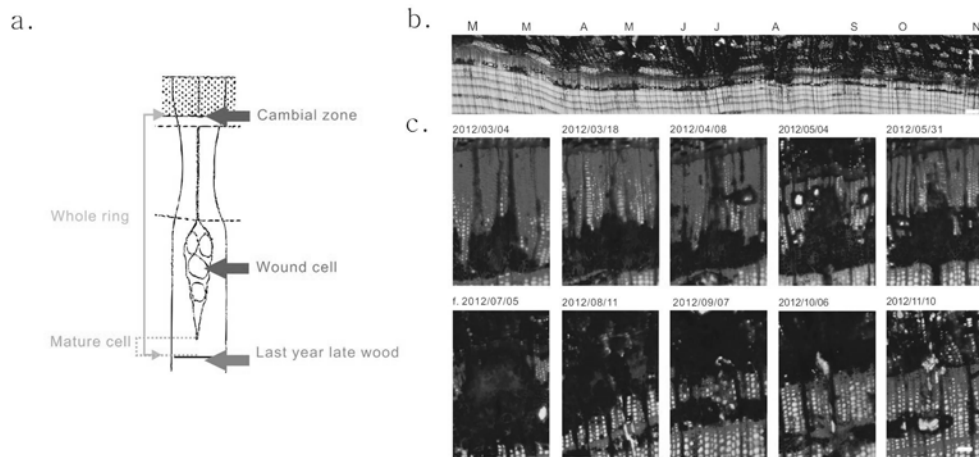
Figure 1. Cross sections showing the monthly dynamic of callus formation from the sample in 2012 by pinning method.   Scale bar: b, 1 mm ; c, 100 μm.
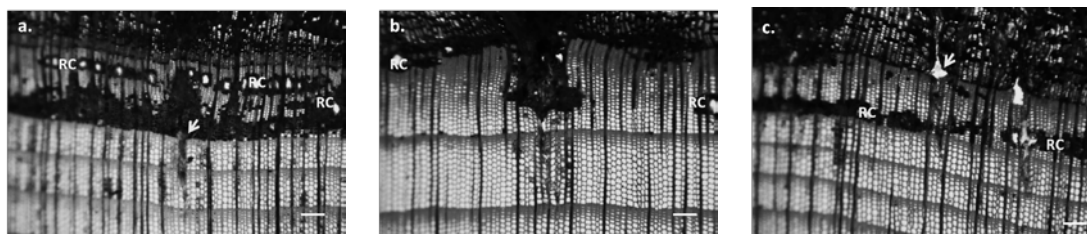

Figure 2. Cross sections by pinning method. a, showing the location of inserting before the growth season. b, showing the location of inserting in the growth season. c, showing the inserting in cessation stage. RC: resin duct. Arrow: center of pinning. Scale bar: 200 μm.
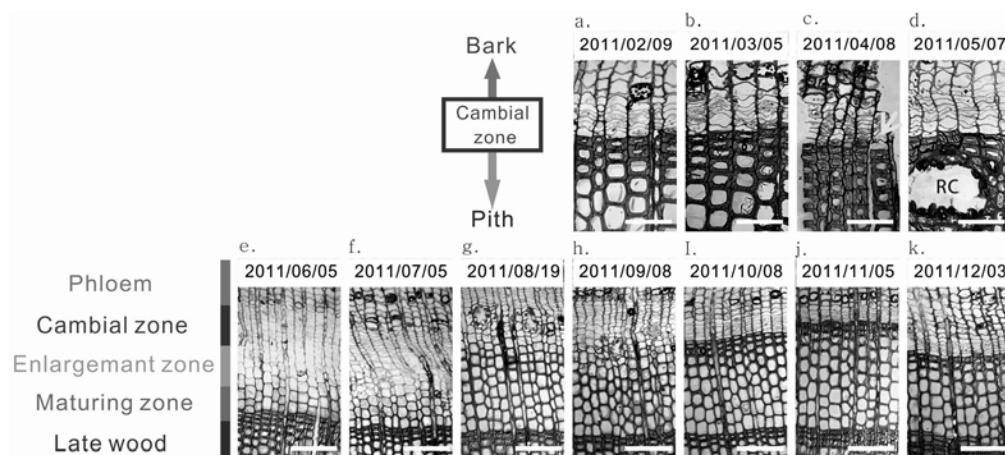

Figure 3. Intra-annual wood formation dynamic monthly in 2011by the intact tissue method. Yellow arrow indicating the cell plate during cell dividing. RC: Resin duct. Scale bar: a-d, 100 μm; e-k, 200 μm.

THREE DIMENSIONAL STRUCTURE OF NATIVE OLIGOMERIC SPROUTY2 DETERMINED BY ELECTRON MICROSCOPY AND ITS ELECTROCONDUCTIVITY

[1]LIU, Bang-Hung (劉邦弘), [1,2]CHEN, Feng-Jung (陳豐榮), [1]LAI, Chun-Chieh (賴俊傑), [1]LEE, Kuan-Wei (李冠緯), [3]LEE, Sue-Ping Lee (李淑萍), [1]SHEN, Hsiao-Hsuian (沈曉瑄), [1]TSAI, Hsieh-Chin (蔡協晉), [3]TSAI, Shu-Ping (蔡淑萍) and [1]LIOU, Gunn-Guang (劉淦光)

[1]Institute of Molecular and Genomic Medicine, National Health Research Institutes, Miaoli, Taiwan
[2]Department of Photonics & Institute of Electro-Optical Engineering, National Chiao Tung University, Hsinchu, Taiwan
[3]Insitute of Molecular Biology, Academia Sinica, Taipei, Taiwan

Receptor tyrosine kinases (RTKs) regulate many fundamental cellular processes, including apoptosis, chemotaxis, differentiation, migration, proliferation and survival. Sprouty2 (Spry2) is known as an important regulator of RTK signaling pathways. Therefore, the property of Spry2 is worth to be investigated more. In this study, we find that Spry2 is able to self-assemble into oligomers with a high affinity KD value of approximate 16 nM, using BIAcore surface plasmon resonance analysis. The three dimensional (3D) structure of Spry2 looks like a donuts shaped with two lip-covers, solved by electron microscopy (EM) single particle reconstruction approach. Furthermore, using energy dispersive spectrum of EM and total reflection X-ray fluorescence (TXRF) methods to analyze the elements carried by Spry2, it is demonstrated that Spry2 is a silicon and iron containing protein. The silicon may contribute for the electroconductivity of Spry2. And the electroconductivity of Spry2 exhibits concentration-dependent feature. This first report of silicon and iron containing protein and its 3D structure may provide a hint to allow us to (1) study the potential mechanism of switching electronic transfer on or off for controlling the signal transduction and (2) develop a new type of conductor or even semiconductor using biological or half-biological hybrid materials in the future.
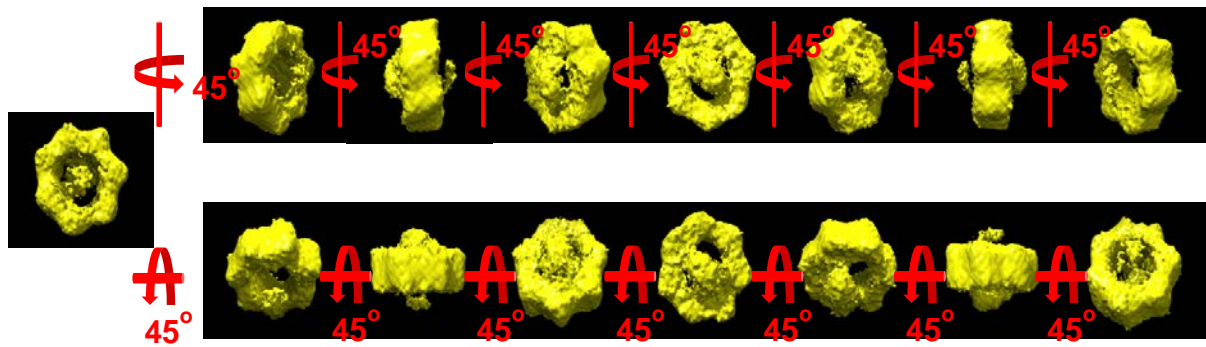
Figure 1. Different views of representative 3D reconstruction model of Spry2. The estimated resolution of the reconstitution density map is 25 Å according to the Fourier shell correlation = 0.5 criterion. The overall dimensions of donut-like part has an apparent thickness of approximately 4.2 nm, an internal diameter approximately 5.0 nm and external diameters approximately 13.4 and 10.0 nm, measured from two vertices or close points of the lobs, respectively.

BIZONOPLAST: A NOVEL GIANT CHLOROPLAST ADAPTED TO LOW LIGHT WITH DIFFERENTIAL PHOTOSYNTHETIC FUNCTIONING IN ITS DIMORPHIC ULTRASTRUCTURE

[1]SHEUE, Chiou-Rong (許秋容), [2]WU, Yeh-Hua (吳業華), [1,3]CHESSON, Peter, [4]JANE, Wann-Neng (簡萬能), CHEN[5], Shiang-Jiuun (陳香君), KUO-HUANG[6], Ling-Long (黃玲瓏) and [7]KU, Maurice S. B. (古森本)

[1]Department of Life Sciences, National Chung Hsing University, Taichung, Taiwan; [2]Institute of Biological Resources, National Chiayi University, Chiayi, Taiwan; [3]Ecology & Evolutionary Biology, University of Arizona, USA; [4]Electron Microscopy Lab, Institute of Botany, Academia Sinica, Taipei, Taiwan; [5]Biology and TechComm-5, National Taiwan University, Taipei, Taiwan; [6]Institute of Ecology and Evolutionary Biology, National Taiwan University, Taipei, Taiwan; [7]Institute of Bioagricultural Science, National Chiayi University, Chiayi, Taiwan

Bizonoplasts are unique giant chloroplasts with dimorphic ultrastructure located in dorsal epidermal cells of leaves of two species of *Selaginella* adapted to deep-shade. This chloroplast is characterized by two zones: the upper zone is occupied by parallel layers of 2–4 stacked thylakoid membranes while the lower zone contains both unstacked stromal thylakoids and grana structure like the common chloroplasts of land plants. In this study, *S. erythropus* was sampled for chloroplast immunogold labeling. Quantitative immunogold labeling of four types of photosynthetic key proteins, psaA for photosystem I (PSI), psbA for photosystem II (PSII), RbcL for rubisco and AtpA for ATPase, was performed to understand photosynthetic functional differences between the upper and lower zones of a bizonoplast. The results show that these four photosynthetic key proteins occur at both upper and lower zones in a bizonoplast. Interestingly, the upper zone is significantly enriched in PSI relative to the lower zone, while the lower zone is significantly enriched in PSII and rubisco relative to the upper zone. There is no significant difference in ATPase between two zones. Based on these results, the unique bizonoplasts with dimorphic ultrastructure show differential physiological functioning in a single plastid: the concave and wide open upper zone in a cup-shaped bizonoplast equipped with layers of parallel and horizontally extended 2–4 stacked thylakoid membranes may facilitate effect area of capturing photons and helps to absorb the far-infrared light (rich in PSI, P700), while the lower zone filled with numerous grana with higher ratio of PSII (P680) and rubisco helps to absorb the infrared light and synthesize more starch grains.

References

1. C. R. Sheue et al. *American Journal of Botany* 94 (2007) 1922-1929.
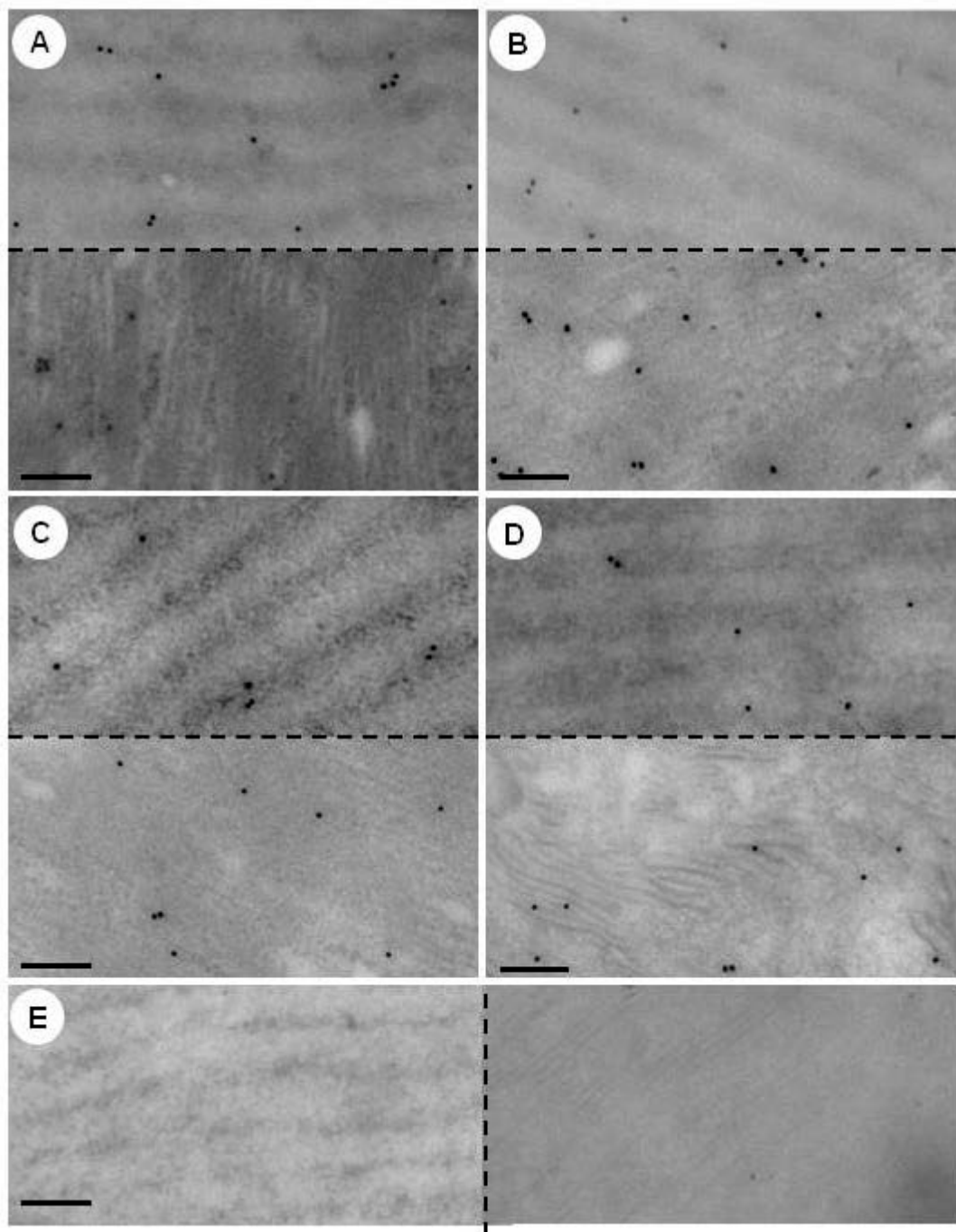
Figure 1. Paired immunogold labeling of four photosynthetic proteins of upper and lower zones of bizonoplasts of *Selaginella erythropus*. A. psaA.   B. psbA. C. rbcL. D. AtpA. E. control. All scale bars = 200 nm.

INCIDENCE AND MICROSTRUCTURAL COMPARISON OF GALLS INDUCED BY *LEPTOCYBE INVASA* ON LEAVES OF THREE SPECIES OF *EUCALYPTUS* TREES

SHIH, Cheng-Kai (石承凱) and LIAO, Gwo-Ing（廖國媖）

Department of Life Sciences, National Cheng Kung University, Tainan, Taiwan

Leptocybe invasa is an emerging pest to eucalypts plantation. After females oviposit eggs on young leaves, the gall tissue will provide nutrient and protection for larvae. There is a little known about the reason why *L. invasa* have the preference of oviposition, this research will focus on gall development and on three *Eucalyptus* trees. We recorded the oviposition sites on each young bud after female chalcids were released ten days ago, and analyzed the oviposition preference of *L. invasa*. Gall development on infected leaves was observed by microscope, compared the microstructure difference of the galls. The results indicates that: (1) highest infection rate on *E. camaldulensis* x *E. grandis* hybrid and *E. erophylla* were 50 % and 63% respectly while no any *E. camaldulensis* was infected; (2) petioles are preferred by *L. invasa* for oviposition; (3) thick cuticle layer and tannin cells might be possible reasons for higher gall abortion rate on *E. urophylla* compared with the hybrid. Epidermis structure is the first defense line against herbivores. Besides, previous studies point out metabolites like tannin can affect development of galling insects. This research describes physical and chemical qualities of infection difference of eucalypts, providing us useful information about blue gum chalcid's oviposition choice.

References

1. Kavitha Kumari, N. 2009. M.S. Thesis, University of Agricultural Sciences, Dharwad, India.
2. Mendel, Z., A. Protasov, N. Fisher, and J. La Salle. 2004. *Australian Journal of Entomology* 43(2): 101-113.
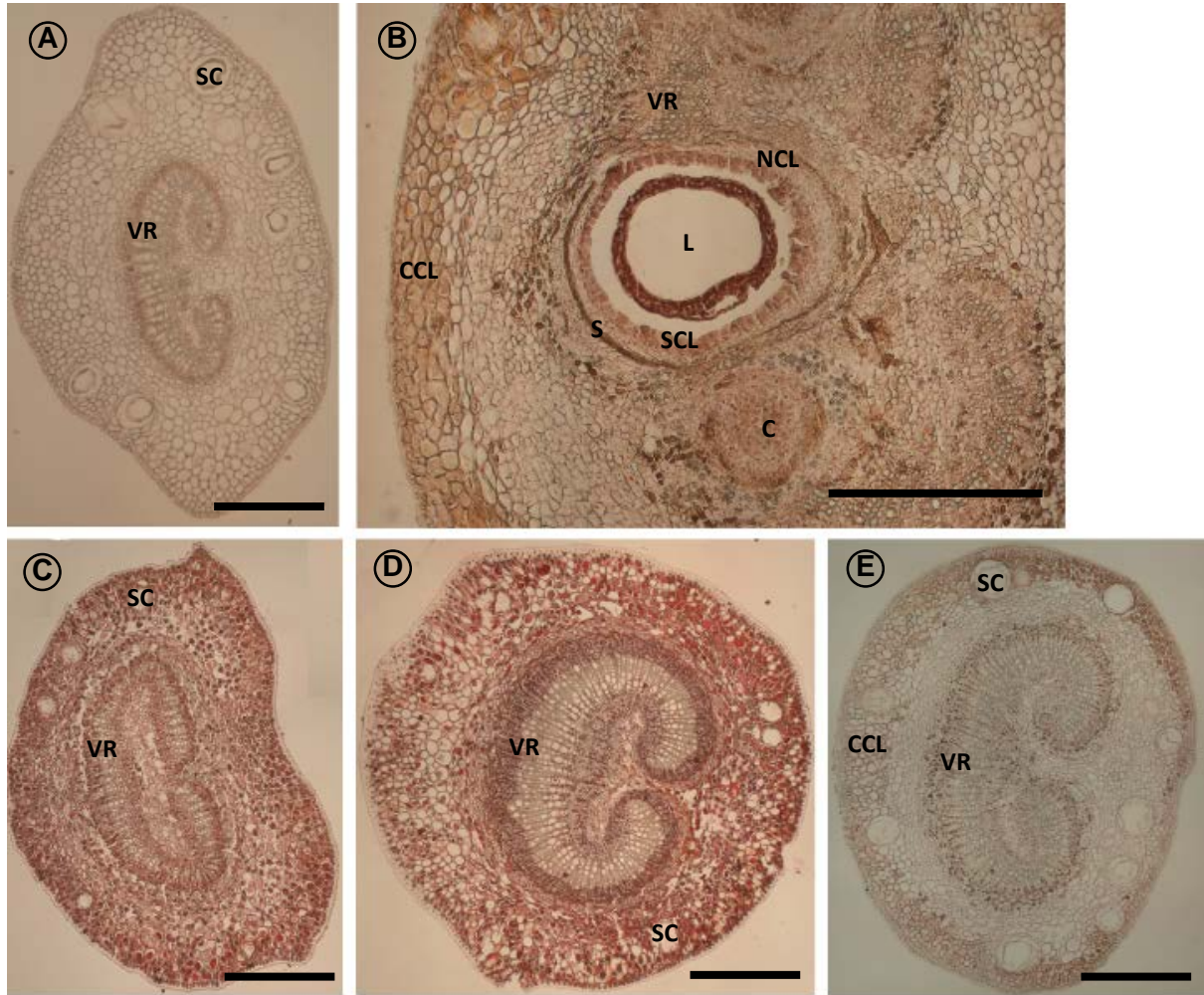
Figure 1. The transverse sections of petioles of *Eucalyptus* trees. (A) Young petiole of *E. camaldulensis* x *E. grandis* hybrid. (B) Young infected petiole of *E. camaldulensis* x *E. grandis* hybrid. (C) Young petiole of *E. erophylla*. (D) Mature petiole of *E. erophylla*. (E) Young petiole of *E. camaldulensis*. Abbreviation: C, chamber; CCL, collenchyma cell layer; L, larva; NCL, nutrient cell layer; S, sclerenchyma cell layer; SC, secretory cavity; SCL, secretory cell layer; VR, vascular ring. Scale bar = 500 μm.

COMPARATIVE MORPHOLOGY AND ANATOMY OF FIVE TYPES OF CECIDOMYIID LEAF GALLS ON *MACHILUS ZUIHOENSIS* HAYATA (LAURACEAE)

SU, Chi-Hao (蘇棨豪) and LIAO, Gwo-Ing (廖國媖)

Department of Life Sciences, National Cheng Kung University, Tainan, Taiwan

Several gall midge species (Diptera: Cecidomyiidae) have been found on *Machilus zuihoensis* Hayata (Lauraceae). This study is aimed to compare the morphology and histogeny during development of five cecidomyiid leaf galls on *M. zuihoensis*, including urn-shaped gall, small urn-shaped gall, obovate gall, hairy oblong gall, and blister gall. Morphological development of galls was observed in the field, and divided into several development stages by morphological characteristics. Gall samples in each development stages was collected, and examined under light microscope to investigate histologic changes between stages, and differences among five gall types. The results show that urn-shaped gall, small urn-shaped gall and hairy oblong gall perform similar development time period, which initiate in February and March, and adult gall midge leave galls in the next year. Obovate gall initiates in February and March, and galls drop form leave to ground in December and next January. Blister gall was found both in March to April and June to September. Urn-shaped gall is different with small urn-shaped gall mainly in the distribution of vascular bundles, cell elongation in the outer top region of gall, and the thickness of cortex. Hair-like structure can only be found on hairy oblong gall, and it initiates before gall tissue break through leave surface. In addition, gall tissue of hairy oblong gall growth parallel with leave after break through leave surface, with secondary metabolites accumulate in cortex far from leave surface. Obovate gall accumulate abundant of starch grains in cortex during horizontal growth of gall, and the gall drop to the ground with larva after gall mature. The gall midges inducing blister gall are considered as a more primitive species then others due to no significant tissue differentiation during all development stage of blister galls, and it's the one which larva leaves gall and pupates outside. Compare with the four phases in gall development that has been published, the main anatomical differences between five types of leaf galls during gall development occur in the growth and differentiation phase which form distinguish morphology of each gall type.

References

1. Chao, J. F., M.S. Thesis, National Cheng Kung University, Tainan, Taiwan, 2010.
2. Yukawa, J. and O. Rohfritsch, in *Biology, Ecology, and Evolution of Gall-Inducing Arthropods*, A. Raman, C. W. Schaefer, T. M. Withers, Science Publishers, Enfield, (2005) 273-304.
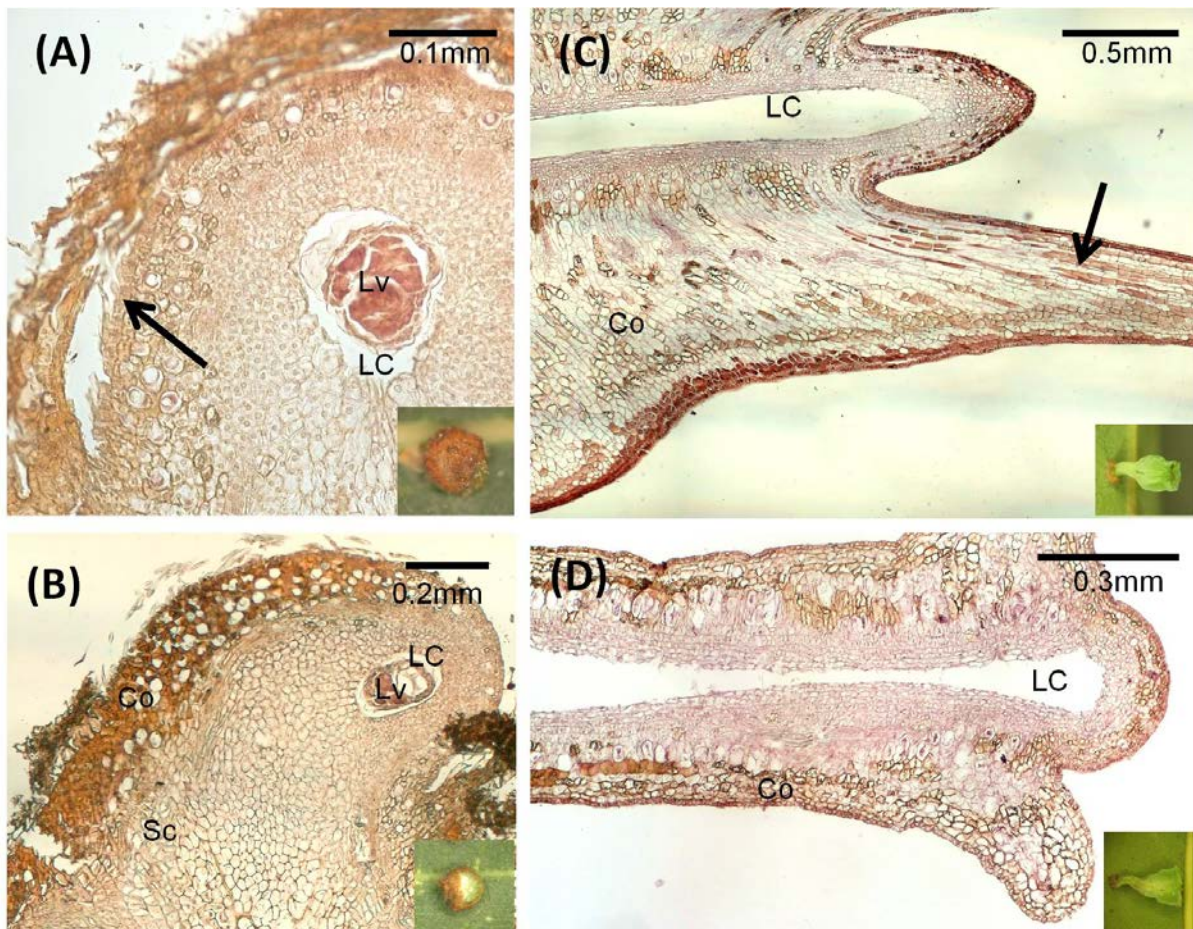
Figure. 1 Sections of developing galls. The insets show the appearance of leaf galls. (A) Hairy oblong gall in stage III. Arrow points the newborn hair-like tissue, which is only found on hairy oblong gall. (B) Hairy oblong gall in stage IV. (C) Urn-shaped gall in stage VI. Arrow points the prolonged cell in the outer top region of gall. (D) Small urn-shaped gall in stage IV. Abbreviations: Co, cortex; LC, larva chamber; Lv, larva; Sc, sclereid layer.

M-P-01	**PLASMONS DISPERSION AND NONVERTICAL INTERBAND TRANSITIONS IN SINGLE-CRYSTAL BI2SE3 INVESTIGATED BY ELECTRON ENERGY-LOSS SPECTROSCOPY** S. C. Liou (劉思謙), M. -W. Chu (朱明文), R. Sankar, F. -T. Huang (黃妃婷), G. J. Shu (戞國俊), F. C. Chou (周方正) and C. H. Chen (陳正弦) Center for Condensed Matter Sciences, National Taiwan University, Taipei, Taiwan
M-P-02	**ATOMIC STRUCTURE OF THE GAN/AL₂O₃ INTERFACE** Yue-Han Wu (吳岳翰) and Li Chang (張立) Department of Materials Science and Engineering, National Chiao-Tung University, Hsinchu, Taiwan.
M-P-03	**MICROSTRUCTURE CHARACTERIZATION OF ZINC SULFIDE SUPERLATTICE NANOWIRES BY TRANSMISSION ELECTRON MICROSCOPY** Yi-Chang Li (李奕錩), Chi-Kang Wu (吳季剛), and Chuan-Pu Liu (劉全璞) Department of Materials Science and Engineering, National Cheng Kung University, Taiwan
M-P-04	**THE INFLUENCE OF ANNEALING TREATMENTS ON MICROSTRUCTURE AND PROPERTIES OF AMORPHOUS FE₈₀SI₈.₅B₁₁ RIBBON** Po-Yu Chen (陳伯宇), Hsin-Yi Lee (李欣怡) and Jer-Ren Yang (楊哲人) Department of Materials Science and Engineering, National Taiwan University
M-P-05	**STRUCTRUAL ANALYSIS OF Si₀.₉Ge₀.₁/Si EPITAXIAL LAYERS BY CONVERGENT BEAM ELECTRON DIFFRACTION** [1]CHEN, Yi-Yan (陳苡諺), [1]WANG, Ting-Yu (王廷玉), [2]CHANG, Hung-Tai (張宏臺), [1]YANG, Jer-Ren (楊哲人), [2]LEE, Sheng-Wei (李勝偉) and [3]Shiojiri, Makoto [1]Department of Materials Science and Engineering, National Taiwan University [2]Department of Materials Science and Engineering, National Central University [3]Kyoto Institute of Technology, Kyoto 606-8585, Japan
M-P-06	**THE STUDY OF INTERPHASE PRECIPITATION MECHANISM AND RELATED MECHANICAL PROPERTIES IN NANOMETER-SIZED CARBIDES STRENGTHENED DUAL-PHASE STEEL** [1]SU, Te-Cheng (蘇德徵), [1]HUANG, Bo-Ming (黃柏銘), [1]YEN, Hong-Wei (顏鴻威)

	[2] HUANG, Ching-Yuan (黃慶淵) and [1] YANG, Jer-Ren (楊哲人) [1]Department of Materials Science and Engineering, National Taiwan University [2]Iron and Steel R&D Department, China Steel Corporation, Kaohsiung, Taiwan
M-P-07	**THE MICRO-MORPHOLOGY AND NANO-MORPHOLOGY OF LENTICULAR MARTENSITE IN THE AISI 440C STAINLESS STEEL** Y. L. Chang (張雅齡) and J. R. Yang (楊哲人) Department of Materials Science and Engineering, National Taiwan University
M-P-08	**THE EFFECT OF MO ON NB CARBIDES IN NB CONTAINING LOW CARBON BAINITIC STRIPS WITH OBSERVATION OF HR TEM IMAGES** Huang, Bo-Ming (黃柏銘), Yen, Hung-Wei (顏鴻威), Yang, Jer-Ren (楊哲人) Department of Materials Science and Engineering, National Taiwan University
M-P-09	**TEM CHARACTERIZATION OF 97.5AU-0.75NI-1.75V INTERLAYER FOR SOFC APPLICATIONS** [1]Kun-Lin Lin (林昆霖) and [2]Jia-Yin Tsai [1] National Nano Device Laboratories, Hsinchu 300, Taiwan [2] Institute of Lighting and Energy Photonics, National Chiao Tung University, Hsinchu, Taiwan
M-P-10	**EFFECT OF ALLOY ADDITION ON THE STRUCTURE OF INTERPHASE PRECIPITATION FOR NANOMETER-SIZED CARBIDE STRENGTHENED DUAL PHASE STEELS** [1]TSAI, Shao-Pu(蔡劭璞), [1]SU, Te-Cheng(蘇德徵), [1]CHENG, Chih-Hung(鄭至閎), [1]HUANG, Bo-Ming(黃柏銘), [2]HUANG, Ching-Yuan(黃慶淵) and [1]YANG, Jer-Ren(楊哲人) [1]Department of Materials Science and Engineering, National Taiwan University [2]R&D Department, China Steel Corporation (CSC)
M-P-11	**THE EMBRITTLEMENT OF ANNEALED AMORPHOUS FE81SI2B17 ALLOY RIBBON** CHEN, Po-Yu (陳伯宇), Lee, Hsin-Yi（李欣怡）and Yang, Jer-Ren（楊哲人） Department of Materials Science and Engineering, National Taiwan University
M-P-12	**ATOMIC-SCALE PROBING OF INTERDIFFUSION AND A LOCALIZED TWO-DIMENSIONAL ELECTRON DENSITY AT AN INSULATING OXIDE INTERFACE**

CHANG, Ching-Pin (張景斌),[12] LIN, Jauyn Grace (林昭吟),[2] CHENG, Su-Ling (鄭淑齡),[12] YANG, Jer-Ren (楊哲人),[1] CHU, Ming-Wen (朱明文),[2] and CHEN, Cheng-Hsuan (陳正弦)[2]

[1] Department of Materials Science and Engineering, National Taiwan University

[2] Center for Condensed Matter Sciences, National Taiwan University

| M-P-13 | **SURFACE EXCITON POLARITON IN MONOCLINIC HFO2: ELECTRON ENERGY-LOSS SPECTROSCOPY STUDY** |

CHU, Ming-Wen (朱明文),[1] LIOU, Sz-Chian (劉思謙),[1] LEE, Yi-Jun (李毅君),[2] HONG, Ming-Hwei (洪銘輝),[2] KWO, Ray-Nien (郭瑞年),[3] and CHEN, Cheng-Hsuan (陳正弦)[1]

[1] Center for Condensed Matter Sciences, National Taiwan University

[2] Department of Materials Science and Engineering, National Tsing Hua University

[3] Department of Physics, National Tsing Hua University

| M-P-14 | **SURFACE EXCITON POLARITONS IN INDIVIDUAL AU NANOPARTICLES IN THE FAR-UV SPECTRAL REGIME** |

CHU, Ming-Wen (朱明文),[1] CHEN, Cheng-Hsuan (陳正弦),[1] F. Javier García de Abajo,[2] DENG, Jin-Pei (鄧金培),[3] and MOU, Chung-Yuan (牟中原)[4]

[1] Center for Condensed Matter Sciences, National Taiwan University

[2] Instituto de Óptica CSIC and Unidad Asociada CSIC-Universidade de Vigo, Serrano 121, 28006 Madrid, Spain

[3] Department of Chemistry, Tamkang University

[4] Department of Chemistry, National Taiwan University

| M-P-15 | **STEM-EELS/EDS STUDIES OF ULTRA-THIN 4.5nm NICKEL SILICIDE FILMS** |

Wu, Chien-Ting (吳建霆),[1] Lee, Yao-Jen (李耀仁),[1,2] Hsueh, F.-K. (薛富國),[1] Sung, P.-J. (宋柏融),[1] ChloT.-C.(卓大鈞),[3] Current, M. I.,[4] and Chao, Tien-Sheng(趙天生)[3]

[1]National Nano Device Laboratories, Hsinchu City, Taiwan.

[2]Department of Physics, National Chung Hsing University, Taichung, Taiwan.

[3]Department of Electrophysics, National Chiao Tung University, Hsinchu, Taiwan.

[4]Current Scientific, San Jose, CA 95124 USA.

| M-P-16 | **ACCELERATION OF NANO-STRUCTURED BAINITE BY TWO STEP HEAT TREATMENT** |

TSAI, Yu-Ting (蔡宇庭),[1] HUANG, Ching-Yuan（黃慶淵）[2] and YANG, Jer-Ren（楊哲人）[1]

[1]Department of Materials Science and Engineering, National Taiwan University, Taipei, Taiwan

[2]Iron and Steel R&D Department, China Steel Corporation

M-P-17	**RETAINED AUSTENITE STABILIZATION AND ITS EFFECT ON TOUGHNESS OF A LOW CARBON LOW ALLOYED STEEL BY TWO-STEP INTERCRITICAL TREATMENT** XIE, Zhen-Jia (謝振家), YUAN, Sheng-Fu (袁勝福), and SHANG, Cheng-Jia (尚成嘉) School of Materials Science and Engineering, University of Science and Technology Beijing, Beijing, China
M-P-18	**MULTI-PHASE MICROSTRUCTURE AND NANO-SIZED PRECIPITATES IN A NB-BEARING AND COPPER-MICROALLOYED STEEL BY A TWO-STEP REVERSED HEAT TREATMENT** ZHOU, Wen-Hao (周文浩), XIE, Zhen-Jia (谢振家), GUO, Hui (郭晖), WANG, Xue-Min (王学敏) and SHANG, Cheng-Jia (尚成嘉) [1]Department of Materials Science and Engineering, University of Science and Technology Beijing, Beijing, China
M-P-19	**ANNEALING BEHAVIOR OF COBALT-PHOSPHORUS ELECTRODEPOSITS** [1,2]CHEN, Fu-Je (陳黼澤), [1]LIN, Chao-Sung (林招松), [2]PAN, Yung-Ning (潘永寧) and [3]Lee, Chun-Ying (李春穎) [1] Department of Materials Science and Engineering [2] Department of Materials Science and Engineering, National Taiwan University, Taipei, Taiwan [3] Department of Mechanical Engineering, National Taipei University of Technology, Taipei, Taiwan
M-P-20	**MICROSTRUCTURAL CHARACTERIZATION OF THE LOW MELTING POINT GLASS-CERAMIC COMPOSITE COATING** CHEN, Fu-Je (陳黼澤) and LIN, Chao-Sung (林招松) Department of Materials Science and Engineering, National Taiwan University, Taipei, Taiwan.
M-P-21	**INFLUENCE OF SURFACE OXIDATION ON THE VALENCE ELECTRON ENERGY-LOSS SPECTRUM OF WURTZITE ALUMINUM NITRIDE**

	Michael R. S. Huang (黃榮喜),[1] Rolf Erni,[2] and Chuan-Pu Liu (劉全璞) [1,] [1] Department of Materials Science and Engineering, National Cheng-Kung University, Tainan 701, Taiwan [2] Electron Microscopy Center, Empa, Swiss Federal Laboratories for Materials Science & Technology, 8600 Dübendorf, Switzerland
M-P-22	**TRANSMISSION ELECTRON MICROSCOPY ANALYSES FOR THIN FILMS GROWN BY ATOMIC LAYER DEPOSITION** CHAO, Shih-Chun (趙士鈞), YU, Chia-Hao (余家濠), WEN, Cheng-Yen (溫政彥) Department of Materials Science and Engineering, National Taiwan University, Taipei, Taiwan
M-P-23	**KINETICS OF SILICIDE FORMATION IN SI NANOWIRES** CHOU, Yi-Chia(周苡嘉),[1] TU, King-Ning(杜經寧)[2] [1]Department of Electrophysics, National Chiao-Tung University, Hsinchu, Taiwan [2]Department of Materials Science and Engineering, University of California Los Angeles, Los Angeles, USA
M-P-24	**DIRECT OPTICAL CHARACTERIZATIONS FOR GROWTH BEHAVIOR OF GRAPHENE ON COPPER BY CHEMICAL VAPOR DEPOSITION** CHANG, Ren-Jie (張仁頡), TSAI, Yun-Yi(蔡昀嶧) and WEN, Cheng-Yen(溫政彥) Department of Materials Science and Engineering, National Taiwan University, Taipei, Taiwan
M-P-25	**IN-SITU TEM STUDY OF THE LITHIATION BEHAVIOR OF A SINGLE SN DOPED ZNO NANOWIRE** Lai, Ming-Wei (賴明偉), Lo, Shen-Chuan (羅聖全), Chen, Yu-Hsiang (陳育祥),and Tsai, Cheng-Ting (蔡承廷) Material and Chemical Research Laboratories, Industrial Technology Research Institute, Hsinchu, Taiwan
M-P-26	**CHARGE DENSITY WAVE STUDY IN DY$_5$IR$_4$SI$_{10}$** M. H. Lee[1,2] (李明浩), C. H. Chen[1,2,3,] (陳正弦), M.-W. Chu[2] (朱明文), H. D. Yang[4] (楊弘敦) 1. Department of Physics, National Taiwan University, Taipei, Taiwan 2. Center for Condensed Matter Sciences, National Taiwan University 3. Institute of Atomic and Molecular Sciences, Academia Sinica, Taipei, Taiwan 4. Department of Physics, National Sun Yat-sen University, Kaohsiung, Taiwan

M-P-27	**ELECTRONICALLY PHASE-SEPARATED CHARGE DENSITY WAVES IN LU$_2$IR$_3$SI$_5$**
	M. H. Lee[1,2] (李明浩), C. H. Chen[1,2,3,] (陳正弦), M.-W. Chu[2] (朱明文), C. S. Lue[4] (呂欽山), Y. K. Kuo[5] (郭永綱)
	1. Department of Physics, National Taiwan University, Taipei, Taiwan
	2. Center for Condensed Matter Sciences, National Taiwan University
	3. Institute of Atomic and Molecular Sciences, Academia Sinica, Taipei, Taiwan
	4. Department of Physics, National Cheng Kung University, Tainan, Taiwan
	5. Department of Physics, National Dong Hua University, Hualien, Taiwan

PLASMONS DISPERSION AND NONVERTICAL INTERBAND TRANSITIONS IN SINGLE-CRYSTAL BI₂SE₃ INVESTIGATED BY ELECTRON ENERGY-LOSS SPECTROSCOPY

[1]S. C. Liou (劉思謙), [1]M. -W. Chu (朱明文), [1]R. Sankar, [1]F. -T. Huang (黃妃婷)
[1]G. J. Shu (殳國俊), [1]F. C. Chou (周方正) and [1]C. H. Chen (陳正弦)

[1] Center for Condensed Matter Sciences, National Taiwan University, Taipei, Taiwan

Plasmons dispersion and nonvertical interband transitions in Bi_2Se_3 single crystals were investigated by electron energy-loss spectroscopy in conjunction with (scanning) transmission electron microscopy, (S)TEM-EELS. Both volume plasmons (π plasmon at 7 eV and $\pi+\sigma$ plasmon at 17 eV) and surface plasmons (~5.5 and 10 eV) were demonstrated in STEM-EELS spectra and the corresponding spectral imaging in real space [1]. In the further EELS experiments in reciprocal space, the momentum-dependent spectra reveal very different dispersion behavior between π and $\pi+\sigma$ plasmons, with $\pi+\sigma$ plasmons showing a typical quadratic dependence whereas the π plasmon exhibiting a linear dispersion analogous to what was reported for graphene. Furthermore, a low energy excitation 0.7~1.6 eV was also observed which is attributed to direct nonvertical interband transitions along the ΓF direction [2].

References

1. S. C. Liou et al., *Phys. Rev. B* 87, 085126 (2013).
2. S. K. Mishra et al., *J. Phys.:Condens. Matter* 9 (1997) 461.
3. This research was supported by National Science Council of Taiwan (NSC99-2112-M-002-027-MY3 and NSC101-2811-M-002-130).

FIG. 1. (a) STEM–EELS spectra acquired on single-crystal Bi$_2$Se$_3$ with the electron probe positioned at the material interior and sample edge (inset HAADF image). (b) The energy of π and $\pi+\sigma$ plasmons as a function as momentum transfer (q), respectively. (c) The dispersion curve of the nonvertical intenband transition peaks as a function of momentum-transfer with sample tilting (marked with black square, respectively). The dashed line is the linear curve fitting. The dispersion of the lowest conduction band along ΓF direction in ref. 2 with energy normalized to the experimental value of energy gap (E$_g$= 0.32 eV) at q= 0 is also plotted for comparison.

ATOMIC STRUCTURE OF THE GAN/AL₂O₃ INTERFACE

[1]Yue-Han Wu（吳岳翰）* and [1]Li Chang（張立）

[1]Department of Materials Science and Engineering, National Chiao-Tung University, Hsinchu, Taiwan.

Gallium nitride (GaN) has been widely used in many practical applications such as light-emitting diodes and high-electron-mobility transistors since Nakamura *et al.* demonstrated successful growth of GaN on sapphire (Al_2O_3) by metal-organic chemical vapor deposition (MOCVD).[1] Though the interfacial structure of GaN/Al_2O_3 has been intensively studied in the past by high-resolution TEM, there is still no clear direct evidence on the atomic structure about bonding characteristics across the interface. In this study, we used scanning transmission electron microscopy (STEM) to investigate the atomic structure of the interface between a low-temperature grown GaN layer and *c*-plane Al_2O_3 substrate.

STEM observations were carried out in JEOL ARM 200F microscopes (resolution ≤ 0.8Å) equipped with a Gatan GIF Quantum®ER system and an Oxford Max80 SDD EDX detector. TEM specimens along $[10\overline{1}0]Al_2O_3$ were prepared carefully to avoid the excess formation of ion damage layers by mechanical grinding and ion milling.

Figure 1(a) shows an HRTEM image of the GaN/Al_2O_3 interface. No interlayers between GaN and Al_2O_3 were found, and there are twins and stacking faults in the GaN region. Figures 1 (b) and (c) show the high-angle annular dark field (HAADF) and annular bright field (ABF) images acquired from the same region. The brightest contrast in the HAADF image is associated with Ga atoms, whereas the relatively weak one with Al. In the ABF image, the contrast shows that Ga and N can be clearly seen as dark spots in the GaN layer, and Al and O in Al_2O_3.[2,3] As a result, it can be determined that N atoms are bonded with Al at the interface. Further supporting evidence was obtained from EELS and EDX measurements.

References

1. S. Nakamura, Y. Harada, and M. Seno, Appl. Phys. Lett. **58**, 2021 (1991).
2. W. W. Mathews, Trans. Am. Microsc. Soc. **2**, 190 (1953).
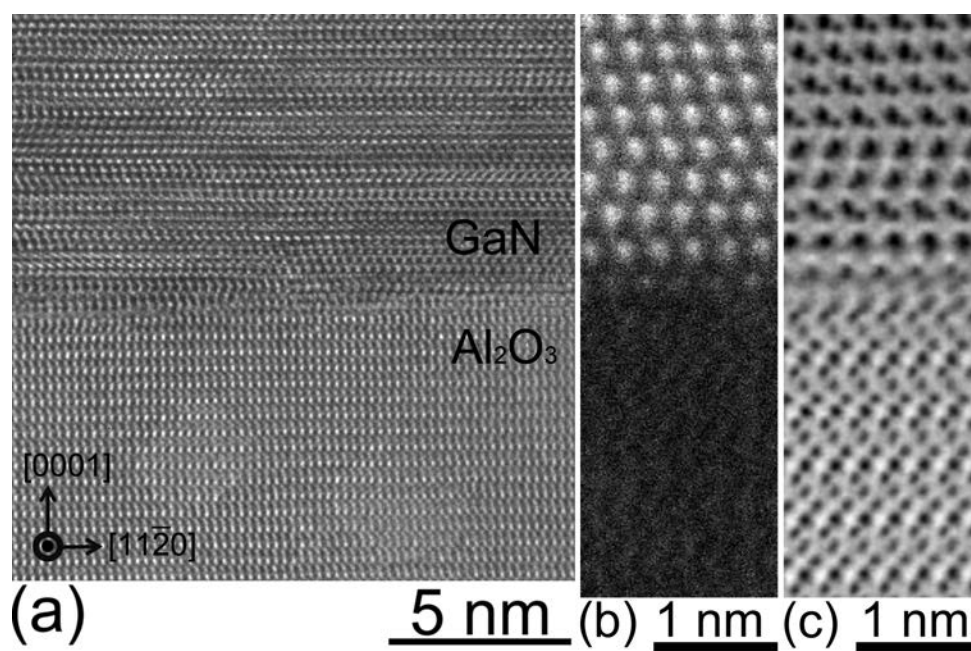3. R.Ishikawa, E. Okunishi, H. Sawada, Y. Kondo, F. Hosokawa, and E. Abe, Nature Mater. 10, 278 (2011).

Fig. 1 (a) A HRTEM image of the GaN/Al$_2$O$_3$ interface along $[10\bar{1}0]_{Al_2O_3}$. The atomic structure in same interfacial region showed in HAADF (b) and ABF (c) images.

MICROSTRUCTURE CHARACTERIZATION OF ZINC SULFIDE SUPERLATTICE NANOWIRES BY TRANSMISSION ELECTRON MICROSCOPY

[1]Yi-Chang Li (李奕錩), [1]Chi-Kang Wu (吳季剛), and [1]Chuan-Pu Liu (劉全璞)

[1]Department of Materials Science and Engineering, National Cheng Kung University, Taiwan

We have synthesized zinc sulfide (ZnS) nanowires by thermal chemical vapor deposition with three kind of microstructure which were round-like,belt-like and arrow-like.First, the length and size of the as-deposited ZnS nanowires are invesgated by SEM. Then, they have been analyzed by transmission electron microscopy in detail. By high resolution electron microscopy (HREM) imaging and selected area electron diffraction results, we characterize their crystal structure, growth direction and defects.
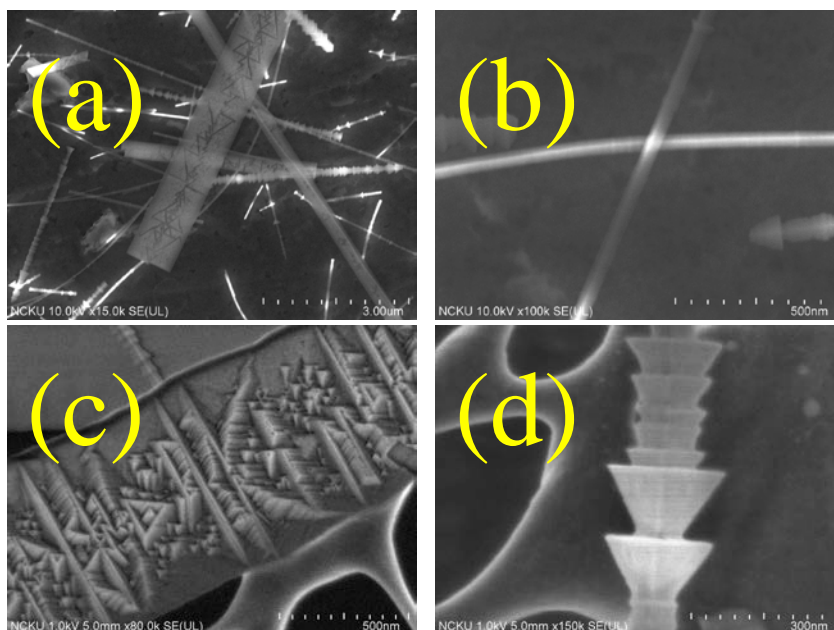
Fig. 1. (a) Low magnification SEM image of ZnS nanowire (b) SEM image of round ZnS nanowire, (c) belt-like ZnS nanowire and, (d) arrow-like ZnS nanowire.
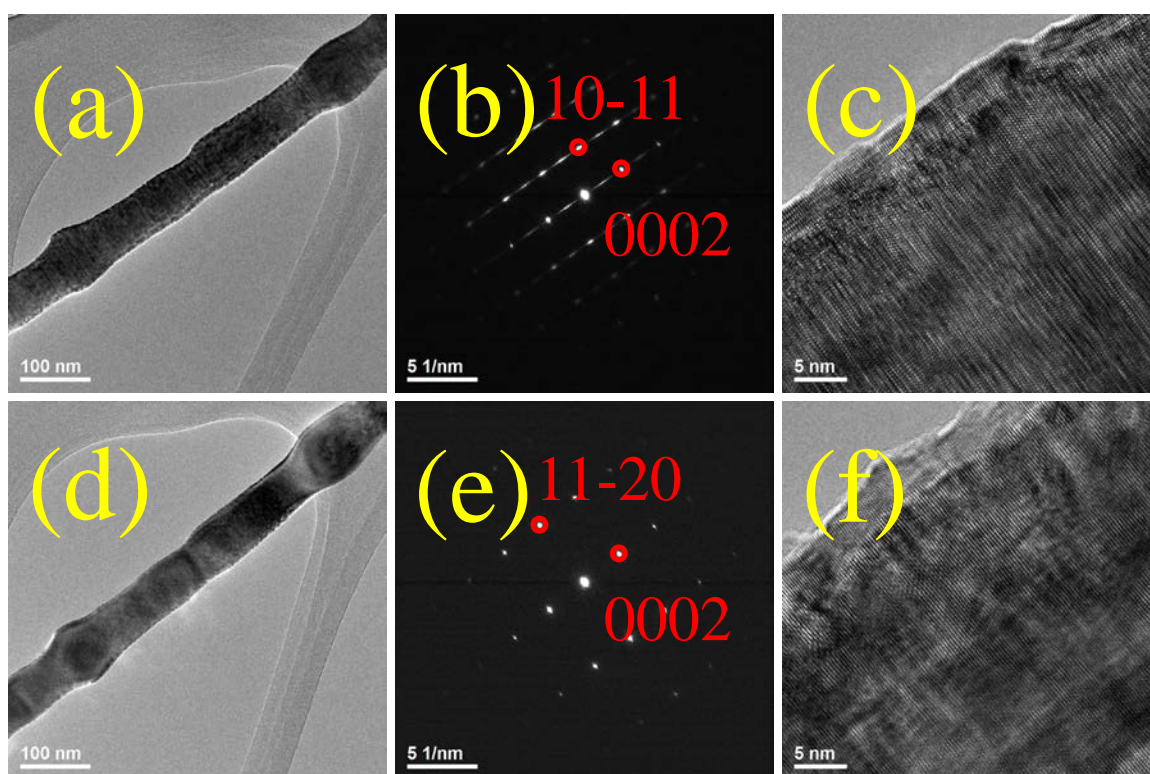
Fig. 2. (a) TEM image of an individual arrow-like ZnS nanowire, (b) the corresponding SAED and, (c) the HRTEM image; (d) TEM image of individual arrow-like ZnS nanowire afer tilting, (e) the corresponding SAED and, (f) the HRTEM image.

THE INFLUENCE OF ANNEALING TREATMENTS ON MICROSTRUCTURE AND PROPERTIES OF AMORPHOUS FE$_{80}$SI$_{8.5}$B$_{11}$ RIBBON

[1]CHEN, Po-Yu(陳伯宇), [1]Lee, Hsin-Yi（李欣怡） and [1]Yang, Jer-Ren（楊哲人）

[1]Department of Materials Science and Engineering, National Taiwan University, Taipei, Taiwan

In this work, specimens of amorphous Fe-Si-B ribbons were annealed at various temperatures ranging from 300°C to 500°C. The detailed microstructures of the annealed ribbons were investigated by electron microscopy (including SEM and TEM). The properties of these ribbons annealed at the corresponding temperatures were analyzed, such as brittleness, hysteresis curve and crystallization behavior. The XRD results showed that the crystallization temperature T_x is located at about 400ºC. The first nucleation in amorphous matrix is the dendrite crystal which is α-Fe (Si). At higher annealing temperature, the boride phase such as Fe$_3$B then precipitates in the matrix. The bend test results indicated that a ductile-brittle transition occurred at about 300~350ºC, It is proposed that the annealing induced embrittlement in ribbons can be divided into low- and high-temperature embrittlement. The former is attributed to the formation of short-range orderings, and the latter is related to crystallization. According to the HRTEM observation, some short range ordering may exist in the amorphous matrix before T_x, which causes the changes in brittleness and magnetic properties.
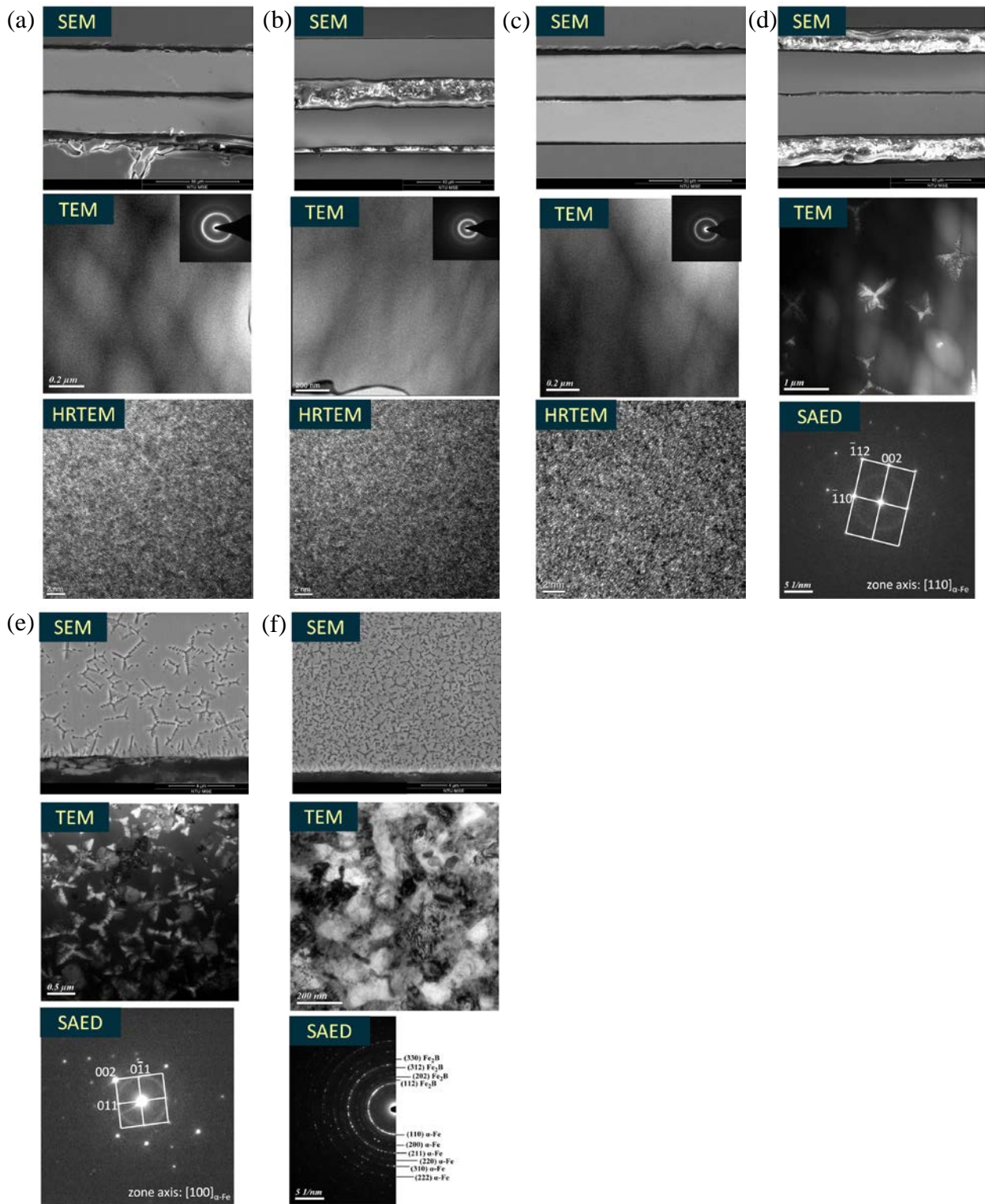
Figure 1 TEM observations of the $Fe_{80}Si_{8.5}B_{11}C_{0.5}$ alloy annealing at different temperature for 1 hr: (a) As-received, (b)300°C, (c)350°C, (d)400°C, (e)450°C, (f)500°C.

STRUCTRUAL ANALYSIS OF $Si_{0.9}Ge_{0.1}$/Si EPITAXIAL LAYERS BY CONVERGENT BEAM ELECTRON DIFFRACTION

[1]CHEN, Yi-Yan (陳苡諺), [1]WANG, Ting-Yu (王廷玉), [2]CHANG, Hung-Tai (張宏臺), [1]YANG, Jer-Ren (楊哲人), [2]LEE, Sheng-Wei (李勝偉) and [3]Shiojiri, Makoto

[1]Department of Materials Science and Engineering, National Taiwan University, Taipei, Taiwan

[2]Department of Materials Science and Engineering, National Central University, Jong-li, Taiwan

[3]Kyoto Institute of Technology, Kyoto 606-8585, Japan

Convergent-beam Electron diffraction (CBED) has recently attracted much attentions on the strain analysis of electronic devices due to its high-sensitivity and accuracy on the determination of lattice parameters.[1][2] In this study, $Si_{0.9}Ge_{0.1}$ epitaxial layer (10 at% Ge) has successfully deposited on the Si (001)-orientated substrate by ultra-high vacuum/chemical vapor deposition (UHV/CVD) system. FEI Tecnai F30 operated at 300 kV attached with energy filtered and STEM mode was used in this work. A series of energy filtered CBED patterns across the $Si_{0.9}Ge_{0.1}$/Si interface was acquired. From the HR-TEM image and EDS line profile, the high quality and uniform $Si_{0.9}Ge_{0.1}$ epitaxial layer with 4 μm was successfully deposited on the (001)-orientated p-Si substrate by UHV/CVD system. [430] zone axis and 1° tilting toward [001] direction from [430] zone axis (off [430] zone axis) were chosen as experimental zone axes. The simulated and experimental CBED patterns were shown in Fig. 1. When taking at close the $Si_{0.9}Ge_{0.1}$/Si interface, for 400 nm thick TEM specimen, split HOLZ lines started at 250 nm from the $Si_{0.9}Ge_{0.1}$/Si interface of Si side and Ge side, and clearer CBED patterns could be observed by off [430] zone axis, which reveals that the blurred pattern caused by the multi-fringes of (004) Kikuchi line pairs was efficiently avoided by off [430] zone axis. From the simulated CBED patterns with split HOLZ lines by initial beam tilting and lattice constant changes, the widely splitting of (008) Kikuchi line pairs could be produced by initial beam tilting, not found by lattice constant changes, which indicates that bending of lattice planes along the direction of TEM specimen thickness is the most possible reason in this study.

References

1. A. Benedetti, H. Bender, C. Torregian, M. Van Dal and K. Maex, *Mater. Sci. Eng.*, B 61 (2004) 114.
2. P. Zhang, A. A. Istratov, E. R. Weber, C. Kisielowski, H. He, *Appl. Phys. Lett.* 89 (2006) 161907.
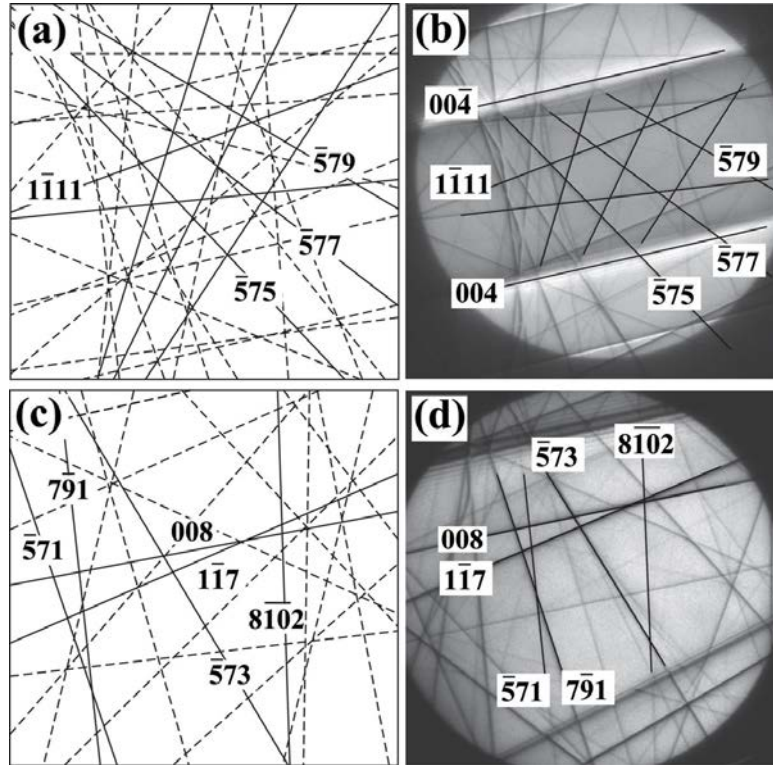
Fig. 1. (a, b) Simulated and experimental CBED patterns at the exact [430] zone axis, respectively. (c, d) Simulated and experimental CBED patterns at the off [430] zone axis, respectively.

THE STUDY OF INTERPHASE PRECIPITATION MECHANISM AND RELATED MECHANICAL PROPERTIES IN NANOMETER-SIZED CARBIDES STRENGTHENED DUAL-PHASE STEEL

[1]SU, Te-Cheng(蘇德徵), [1]HUANG, Bo-Ming(黃柏銘）, [1]YEN, Hong-Wei(顏鴻威），
[2] HUANG, Ching-Yuan(黃慶淵） and [1]YANG, Jer-Ren(楊哲人）

[1]Department of Materials Science and Engineering, National Taiwan University, Taipei, Taiwan
[2]Iron and Steel R&D Department, China Steel Corporation, Kaohsiung, Taiwan

The dual-phase steel is considered to be a potential new generation steel for automobiles owing to the high formability and low production cost. However, dual-phase steel suffers from the mismatch of strain in the interphase boundary, resulting in the poor hole-expansion ratio [1]. Therefore, this research attempts to develop new automobile dual phase steel strips with ultrahigh strengths and excellent formability by creating a microstructure of martensite and strong ferrite by means of nanometer-sized precipitation hardening. The dilatometer experiment was conducted with different austenization temperature and isothermal holding temperature. The results show that raising the austenization temperature can increase ferrite Vicker hardness (Figure 1) with parallel and coherent interphase precipitation structure (Figure 2). This outcome can be attributed to the rise of prior austenite grain size reducing the ferrite transformation rate, further increasing the precipitation density.

Abstract is due on June 12, 2013.

References

1. M. S. Rashid, *Ann. Rev. Mater. Sci.* 11 (1981) 245
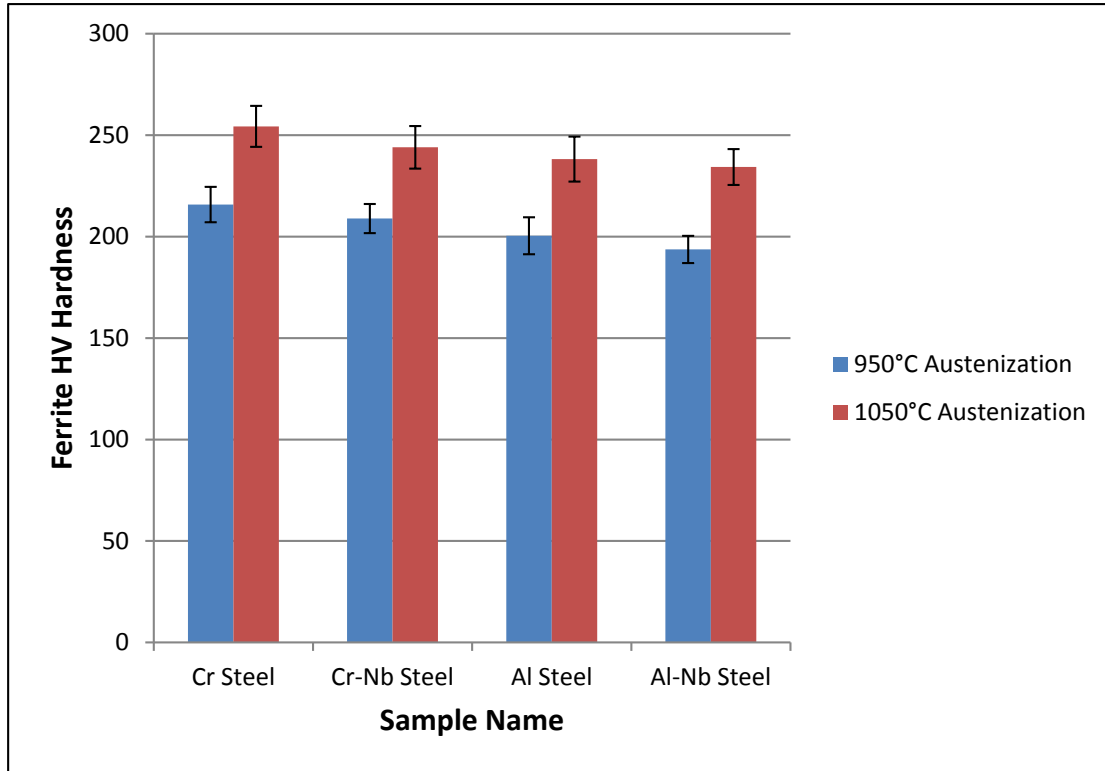
Figure 1. Comparison of average ferrite HV hardness of heat-treated specimen austenized at 950°C or 1050°C and isothermal held at 650°C for 8 seconds
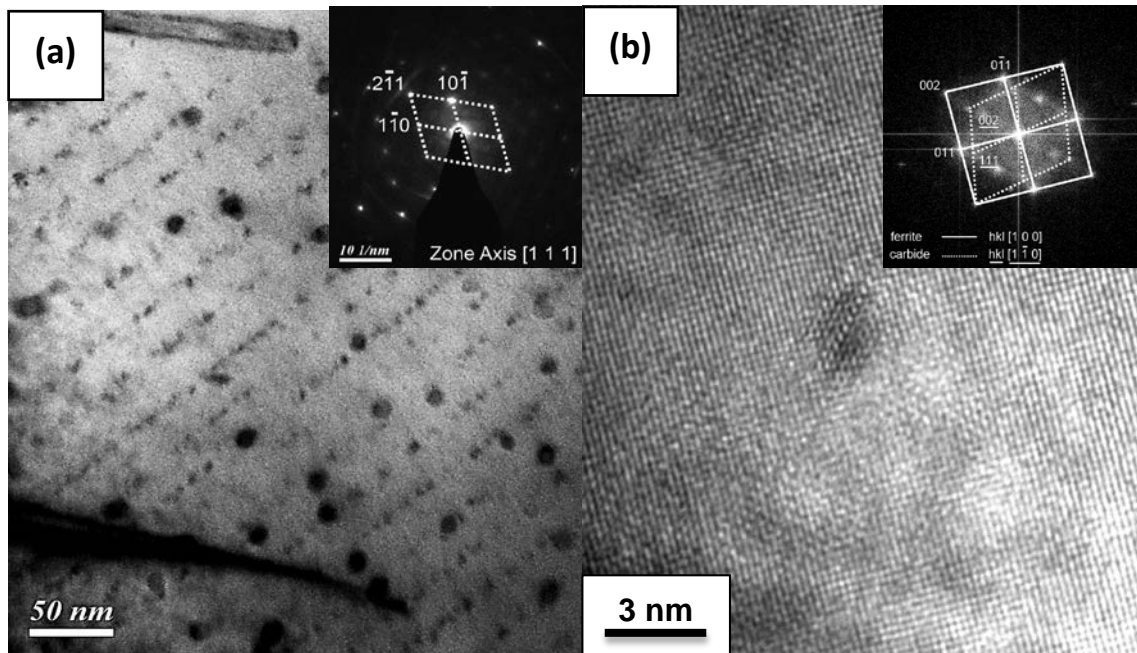
Figure 2. (a) Interphase precipitation structure of heat treated Al steel austenized at 1050°C and isothermal held at 700°C. The sheet plane of this precipitation can be indexed near {211}. (b) High resolution TEM image and its fast Fourier transform image showing the Baker-Nutting orientation relationship between ferrite and interphase precipitation.

THE MICRO-MORPHOLOGY AND NANO-MORPHOLOGY OF LENTICULAR MARTENSITE IN THE AISI 440C STAINLESS STEEL

Chang Y. L. (張雅齡)[1], Lee Hsin-Yi (李欣怡)[1], Yang J. R. (楊哲人)[1]

[1]Department of Materials Science and Engineering, National Taiwan University, Taipei, Taiwan

The microstructure of an high-chromium, high-carbon AISI 440C stainless steel after subzero treatment has been studied in this research. The austenite matrix was first transformed to plate martensite and turned into lenticular martensite. From the TEM observation results, it is indicated that the growth of lenticular martensite is achieved by the extension of twins, which released latent heat and activated the screw dislocations to slip in untwinned regions. The midrib keeps the lattice-invariant deformation mode of twinning, whereas the extended twinned region and untwinned region combine both twinning and slip modes. Furthermore, the mechanism and the microstructure of tempered martensite decomposition and carbide precipitation have been studied in the steel. The morphology and the chemical composition of carbide precipitates at different positions (e.g. midrib, extended twinned regions, and untwinned regions) in lenticular martensite and the crystallography of their formation have been examined by means of TEM after tempering at 600oC for various times.
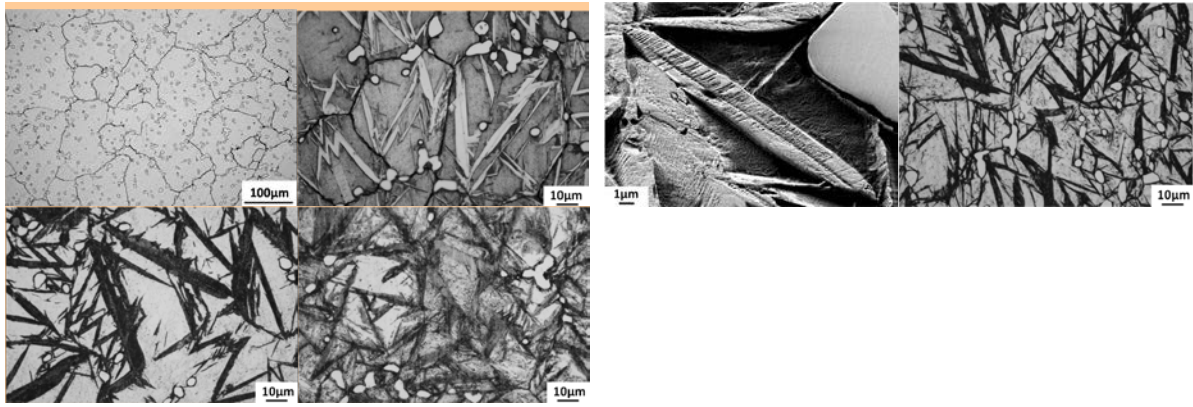
Fig. 2 The OM and SEM showing the microstructures (a) homogenized；(b) and (c) subzero cooled at -196℃ for 15min；tempered at 600ºC for (d) 0.5 hr；(e) 1hr；(f) 2hr.
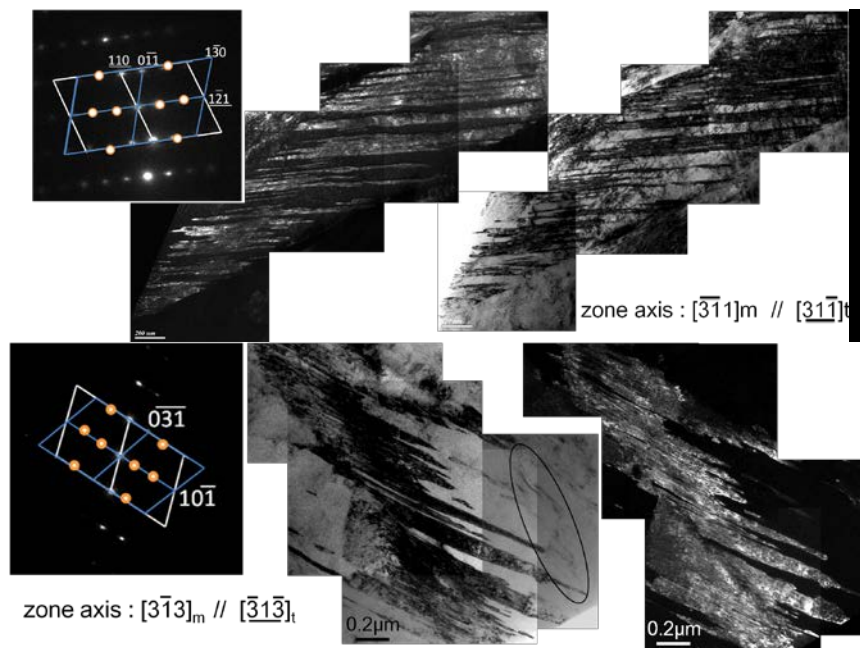
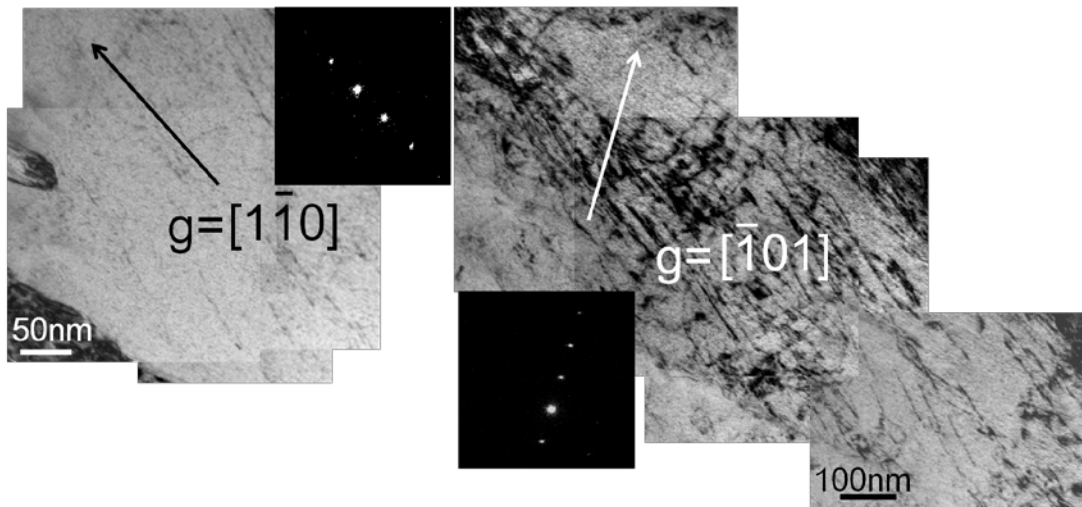Fig. 3 The TEM showing the microstructures (a) thin plate and (b) lenticular martensite.

Fig. 4 Shows the some area of untwined region observed by different two beam condition (a) g = 1$\bar{1}$0 and (b) g=$\bar{1}$01

THE EFFECT OF MO ON NB CARBIDES IN NB CONTAINING LOW CARBON BAINITIC STRIPS WITH OBSERVATION OF HR TEM IMAGES

[1]Huang, Bo-Ming(黃柏銘), [1]Yen, Hung-Wei(顏鴻威), [1]Yang, Jer-Ren(楊哲人)

[1]Department of Materials Science and Engineering, National Taiwan University, Taipei, Taiwan

The main purpose of this work was to elucidate the effect of Mo addition on the development of microstructure and precipitation of Nb carbides in the hot rolled low-carbon Nb-containing bainitic steels. Three experimental steels have been investigated; they have the same base composition 0.05C-1.7Mn-0.08Nb (wt%); one is without Mo addition, the other with 0.1 wt% Mo, and final with 0.3wt% Mo as shown in Table 1. The strips were manufactured by hot rolling process and air-cooled down room temperature.

In previous investigation of nanometer-sized carbides of Nb-Mo low carbon bainitic strips during tempering process, the MC type carbides such as Nb carbides precipitated at bainite requires similar morphology as Nb carbides precipitated at prior austenite during hot milling stage. The aim of study is to distinguish two types of carbides and further to determine the effect of Mo on morphology of nanometer-sized Nb carbides at bainite in according to different orientation relationship (O.R.) with corresponding matrix. In High Resolution TEM (HR TEM) images, it is found that the carbides have Baker-Nutting O.R. with bainitic matrix different from cubic-cubic O.R as shown in Figure 1. strain induced Nb carbides requires. With corresponding EDX spectrum, it is known that more addition of Mo can incorporate into Nb carbides to form (Nb,Mo) carbides and maintain the crystallography. After statistic of carbides size, the (Nb,Mo) carbides behave slight coarsening phenomena with raising concentration of Mo in bainitic matrix. It is suggested that the addition of Mo needs to be limited between 0.1 and 0.3wt% in development of precipitation strengthening in Nb-containing bainitic strips.

Table 1 The composition of as received hot rolled strips

Strip No.	C	Si	Mn	N	Al	Cr	Ti	Nb	Mo
Nb	0.05	0.2	1.7	0.004	0.03	0.18	0.016	0.08	-
Nb-Mo	0.05	0.2	1.7	0.004	0.03	0.18	0.016	0.08	0.1
Nb-3Mo	0.05	0.2	1.7	0.004	0.03	0.18	0.016	0.08	0.3
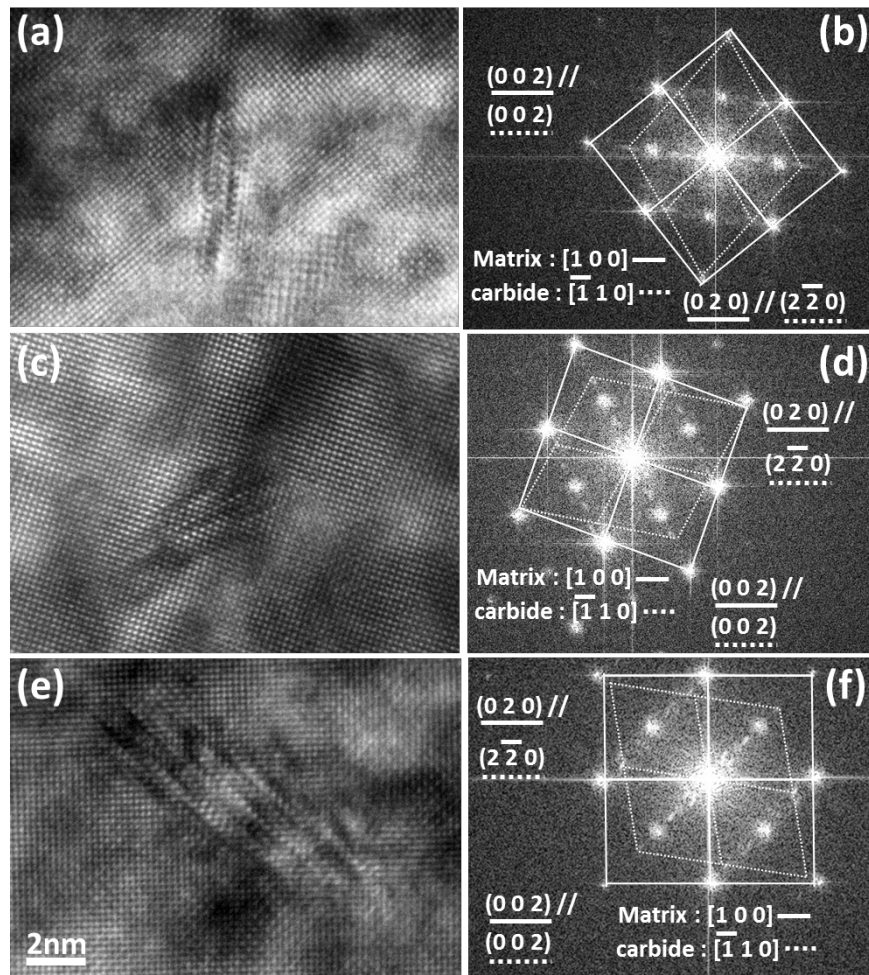
Figure 1 High Resolution TEM images and corresponding FFT images showing morphology and Bake-Nutting orientation relationship in (a),(b) Nb-strip, (c),(d) Nb-Mo strip, and (e),(f) Nb-3Mo strip.

TEM CHARACTERIZATION OF 97.5AU-0.75NI-1.75V INTERLAYER FOR SOFC APPLICATIONS

Kun-Lin Lin [1,*] and Jia-Yin Tsai [2]

[1] National Nano Device Laboratories, Hsinchu 300, Taiwan

[2] Institute of Lighting and Energy Photonics, National Chiao Tung University, Hsinchu 300, Taiwan

The microstructure of gold-based interlayer with composition (in wt%) of 97.5Au-0.75Ni-1.75V following oxidation at 850ºC/200 min was characterized by TEM/EDS and SEM. A loose vanadium oxide (V_2O_5) and nickel vanadate ($Ni_2V_2O_7$) formed and distributed within the oxidized 97.5Au-0.75Ni-1.75V interlayer. No evidence of NiO was found because there was not enough Ni present to form nickel oxide. The oxide products in the 97.5Au-0.75Ni-1.75V interlayer after oxidation are consistent with the Pilling-Bedworth (PB) ratio considerations. Metallic sealants have been shown to provide rigid sealing and higher stress accommodation in Solid Oxide Fuel Cells (SOFCs) applications. Before joining, the oxidation behavior of a gold-based interlayer used at high temperatures in air must be thoroughly characterized in present study.

Figure 1(a–c) show a BFI, EDS, and SADP of the 97.5Au-0.75Ni-1.75V interlayer before oxidation, displaying a rod-like Au-rich phase with large stress fields and high dislocation density was observed. Figure 2 shows the backscattered electron images of the 97.5Au-0.75Ni-1.75V interlayer after oxidation. No obvious oxide scale exists at the surface of the 97.5Au-0.75Ni-1.75V interlayer after oxidation, but several irregularly shaped particles are distributed over the interlayer. Figure 3 (a) shows a BFI of the Au-rich phase and loose vanadium oxide (V_2O_5) accompanied with cracks in the 97.5Au-0.75Ni-1.75V interlayer following oxidation. The composition of V_2O_5 is 41.5 at. % V, 57.0 at.% O, and 1.5 at.% Au. Figures 3(c) to (e) display the SADPs of V_2O_5 along with the zone axes of [$\bar{1}1\bar{1}$], [100], and [130], respectively. The lattice parameters of orthorhombic V_2O_5 were calculated to be $a = 11.80$ Å, $b = 4.12$ Å, $c = 3.58$ Å and $\lambda = \beta = \gamma = 90º$, corresponding with the values of V_2O_5 of ICSD # 15798. Figure 4 (a) shows a BFI of Au-rich phase and a nickel vanadate ($Ni_2V_2O_7$) phase formed at the surface of the interlayer. Figure 4(b) shows the EDS spectrum of $Ni_2V_2O_7$, containing 23.0 at.% Ni, 19.2 at. % V, and 57.8 at.% O. The SADPs of $Ni_2V_2O_7$, along with the zone axes of [$10\bar{1}$], [111], and [211], respectively, are shown in Figs. 6(c) to (e). The lattice parameters of monoclinic $Ni_2V_2O_7$ were calculated to be $a = 6.65$ Å, $b = 8.27$ Å, $c = 9.25$ Å and $\beta = 99.66º$, corresponding with monoclinic $Ni_2V_2O_7$ in ICSD # 2358.

From the Pilling-Bedworth (PB) ratio considerations, the PB ratios are 1.52 and 3.18 for oxidation of Ni and V, respectively. These values mean that Ni should form the most protective scale and V should form an unstable scale that would easily flake off. The PB ratio considerations are consistent with our observations of oxide products.

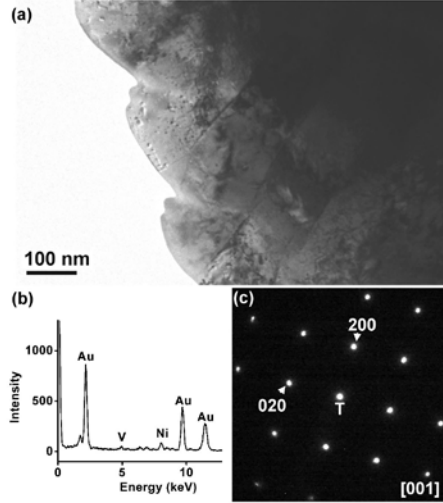(a)

100 nm

(b)

(c)

200

020

[001]

Fig. 1 (a) Transmission electron micrograph (bright-field image, BFI) of the 97.5Au-0.75Ni-1.75V interlayer before oxidation, indicating the rod-like Au-rich phase. (b) EDS spectrum of the Au-rich phase. (c) SADP of the Au-rich phase with a zone axis of [001].
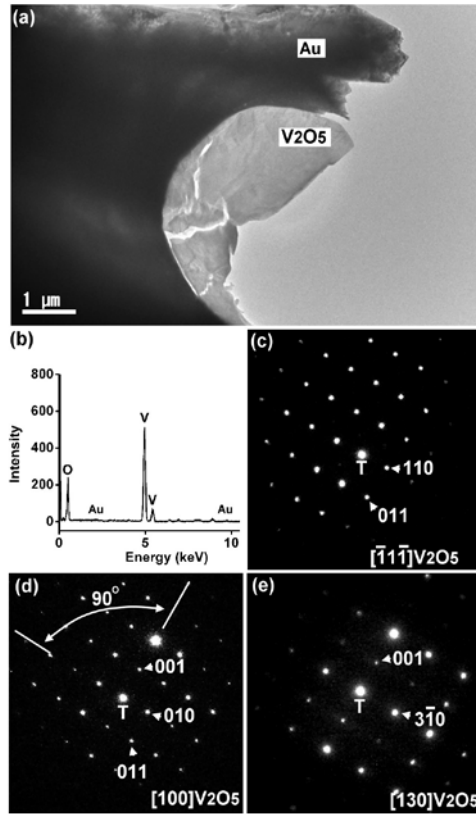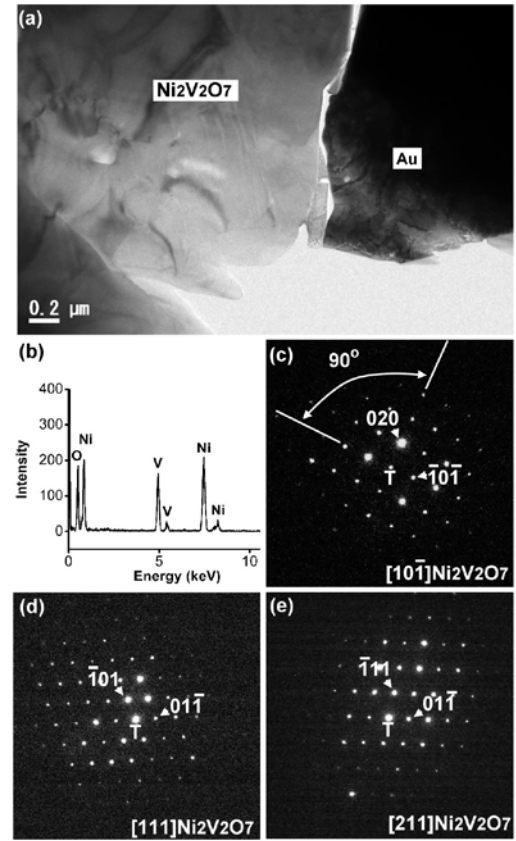

97.5Au-0.75Ni-1.75V

Glue Glue

NDL   COMPO 15.0kV X500   10μm   WD 8.5mm

Fig. 2 Scanning electron micrographs (backscattered electron image, BEI) of the cross-sections of the 97.5Au-0.75Ni-1.75V interlayer after oxidation at 850ºC for 200 min. Several irregularly shaped particles are distributed over the 97.5Au-0.75Ni-1.75V interlayer.

(a) Au

V_2O_5

1 μm

(b)

(c)

$[\bar{1}1\bar{1}]V_2O_5$

(d) 90°

001

010

011

$[100]V_2O_5$

(e)

001

$3\bar{1}0$

$[130]V_2O_5$

Fig. 3 (a) Transmission electron micrograph (bright-field image, BFI) of the 97.5Au-0.75Ni-1.75V interlayer after oxidation at 850ºC for 200 min, indicating the loose V_2O_5 phase formation. (b) EDS spectrum of V_2O_5. (c−e) SADPs of V_2O_5 with the zone axes of [$\bar{1}1\bar{1}$], [100], and [130], respectively.

(a)

Ni2V2O7

Au

0.2 μm

(b)

(c) 90°

020

$\bar{1}01$

$[10\bar{1}]Ni2V2O7$

(d)

$\bar{1}01$

$01\bar{1}$

$[111]Ni2V2O7$

(e)

$\bar{1}1\bar{1}$

$01\bar{1}$

$[211]Ni2V2O7$

Fig. 4 (a) Transmission electron micrograph (bright-field image, BFI) of the 97.5Au-0.75Ni-1.75V interlayer after oxidation at 850ºC for 200 min,, indicating the $Ni_2V_2O_7$ phase. (b) EDS spectrum of $Ni_2V_2O_7$. (c−e) SADPs of $Ni_2V_2O_7$ with the zone axes of [$10\bar{1}$], [111], and [211], respectively.

- 54 -

EFFECT OF ALLOY ADDITION ON THE STRUCTURE OF INTERPHASE PRECIPITATION FOR NANOMETER-SIZED CARBIDE STRENGTHENED DUAL PHASE STEELS

[1]TSAI, Shao-Pu(蔡劭璞), [1]SU, Te-Cheng(蘇德徵), [1]CHENG, Chih-Hung(鄭至閎), [1]HUANG, Bo-Ming(黃柏銘), [2]HUANG, Ching-Yuan(黃慶淵) and [1]YANG, Jer-Ren(楊哲人)

[1]Department of Materials Science and Engineering, National Taiwan University, Taipei, Taiwan
[2]R&D Department, China Steel Corporation (CSC), Kaohsiung, Taiwan

The dual-phase steel, which is typically the microstructural combination of ferrite matrix and island martensite, is viewed as the potential of new-generation steel because of its ultrahigh strength, high strength/weight ratio and good formability. However, dual phase steel suffers the problem of bad hole-expansion property. X. Fang et al. [1] proposed that reducing the difference between yield strength and ultimate tensile strength can effectively improves hole-expansion property, thus improving the mechanical properties of dual phase steels. Therefore, this research aimed to enhance ferrite strength through the nanometer-sized interphase precipitation [2], whose structure could be affected by the hardenability of steel. This study compared the ferrite transformation behavior of Cr steel and Al steel (alloy designation listed in Table 1) to investigate the effects alloy on the mechanical properties and interphase precipitation structure (as in Fig.1). It's found that Al will raise the transformation rate of ferrite, while Cr alloy have the opposite effect. Besides, Al steels shows lower hardness, which could be attributed to the lower precipitation density than Cr steels. This study conclude that lower isothermal holding temperature and lower ferrite transformation rate give rise to the higher strengthening contribution of interphase precipitation.

References
1. X. Fang, Z. Fan, et al., *Journal of Materials Science*, 2003, 38(18), pp.3877-3882.
2. R.W.K. Honeycombe, *Metallurgical Transactions A*, 1976. **7**(7), p. 915.

Table 1. Chemical composition of steel plates investigated (wt.%)

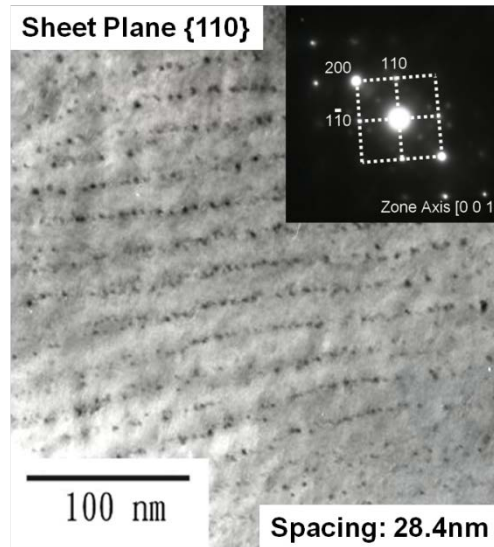|	Fe	C	Si	Mn	Cr	P	Al	Ti	N
Cr Steel	Bal.	0.1	0.1	1.5	0.6	0.04	-	0.2	trace
Al Steel	Bal.	0.1	0.1	1.5	-	0.04	0.1	0.2	trace

Figure 1. Morphology of interphase precipitation of Al steel austenized at 1050℃ and isothermal held at 650℃ for 8 seconds. The sheet spacing of precipitation is measured as 28.4nm, and sheet plane belongs to {110}.

THE EMBRITTLEMENT OF ANNEALED AMORPHOUS FE$_{81}$SI$_2$B$_{17}$ ALLOY RIBBON

[1]CHEN, Po-Yu (陳伯宇), [1]Lee, Hsin-Yi（李欣怡）and [1]Yang, Jer-Ren（楊哲人）

[1]Department of Materials Science and Engineering, National Taiwan University, Taipei, Taiwan

The application of the iron-based amorphous alloys for use as magnetic core in transformers is very attractive because of their superior magnetic characteristics and much lower core loss. To further improve the soft magnetic properties such as low coercivity and high permeability, the as-cast amorphous ribbon needs to be annealed at an appropriate temperature (below crystallization temperature) under magnetic field for a suitable period. However, after annealing treatment, the amorphous ribbon turns to be brittle, which is disadvantageous to application.

In this work, the embrittlement behavior of Fe$_{81}$Si$_2$B$_{17}$ amorphous ribbon annealed at 275 - 425ºC for 60 min was investigated by bend test, thermal analysis, and electron microscopy. The crystallization temperature (T_x) and ductile-brittle transition temperature (T_{db}) of Fe$_{81}$Si$_2$B$_{17}$ ribbon were determined to be 425 ºC and 325ºC respectively. The fracture surfaces of the ribbons treated at various annealing temperature (T_a) were investigated by FEG-SEM. It was found that when the ribbon was annealed at $T_a < T_{db}$, its thickness was shrink from 20 μm to 10 μm before fracture and vein structure was observed in the fracture surface. When annealed at $T_a > T_{db}$, the ribbon showed no obvious deformation in cross-section area and directly cracked after bending. In those annealed at $T_a > T_{db}$ ribbons, different characteristic morphologies along the crack propagation were observed: river-pattern zone, mist zone, striation zone and mirror zone. This characteristic fracture morphology was independent of annealing temperature when $T_x > T_a > T_{db}$. After crystallization, the mirror-like fracture surface of annealed ribbon was distributed with few dendrite crystals and the ribbon was totally brittle. The severe embrittlement behavior was found in the crystalline ribbon. For the case of the annealing temperature below T_x, the embrittlement phenomenon could be ascribed to the short range ordering.
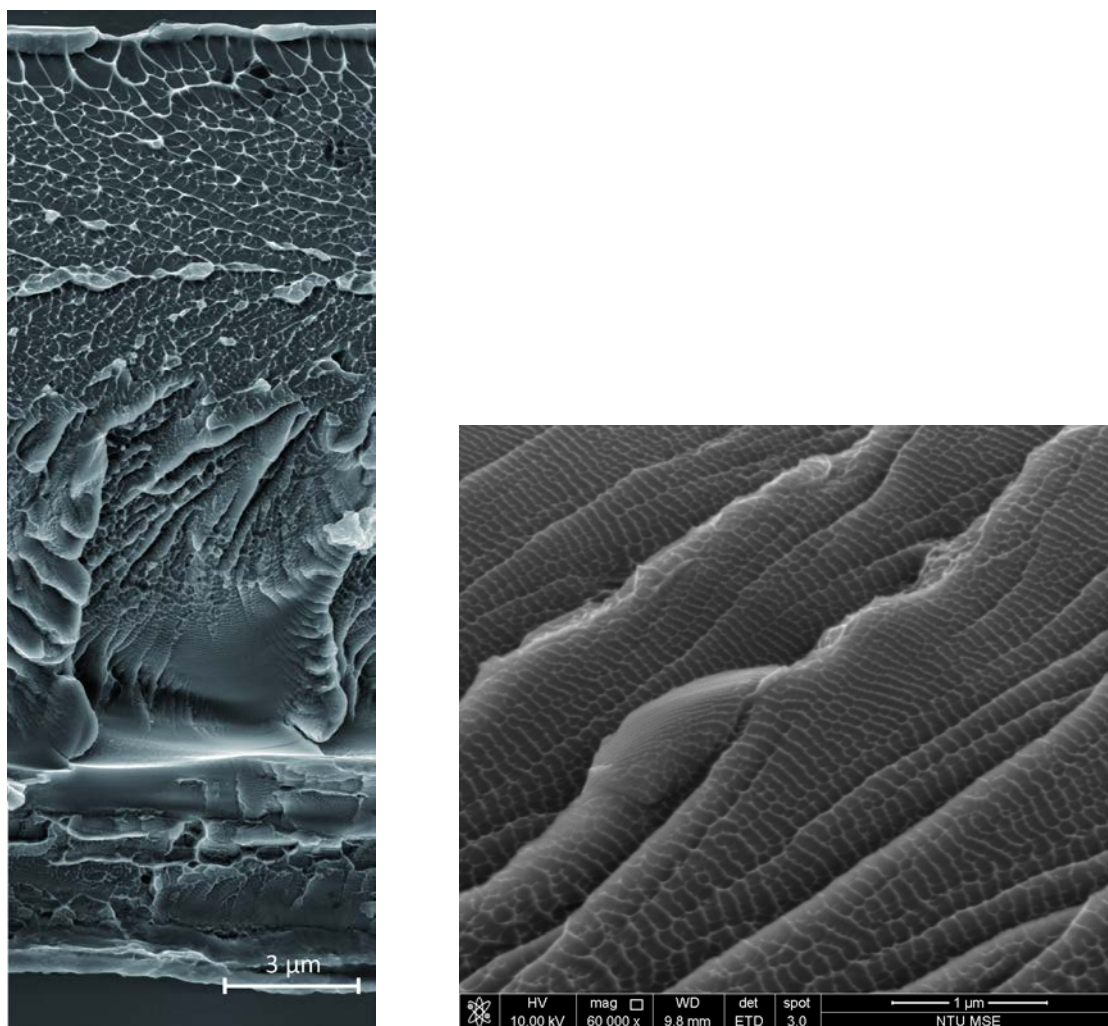
Figure 1 The fracture surface of the amorphous Fe-based ribbon which is annealed at 325°C for 60 min.

ATOMIC-SCALE PROBING OF INTERDIFFUSION AND A LOCALIZED TWO-DIMENSIONAL ELECTRON DENSITY AT AN INSULATING OXIDE INTERFACE

CHANG, Ching-Pin(張景斌),[12] LIN, Jauyn Grace(林昭吟),[2] CHENG, Su-Ling(鄭淑齡),[12] YANG, Jer-Ren(楊哲人),[1] CHU, Ming-Wen(朱明文),[2] and CHEN, Cheng-Hsuan(陳正弦)[2]

[1] Department of Materials Science and Engineering, National Taiwan University, Taipei, Taiwan

[2] Center for Condensed Matter Sciences, National Taiwan University, Taipei 106, Taiwan

Upon joining the non-polar TiO_2 plane of $SrTiO_3$ with the polar atomic plane of an insulating oxide, the heterojunction interface could become metallic. The context of this exotic physics has been known as electronic reconstruction and largely described by the charge transfer from the polar to non-polar planes, forming interfacial two-dimensional electron gas. We explored this wisdom through mixed-valence $(Nd_{0.35}Sr_{0.65})MnO_3$ on TiO_2-terminated $SrTiO_3$, manifesting a primitively polar-discontinuous $(Nd_{0.35}Sr_{0.65}O)^{0.35+}$-$(TiO_2)^0$ interface, while being electrically insulating. Using atomic-plane-by-atomic-plane chemical quantifications and spectroscopy in an aberration-corrected electron microscope, unexpectedly charge transfer across the insulating interface does exist, whereas inversely into $(Nd_{0.35}Sr_{0.65})MnO_3$. The intricate electronic correlations and interfacial strain envisaged by $(Nd_{0.35}Sr_{0.65})MnO_3$ drive the charges otherwise localized, leading to a counter-intuitive inverse charge transfer with an insulating character, in distinct contrast to the electronic-reconstruction framework. Correlations physics underlining this unexpected inverse electronic reconstruction were atomically tackled with new interface-property perspectives.

SURFACE EXCITON POLARITON IN MONOCLINIC HFO₂: ELECTRON ENERGY-LOSS SPECTROSCOPY STUDY

CHU, Ming-Wen(朱明文),[1] LIOU, Sz-Chian(劉思謙),[1] LEE, Yi-Jun(李毅君),[2] HONG, Ming-Hwei(洪銘輝),[2] KWO, Ray-Nien(郭瑞年),[3] and CHEN, Cheng-Hsuan(陳正弦)[1]

[1] Center for Condensed Matter Sciences, National Taiwan University, Taipei 106, Taiwan

[2] Department of Materials Science and Engineering, National Tsing Hua University, Hsinchu 300, Taiwan

[3] Department of Physics, National Tsing Hua University, Hsinchu 300, Taiwan

We have recently revisited the conventional understanding in surface exciton polaritons (SEPs) and established their excitations in materials displaying an otherwise weak excitonic oscillator strength [1]. The existence of SEPs is thus not limited to materials with a sharp excitonic absorption [2], and the collective nature of SEPs upon weak excitonic absorption originates from oscillations of loosely defined delocalized excitons, which are correlated with broad interband transitions in materials (e.g., Figure 1). The weak excitonic absorption and the associated interband transitions can be observed in practically all semiconductors and insulators above the band gap, suggesting the existence of SEPs in the materials. Using scanning transmission electron microscope (STEM) in conjunction with electron energy-loss spectroscopy (EELS) with an ultimate spatial resolution of 0.2-2 nm, we have firmly established the existence of SEP (~7.5 eV) in monoclinic, insulating HfO_2 upon the weak excitonic excitation, ~6.2 eV, above the optical band gap (~5.1 eV), Figure 1. Interband transitions can be found in almost all semiconductors and insulators above the band gap, and this work could stimulate future interests in SEPs in various materials, where the SEP excitations may find unexpected optics applications via manipulations of their surface wave fields analogous to surface plasmons for plasmonics.

References
1. M.-W. Chu et al., *Phys. Rev. B* 77 (2008) 245402.
2. F. Yang et al., *Phys. Rev. Lett.* 64 (1990) 559.
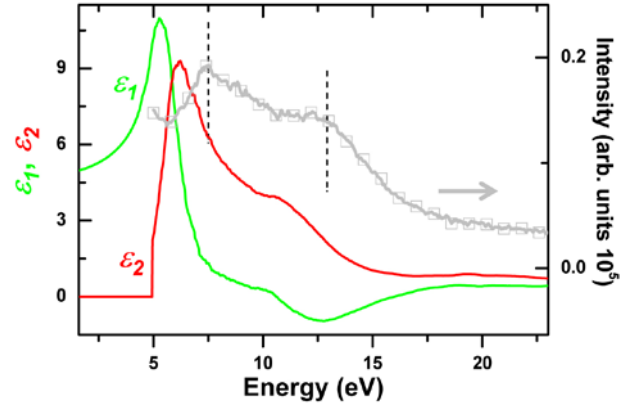
Figure 1. The real (ε_1) and imaginary parts (ε_2) of the complex dielectric function of monoclinic HfO$_2$, displaying a broad, weak excitonic absorption (maximum in ε_2) at ~6.2 eV above the optical band gap. SEP onset at ~7.5 eV and that for surface plasmon (SP) at ~13.4 eV are indicated by dashed lines. Gray, STEM-EELS excitations of SEP and SP taken at 4 nm from the surface of an HfO$_2$ bulk ceramic.

SURFACE EXCITON POLARITONS IN INDIVIDUAL AU NANOPARTICLES IN THE FAR-UV SPECTRAL REGIME

CHU, Ming-Wen(朱明文),[1] CHEN, Cheng-Hsuan(陳正弦),[1] F. Javier García de Abajo,[2] DENG, Jin-Pei(鄧金培),[3] and MOU, Chung-Yuan(牟中原)[4]

[1] Center for Condensed Matter Sciences, National Taiwan University, Taipei 106, Taiwan

[2] Instituto de Óptica CSIC and Unidad Asociada CSIC-Universidade de Vigo, Serrano 121, 28006 Madrid, Spain

[3] Department of Chemistry, Tamkang University, Taipei County 25137, Taiwan

[4] Department of Chemistry, National Taiwan University, Taipei 106, Taiwan

Interests in surface excitations of Au are mainly focused on the well-known surface plasmon (SP) in the visible spectral regime [1]. The existence of surface exciton polaritons (SEPs) is believed to be pristine to the spectral regimes showing strong excitonic absorptions [2]. The presence of SEPs in far-UV in Au (≥ 10 eV), where the optical and electronic properties of Au are dominated by broad interband transitions that display characters of weak and diffused excitonic oscillator strengths, is not expected and has never been discussed. Reexamining Ref. 2 and using electron energy-loss spectroscopy (EELS) with a 2-Å electron probe in aloof (optical near-field) setup and energy filtered mapping (Figure 1), we firmly establish the existence of SEPs in individual Au nanoparticles in the far-UV spectral regime [1]. These results indicate that SEPs indeed can be excited in weak excitonic onsets in addition to their general believing for the sharp excitonic oscillations. Our experimental observations are further confirmed by the theoretical calculations of EELS spectra. The unmatched spatial resolution (2 Å) of the electron spectroscopy technique enables an investigation of individual nanomaterials and their surface excitations in aloof setup. The SEPs in individual Au nanoparticles thus represent an example of surface excitations of this type beyond the visible spectral regime and could stimulate further interests in SEPs in various materials and applications in novel plasmonics and nanophotonics at high energies via manipulations of the associated surface near fields.

References
1. M.-W. Chu et al., *Phys. Rev. B* 77 (2008) 245402.
2. F. Yang et al., *Phys. Rev. Lett.* 64 (1990) 559.
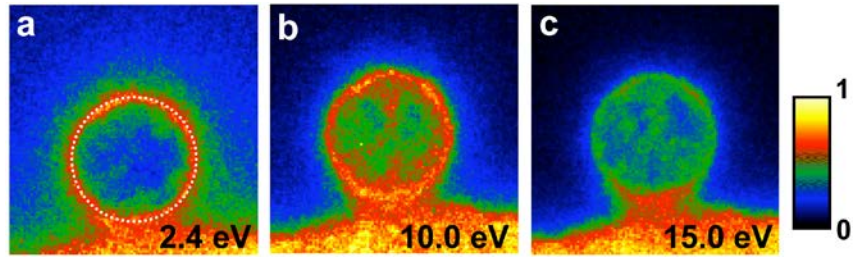
Figure 1. (a) EELS mapping of SP near fields in an individual Au nanoparticle (radius, 13 nm; dotted circle, the projected surface of the nanoparticle). The intensity maximum encircling the surface is well known to signify the surface-excitation nature, which is also observed in (b) and (c) for SEP excitations in Au in the far-UV spectral regime (10.0 and 15.0 eV, respectively). Reproduced from [1].

STEM-EELS/EDS STUDIES OF ULTRA-THIN 4.5nm NICKEL SILICIDE FILMS

Wu, Chien-Ting(吳建霆),[1] Lee, Yao-Jen(李耀仁),[1,2] Hsueh, F.-K.(薛富國),[1] Sung, P.-J. (宋柏融),[1] ChloT.-C.(卓大鈞),[3] Current, M. I.,[4] and Chao, Tien-Sheng(趙天生)[3]

[1]National Nano Device Laboratories, Hsinchu City, Taiwan.
[2]Department of Physics, National ChungHsing University, Taichung, Taiwan.
[3]Department of Electrophysics, National Chiao Tung University, Hsinchu, Taiwan.
[4]Current Scientific, San Jose, CA 95124 USA.

We demonstrate a novel silicidation process that forms Ni silicide thin films in a thickness of 10 nm while maintaining a low sheet resistance (Rs) of 18 ohm/sq. with two-step low temperature microwave annealing (MWA). Using this two-step method, an ultra-thin Ni silicide film, as thin as 4.5 nm, can be fabricated. Ni films were pre-deposited on Si wafers by the physical vapor deposition (PVD) method. A thin NiSi layer (Ni: ~54%) with partial crystalline was formed by the first MWA step, as shown in Fig. (a). After removing the unreacted metal (Ni rich layer, Ni: >93%) by selective wet etching, the second MWA step was performed to reduce the Rs of the NiSi layer. Figures 1(b~c) show the HRTEM images of the NiSi film of 4.5 nm, 10 nm and 16 nm in thickness. In our previous experience, it is easy to form $NiSi_2$ nanoclusters in the silicide layer after the RTA or MWA process at higher temperature for thinner silicide layers. Figure 2(a) shows a 4.5 nm NiSi thin film formed with some small epitaxial $NiSi_2$ (10~20 nm) regions on Si surface without the formation of the pyramids structure, but this phenomenon is not observed in the 10 nm and 16 nm NiSi films. It should be noted that the high resistance $NiSi_2$ phase in the form of nano-islands is one of the factors, other than the thickness effect, that 4.5 nm NiSi layer presents a higher Rs (50 ohm/sq.) than that of the 10 nm (18 ohm/sq.) thick layer. The structural identification and the distribution of $NiSi_2$ phase in the NiSi layer are also performed in this study. We use electron energy-loss spectroscopy and energy dispersive X-ray spectroscopy in the scanning transmission electron microscopy mode (STEM-EELS/EDS) to identify the nickel silicide phases. Atomically-resolved Z-contrast images, elemental analysis, and the bulk Plasmon excitations are used to identify the phases of nickel silicides [1, 2], as shown in Fig. 2.

References

1. E. Verleysen, H. Bender, O. Richard, D. Schryvers and W. Vandervorst, *J Mater Sci 46,* (2011)2001-2008.
2. N. Kawasaki, N. Sugiyama, Y. Otsuka, H. Hashimoto, M. Tsujimoto, H. Kurata and S. Isoda, *Ultramicroscopy 108*, (2008) 399-406.
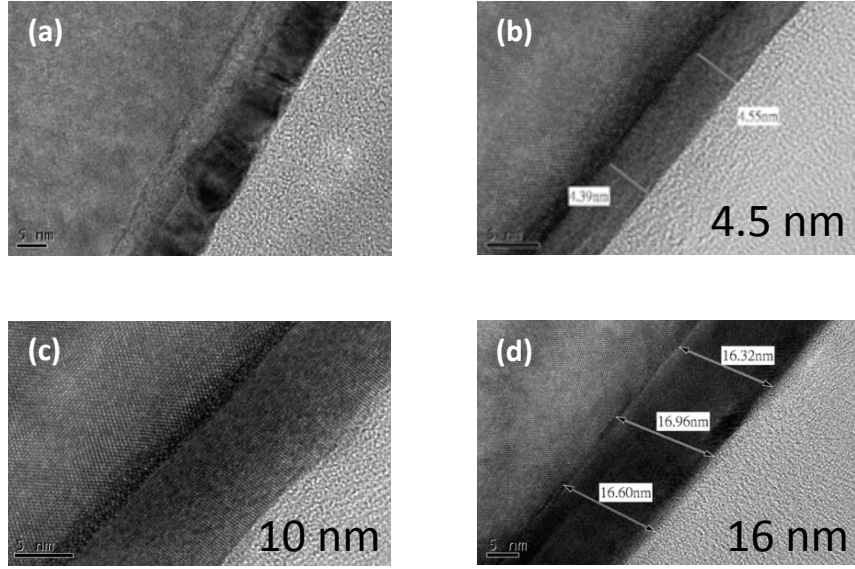
Figure 1. HRTEM images of (a) NiSi film after first step MWA. (b) 4.5 nm NiSi film. (c) 10 nm NiSi film. (d) 16 nm NiSi film.
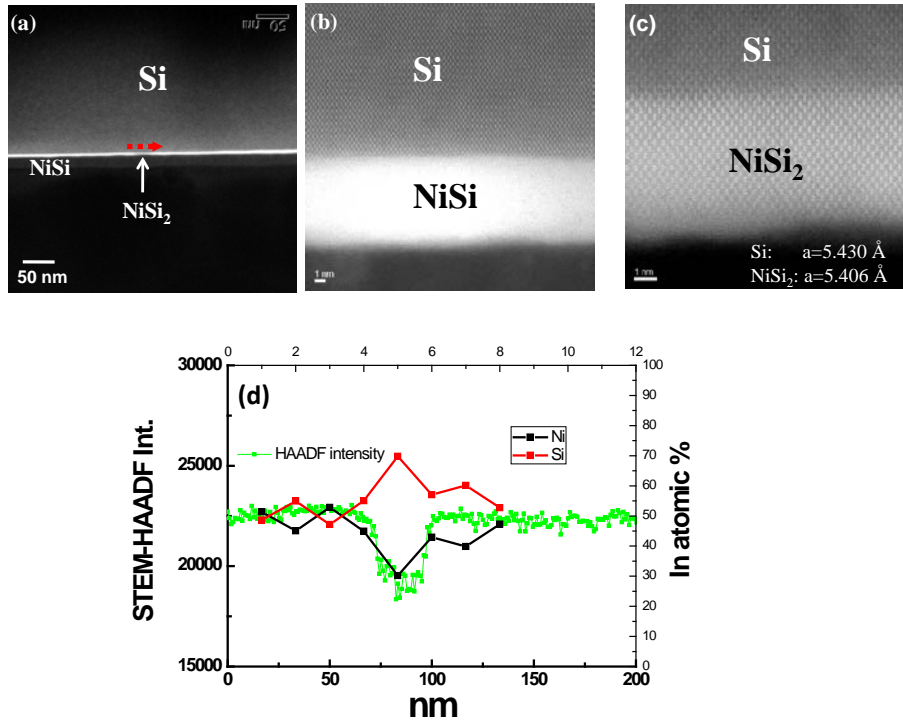
Figure 2.(a-c) STEM-HAADF images of the 4.5 nmNiSi layer. (d)Line-profiles of STEM-HAADF intensity and elemental compositions in (a).

ACCELERATION OF NANO-STRUCTURED BAINITE BY TWO STEP HEAT TREATMENT

TSAI, Yu-Ting (蔡宇庭),[1] HUANG, Ching-Yuan (黃慶淵)[2] and YANG, Jer-Ren (楊哲人)[1]

[1]Department of Materials Science and Engineering, National Taiwan University, Taipei, Taiwan
[2]Iron and Steel R&D Department, China Steel Corporation

Nano-structured bainite is promising for ultra-high strength applications. The microstructure is carbide free, and is composed of fine bainitic ferrite and retained austenite films of nanometer size. Excluding heavy thermo-mechanical processing for conventional steels of the same grade, the heat treatment of nano-structured bainite is inexpensive and simple, which involves only direct quenching to isothermal holding temperature for bainite transformation. However, due to low homologous temperature used, transformation rate is sluggish. Various attempts have been used for acceleration of bainite transformation, including temperature cycling, fine-grained austenite and judicious addition of expensive alloying element, but however, no distinguished results were reported. In this study, inspired by recent quenching and partitioning (Q&P) process concepts, we attempted a two-step heat treatment on nano-structured bainite alloy, and significant acceleration of bainite transformation due to partial martensite is found. TEM results indicated that martensite and bainitic ferrite exhibited similar orientation, suggesting that partial martensite formation probably could induce the formation of similarly oriented bainitic ferrite, resulting in acceleration of bainite transformation.

References

F. G. Caballero, *Mater. Sci. Technol.* 17 (2001) 512

H.S. Hasan, *Mater. Sci. Technol.* 26 (2010) 453

C. Garcia-Mateo, *ISIJ Int*. 43 (2003) 1821

S. Khare, Mater. *Metall. Mater. Trans. A*. 41, 922 (2010)
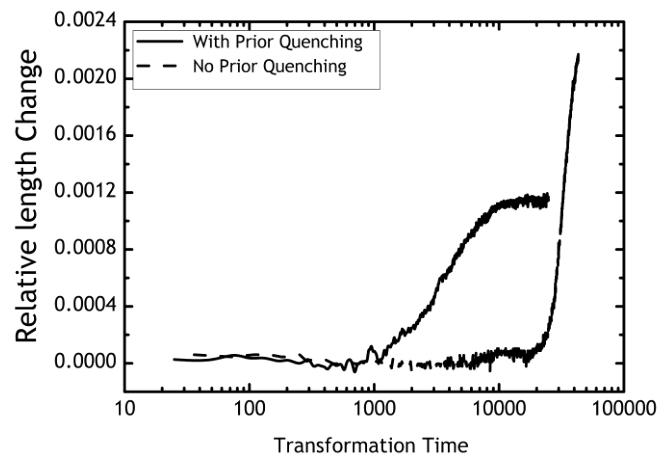
Figure 1. dilatometry results shows that with two step transformation, bainite transformation can be greatly accelerated.
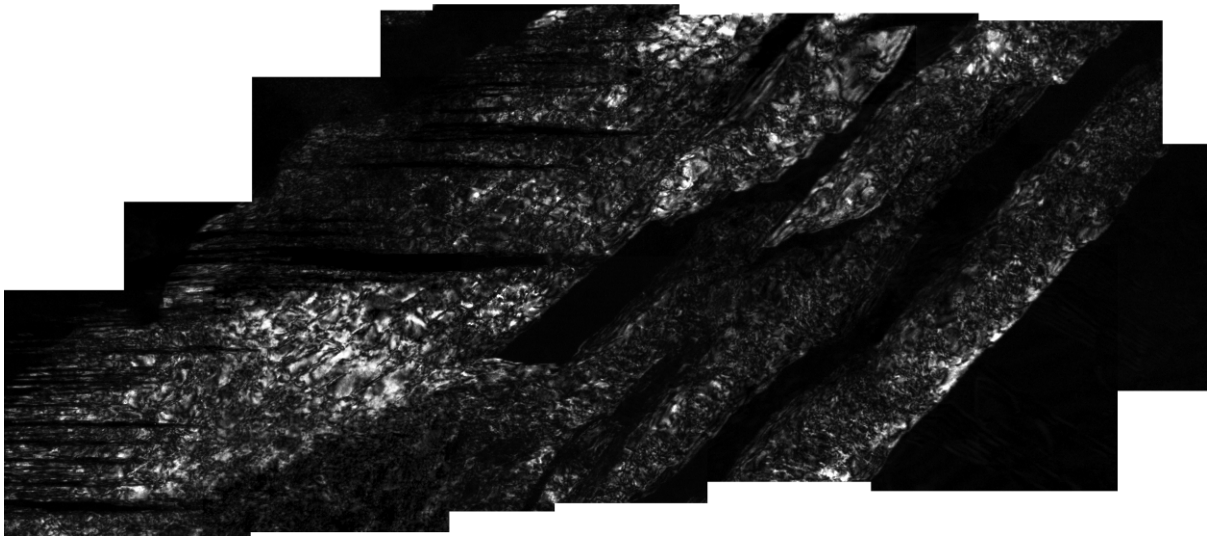
Figure 2. The dark field image shows tempered twinned martensite (on the left hand side) and adjacent bainite. They are similarly orientated.

RETAINED AUSTENITE STABILIZATION AND ITS EFFECT ON TOUGHNESS OF A LOW CARBON LOW ALLOYED STEEL BY TWO-STEP INTERCRITICAL TREATMENT

[1]XIE, Zhen-Jia (謝振家), [1]YUAN, Sheng-Fu (袁勝福), and [1]SHANG, Cheng-Jia (尚成嘉)

[1]School of Materials Science and Engineering, University of Science and Technology Beijing, Beijing, China

Recently, low temperature toughness has been given more attentions and becomes more significant to low carbon low alloyed high performance steel, due to its potential applications in severe service environment. However, it is so difficult to achieve excellent impact toughness combined with high strength, especially at a certain low temperature. Previous work has suggested that stable face-centre-cubic (FCC) austenite is benefit for both ductility and toughness, especially for lowering ductile-brittle transition temperature (DBTT)[1-5]. In this work, two-step intercritical heat treatment after pre-quenching was performed on a Fe-0.08C-0.5Si-2.4Mn-0.5Ni-0.3Mo-0.1Nb-0.02Ti (wt%) steel, and ultra-fine complex microstructure of intercritical ferrite, tempered/annealed martensite and film-like meta-stable retained austenite was obtained. The results from scanning electron microscopy(SEM), transition electron microscopy(TEM), dilatometery and X-ray diffraction(XRD) analysis show that, the first intercritical annealing produces mixture microstructures of intercritical ferrite and preliminary alloy-enriched martensite, which has a lower A_{c1}(designated as A_{c1}')[6]. During the following intercritical tempering above the A_{c1}', fine reversion austenite films form along martensite laths and are fully thermal-stabilized to room temperature by further partition of carbon and manganese. The intercritical tempering temperature is important for reversion austenite stabilization. The meta-stable film-like retained austenite is good for low temperature toughness.

References

1. F.G. Caballero, H.K.D.H. Bhadeshia, *Current Opinion in Solid State and Materials Science* 8 (2004) 251-257.
2. J.I. KIM, C.K. SYN, J. W. MORRIS, Jr., *Metall. Trans A* 14 (1981) 1983-93.
3. C. N. Ahlquist, *Acta Metall.* 23 (1975) 239.
4. K. J. KIM, *Mater. Sci. Eng.* 33 (1978) 5-20.
5. S. D. Antolovich, B. Singh, *Metall. Trans.* 2 (1971) 2135.
6. W.H Zhou, H. Guo, Z.J. Xie, X.M. Wang, C.J. Shang, *Mater. Sci. Eng. A* 2013, accepted.
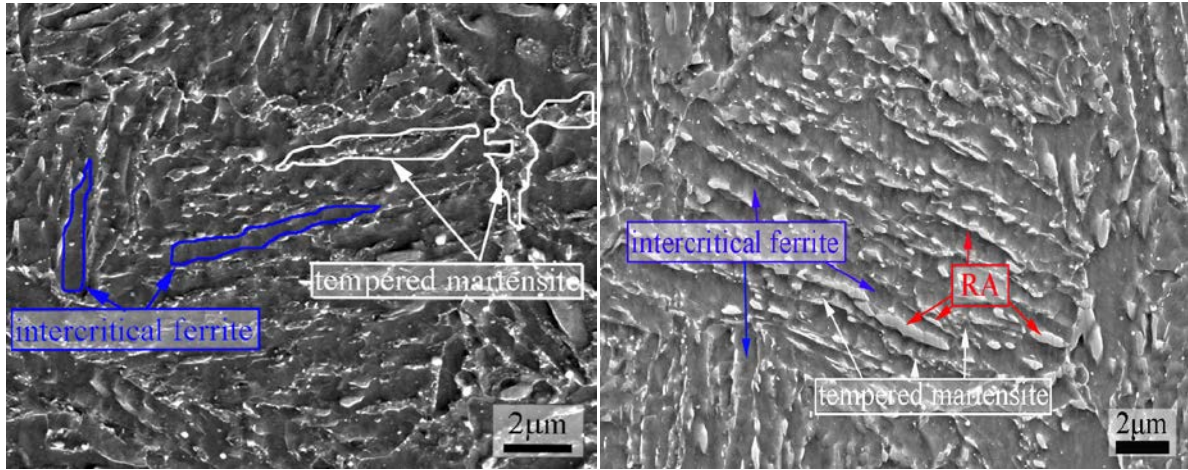
Figure 1. SEM micrographs: (a) intercritical ferrite and tempered martensite after tempered at 600℃, (b) intercritical ferrite, tempered martensite and retained austenite after intercritical tempered at 680 ℃, (both samples were tempered following intercritical annealed at 740℃ after pre-quenching.
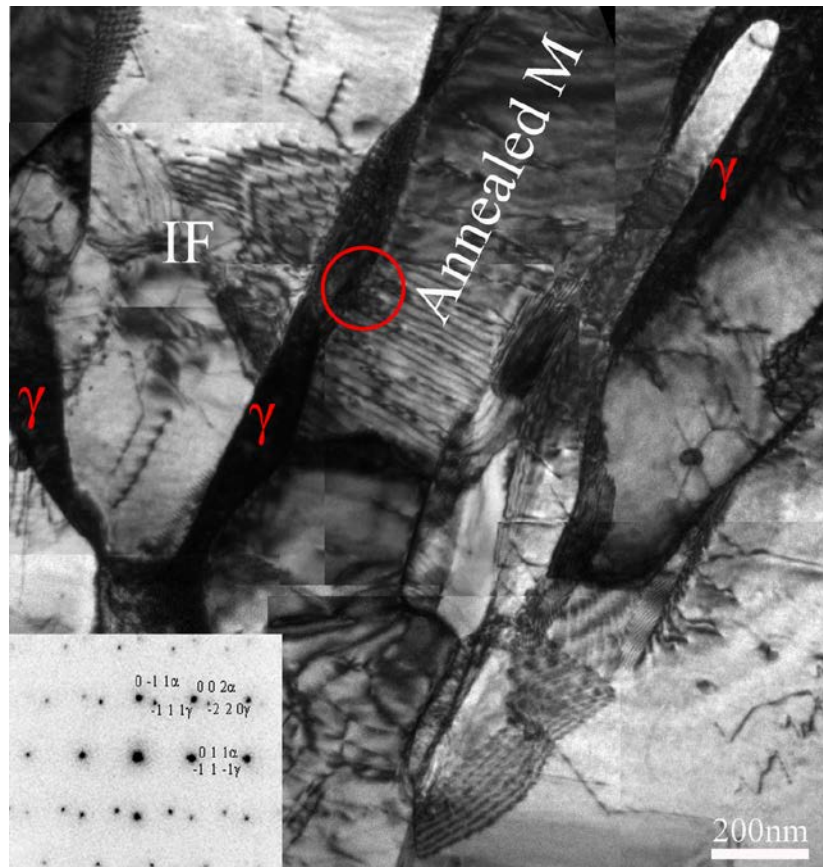
Figure 2. TEM observed the film-like between intercritical ferrite and annealed martensite, N-W orientation relationship can be observed between reversion austenite and annealed martensite.
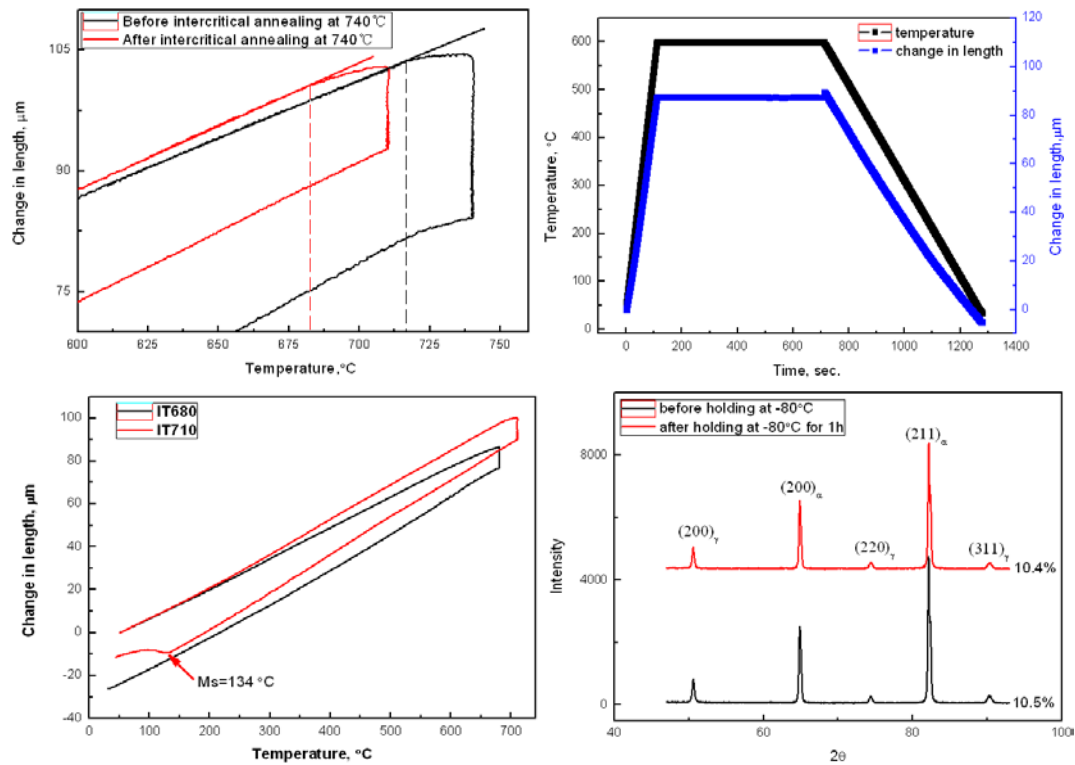
Figure 3. Dilatometer curve showing phase transformation: (a) Ac1 was lowed to 680℃ from 710℃ after the first step intercritical annealed at 740℃, (b) no obvious reversion austenite formed during tempering at 600℃，(c) reversion austenite formed at 710℃ transformed to martensite, while no transformation occurred for that formed at 680℃, (d) no change revealed that retained austenite obtained by intercritical tempering at 680℃ can be stable even at -80℃.

MULTI-PHASE MICROSTRUCTURE AND NANO-SIZED PRECIPITATES IN A NB-BEARING AND COPPER-MICROALLOYED STEEL BY A TWO-STEP REVERSED HEAT TREATMENT

[1]ZHOU, Wen-Hao (周文浩), [1]XIE, Zhen-Jia (谢振家) [1]GUO, Hui (郭晖),
[1]WANG, Xue-Min (王学敏) and [1]SHANG, Cheng-Jia (尚成嘉)

[1]Department of Materials Science and Engineering, University of Science and Technology Beijing, Beijing, China

Complex microstructure with considerable content of retained austenite is considered to improve the mechanical properties of advanced steels. Different from the TRIP or Q&P processing, in which the FCC-phase is stabilized by the carbon atoms ejected from bainite or martensite during medium or low phase transformation process, the present work gives a new way to obtain retained austenite by stabilizing the reversed austenite. A two-step reversion treatment was applied for a Fe-0.1C-2.0Mn-0.78Si-0.78Al-0.078Nb-1.0Cu-1.0Ni-0.25Mo (wt%) steel. After annealing at 780°C for 30min, a tempering process at 660°C for 30min is followed. The final microstructure is consisted of tempered bainite, lamellate ferrite, fine retained austenite and a small quantity of bainite or martensite. Meanwhile, nano-sized Nb precipitates and Cu-enriched particles were observed in the ferrite after the tempering process. By combination the multi-phase microstructure, retained austenite and nano-sized precipitates, the excellent mechanical properties (yield strength>690MPa, Y/T ratio<0.85, CVN@-20℃ (3/4t)>90J) were obtained.
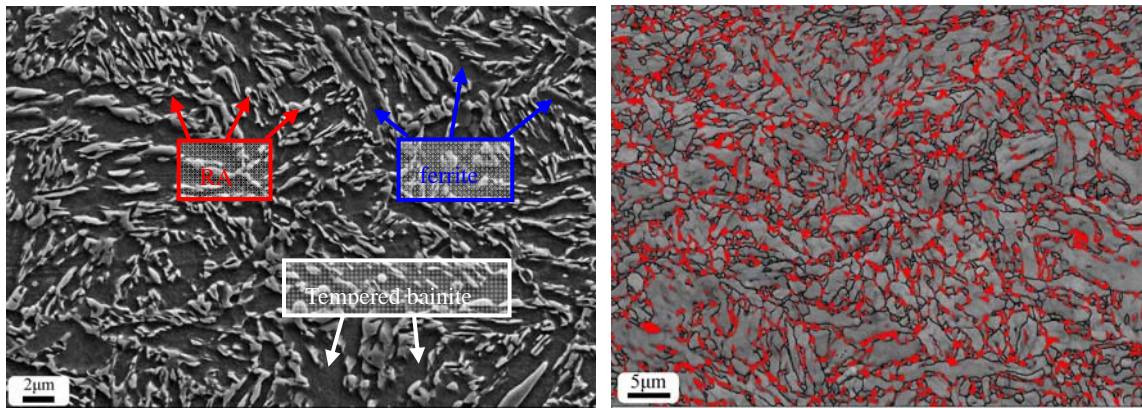
Figure 1. Multi-phase microstructure and retained austenite are shown in the SEM images and EBSD maps. (a) Microstructure consist of lamellate ferrite, tempered bainite matrix and retained austenite. (b) Dispersed retained austenite with fine size are represented by red colour.
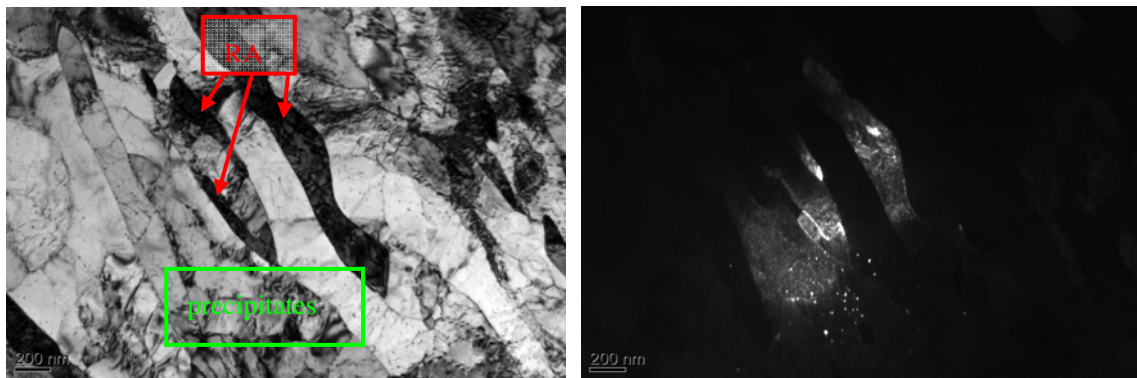
Figure 2 Retained austenite films form along the lamellate ferrite boundary, nano-sized precipitates disperse in the matrix.
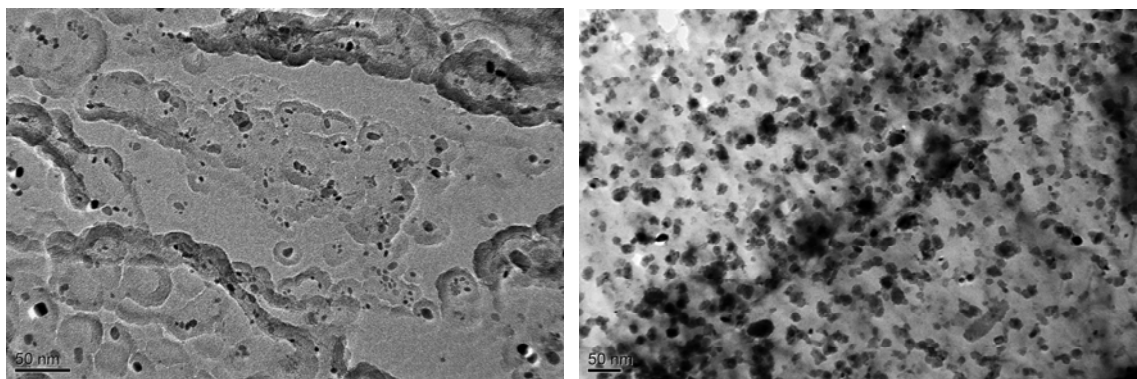
Figure 3 (a) Nb precipitates in the matrix (carbon replica sample) and (b) Nb and Cu precipitates with different sizes disperse in the matrix (foil sample)

ANNEALING BEHAVIOR OF COBALT-PHOSPHORUS ELECTRODEPOSITS

[1,2]CHEN, Fu-Je(陳黼澤), [1]LIN, Chao-Sung(林招松), [2]PAN, Yung-Ning(潘永寧) and [3]Lee, Chun-Ying(李春穎)

[1] Department of Materials Science and Engineering

[2] Department of Materials Science and Engineering, National Taiwan University, Taipei, Taiwan

[3] Department of Mechanical Engineering, National Taipei University of Technology, Taipei, Taiwan

Cobalt-Phosphorus (Co-P) coatings have many applications, such as mold industry, due to their excellence mechanical and corrosion resistance properties that are extensively used as protective coatings [1]. Such properties are best related to the composition and microstructure of the coatings. In general, the composition and microstructure of the Co-P electrodeposit strongly depend on the chemistry, temperature, and pH of the electrolyte. This study systematically investigated the annealing behavior, including microstructural evolution and mechanical properties of Co-4.5wt.%P deposits plated from cobalt sulfamate baths containing 5 g dm^{-3} phosphorous acid (H_3PO_3). Experimental results showed that annealing of Co-P deposits resulted in precipitation hardening [2] and a peak hardness was obtained at specific temperature ranges (Figure 1). The microstructure characterization revealed that the Co-P deposits underwent structural transformation at higher temperatures (Figure 2). HCP cobalt grain structure was transformed to a high temperature stable FCC austenite at temperatures above the allotropic temperatures of cobalt. As Co-P deposit was air cooled, a structure of HCP martensite coexisted with FCC austenite [3]. It is worth noting that high density annealing twins and stacking faults were found at the columnar grains (Figure 2). Both caused a grain refinement effect on the crystalline domains [4]. Thus, cobalt phosphorus alloys have superior mechanical strength at intermediate temperatures such as 400℃ ~ 500℃. However, Co-P deposit experienced recrystallization and grain growth at increased heat treatment temperatures that caused a reduction in the deposit hardness.

References

1. A. Brenner, *Electrodeposition of Alloys* (1963).
2. P. Choi, M. da Silva, U. Klement, T. Al-Kassab and R. Kirchheim, *Acta Materialia*, 53 (2005) 4473.
3. G. D. Hibbard, G. Palumbo, K. T. Aust and U. Erb, *Philosophical Magazine*, 86 (2006) 125.
4. G. Hibbard, K.T. Aust, G. Palumbo and U. Erb, *Scripta Materialia*, 44 (2001) 513.
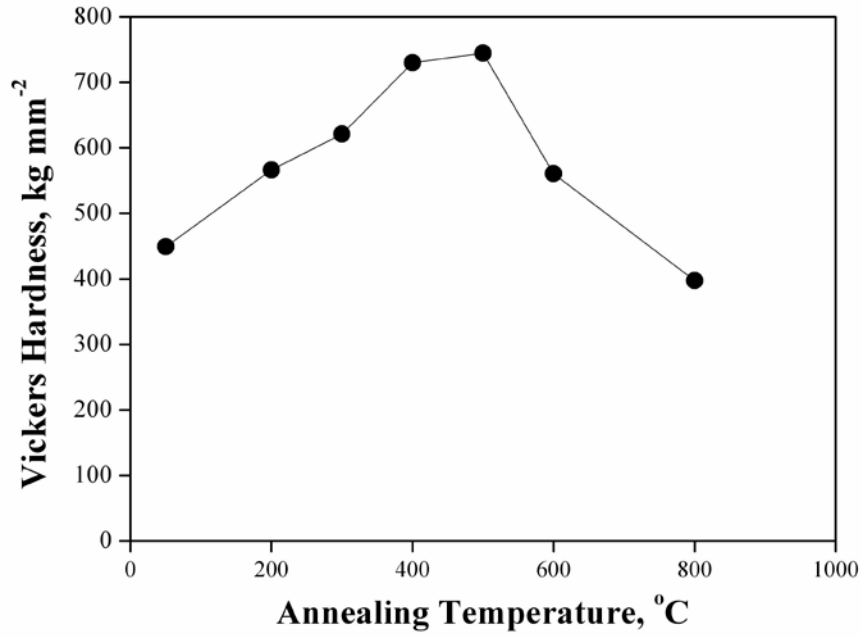
Figure 1. The hardness of the Co-P deposit as a function of annealing temperature.
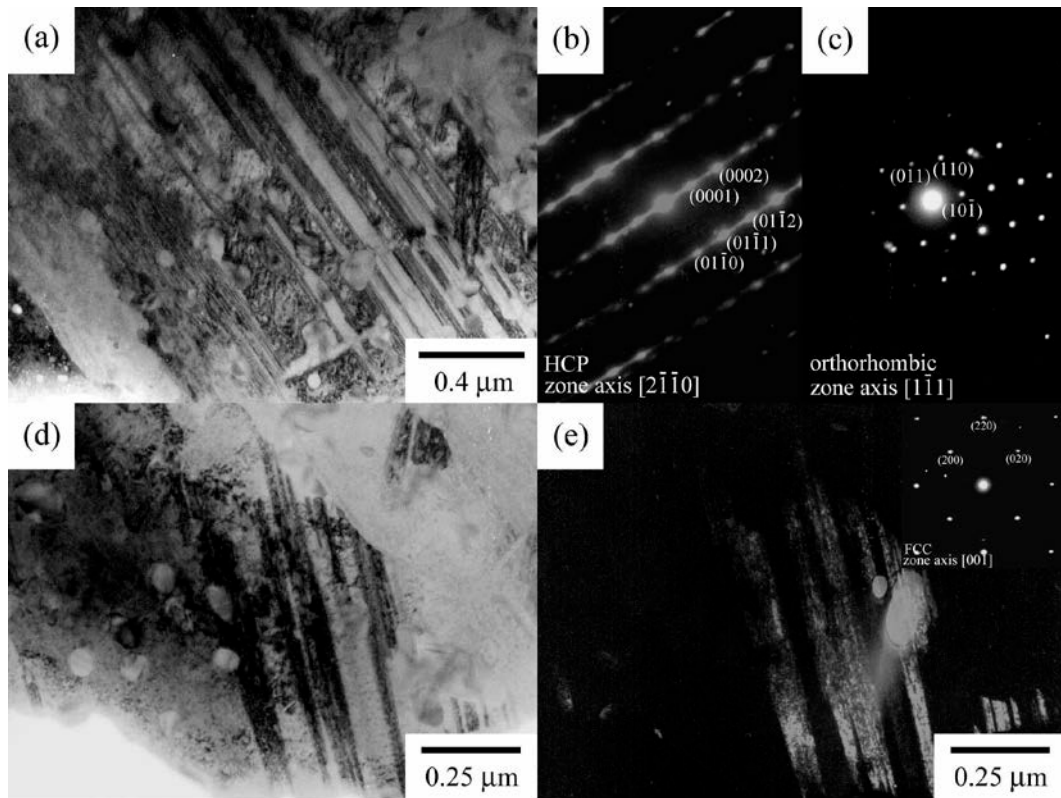

Figure 2. Microstructure characterization of Co-P deposit after annealing at 500℃ for 1 h: (a) bright-field image of HCP columnar grains, (b) selected area electron diffraction pattern of annealing twins, (c) selected area electron diffraction patterns of Co_2P precipitates, (d) bright-field image of FCC columnar grains, (e) dark-field image of FCC columnar grains.

MICROSTRUCTURAL CHARACTERIZATION OF THE LOW MELTING POINT GLASS-CERAMIC COMPOSITE COATING

CHEN, Fu-Je (陳黼澤) and LIN, Chao-Sung (林招松)

Department of Materials Science and Engineering, National Taiwan University, Taipei, Taiwan

Protective glass-based coatings have superior abrasive resistance, thermal insulation, corrosion resistance, and antioxidant properties at high temperatures, which are widely used in aircraft engines and gas turbine engine components [1,2]. The glass-ceramic composite coatings are polycrystalline solids with a residual glassy matrix, leading to a polycrystalline microstructure that imparts better performance to against abrasion and corrosion, as well as better toughness compared to the conventional glasses. The glass-based composite coatings producing process is to cool the molten material through the rapid solidification of liquid glass forming the amorphous phase. Subsequent appropriate annealing treatment results in phase separation and precipitation. The melting point of pure silica glass is about 1800℃ ~ 2000℃. Alkali metal oxides (eg. Na_2O, K_2O) and alkaline earth oxides (eg. MgO, CaO) are generally added as the flux to reduce the melting point of the glass system [3]. In this study, the microstructure of a glass-ceramic coating formed by thermal spray was detailed. Figure 1(a) shows the thermal spray method produced a dense and uniform coverage SiO_2-Na_2O-Al_2O_3 glass-based composite material. There were 10 to 100 μm spherical particles dispersing in the glass-ceramic protective layer. The cross-sectional TEM micrograph and XRD pattern showed that the SiO_2-Na_2O-Al_2O_3 composite coating consisted of amorphous phase and crystalline phase (Figure 1(b) and Figure 1(c)), in which the amorphous structure was mainly silica phase structure and the crystalline phase consisted of α phase SiO_2 (HCP), β phase SiO_2 (FCC), Na_2O (FCC) and α phase Al_2O_3 (orthorhombic). The microstructure characterization showed no boundary contrast and electron diffraction pattern of the composite coating confirmed that the parent phase was an amorphous structure (Figure 1(b)). The composition analysis of the amorphous phase was mainly silica, with small amounts of sodium, aluminum, calcium, cobalt and nickel. The crystalline precipitation phase was α phase SiO_2 (Figure 1(c)). The ratio of crystalline phase/amorphous phase and the microstructure determine the mechanical properties of the material, such as toughness, thermal stability, and corrosion resistance.

References

1. S. Datta and S. Das, *Bulletin of Materials Science*, 28 (2005) 689.
2. P. Liu, L. Wei, X. Zhou, S. Ye and Y. Chen, *Journal of Coatings Technology and Research*, 8 (2011) 149.
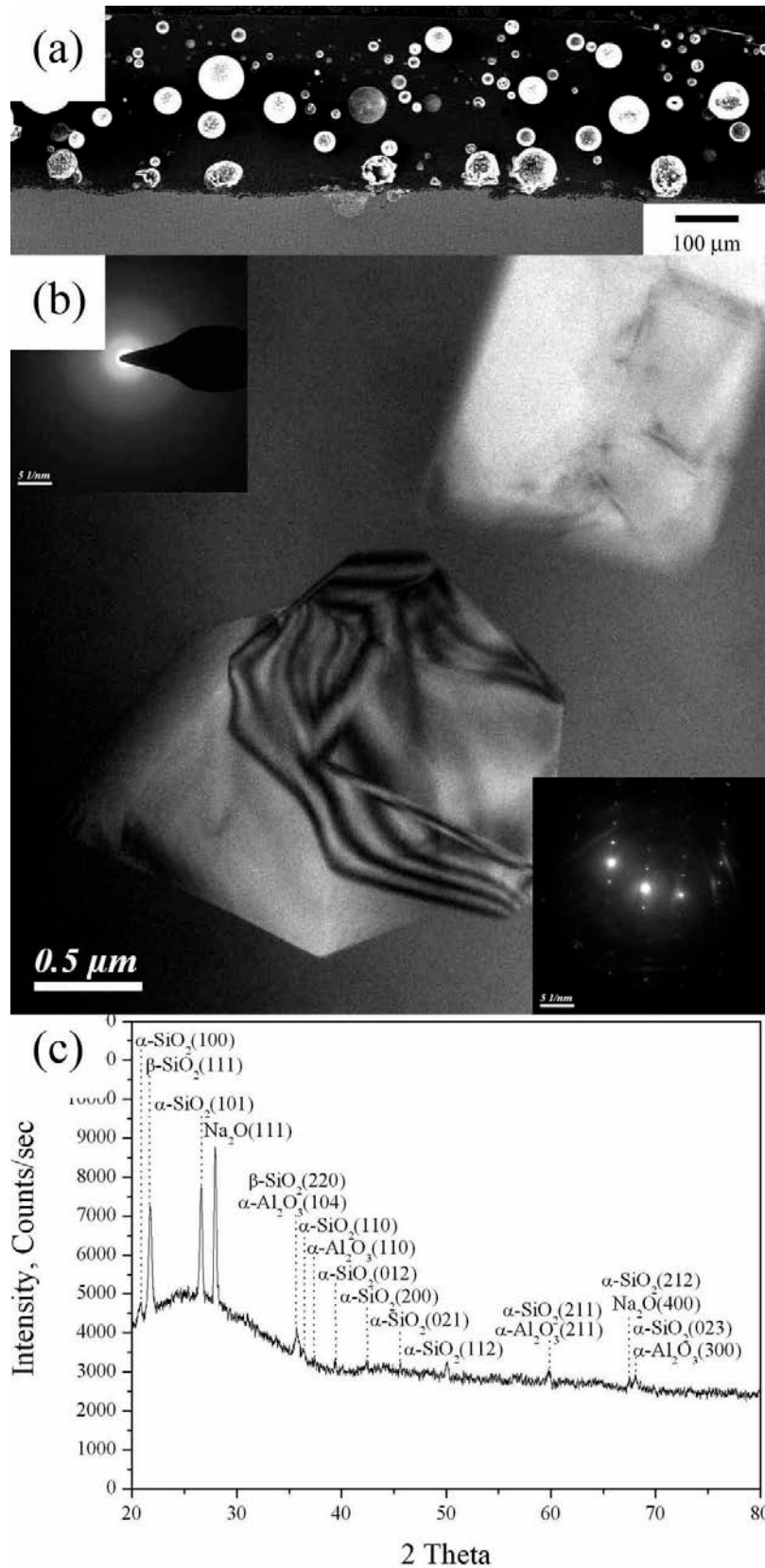3. A. R. Stetson, United States Patent 4,731,347 (1988).

Figure 1. Microstructural characterization of SiO₂-Na₂O-Al₂O₃ glass-ceramic composite coating: (a) cross-sectional SEM micrograph, (b) cross-sectional TEM micrograph and SAED pattern, and (c) XRD pattern.

INFLUENCE OF SURFACE OXIDATION ON THE VALENCE ELECTRON ENERGY-LOSS SPECTRUM OF WURTZITE ALUMINUM NITRIDE

Michael R. S. Huang (黃榮喜),[1] Rolf Erni,[2] and Chuan-Pu Liu (劉全璞) [1,]

[1] Department of Materials Science and Engineering, National Cheng-Kung University, Tainan 701, Taiwan

[2] Electron Microscopy Center, Empa, Swiss Federal Laboratories for Materials Science & Technology, 8600 Dübendorf, Switzerland

The influence of surface oxidation on the low-loss spectrum of aluminum nitride (AlN) is investigated in electron energy-loss spectroscopy with scanning transmission electron microscopy. Contrary to intrinsic bulk AlN, oxidized AlN exhibits considerable spectral broadening both in the full width at half maximum of bulk plasmon and the subsidiary features. The modification in the low-loss lineshapes because of oxidation significantly complicates the determination of the dielectric function intrinsic to AlN. Simulations based on dielectric theory qualitatively consist with the experimental results while incorporating thick oxide overlayers, further suggesting that the surface oxide of AlN can be rough and porous in nature.

References

1. Michael R. S. Huang, Rolf Erni and Chuan-Pu Liu, Appl. Phys. Lett. 102, 061902 (2013)
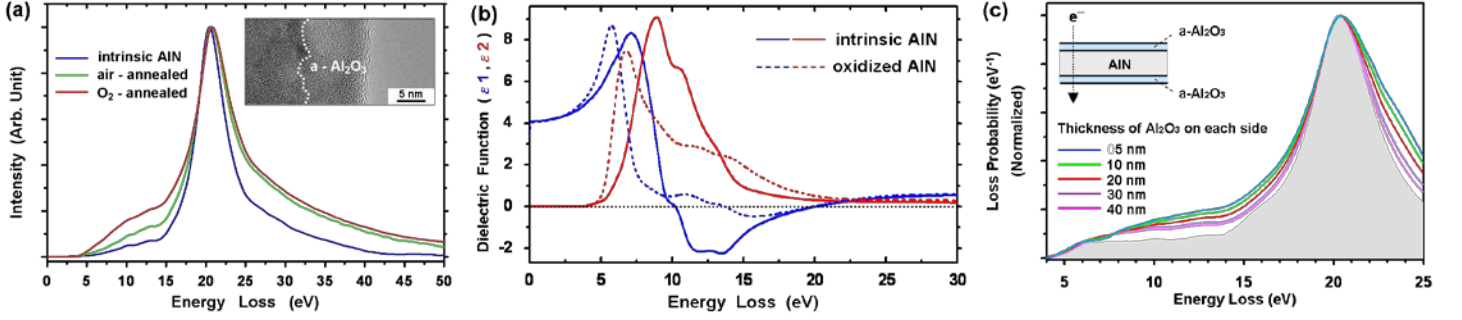
FIG. 1. (a) Comparison of the spectra from intrinsic AlN (blue), atmosphere (green) and O_2 (red) annealed samples, with zero-loss peaks and plural scattering deconvoluted. The inset shows a TEM bright-field image of a-Al_2O_3 overlayers at the edge of an oxidized nanoparticle. (b) Experimentally derived complex DFs ($\varepsilon = \varepsilon_1 + i\ \varepsilon_2$) of intrinsic (solid line) and oxidized (dashed line) AlN. (c) (a) Simulated low-loss spectra of a 60-nm bulk AlN slab with various thicknesses of a-Al_2O_3 overlayer. The schematic representation of the multilayer model utilized is also shown in the inset.

TRANSMISSION ELECTRON MICROSCOPY ANALYSES FOR THIN FILMS GROWN BY ATOMIC LAYER DEPOSITION

CHAO, Shih-Chun (趙士鈞), YU, Chia-Hao (余家濠), WEN, Cheng-Yen (溫政彥)

Department of Materials Science and Engineering, National Taiwan University, Taipei, Taiwan

Atomic layer deposition (ALD) is a proven way for conformal growth of uniform thin films. Using this technique, aluminum oxide (Al_2O_3) and titanium oxide (TiO_2) thin films can be fabricated for several potential applications. For example, Al_2O_3 is useful for gate oxide materials [1], and passivation layers in solar cells [2]; TiO_2 is beneficial in photocatalytic applications to harvest solar energy [3]. In this study, we use transmission electron microscopy (TEM) techniques to characterize the ALD grown Al_2O_3 and TiO_2 thin films.

For applications of TiO_2 thin films in photocatalytic reactions, the interfacial structure plays an important role. In the ALD growth of TiO_2, titanium isopropoxide (TTIP) and H_2O are used as precursors to deposit TiO_2 thin films on Si substrates at $250℃$. The plan-view and cross-sectional TEM images (Figure 1(a-b)) suggest that uniform polycrystalline TiO_2 thin films are deposited on Si substrates. The electron diffraction analysis (Figure 2) indicates that the TiO_2 thin films are the anatase phase. The cross-sectional scanning TEM (STEM) image (Figure 3) shows that there is an amorphous SiO_2 layer between the TiO_2 layer and the Si substrates, which may play an important role in the efficiency of the photocatalytic reactions.

For the growth of Al_2O_3 thin films, tri-methyl-aluminum (TMA) and H_2O are used as the precursors. The STEM analysis shows that the Al_2O_3 thin films are very uniform (Figure 4(a-b)). The sensitivity of the STEM contrast on atomic weight differentiates the amorphous Al_2O_3 thin films and the amorphous native SiO_2 layer. To further demonstrate the conformity of the ALD process for the growth of oxide material on complex nanostructures, Al_2O_3 dielectric layers were grown on the surface of high aspect-ratio silver nanowires. STEM energy dispersive spectroscopy (STEM-EDS) mapping results (Figure 5(a-f)) show uniform Al_2O_3 thin films on the surfaces of Ag nanowires. It can therefore be potentially applied to surrounding gate oxide layer in 3D electronics to increase the capacitance of metal-oxide-semiconductor devices.

References

1. D.C. Gilmer, R. Hegde, R. Cotton, R. Garcia, V. Dhandapani, D. Triyoso, D. Roan, A. Franke, R. Rai, L. Prabhu, C. Hobbs, J.M. Grant, L. La, S. Samavedam, B. Taylor, H. Tseng, P. Tobin, *Appl. Phys. Lett.*, 81 (2002)1288-1290.
2. G. Dingemans, E. Kessels, *J. Vac. Sci. Technol. A*, 30 (2012)040802.

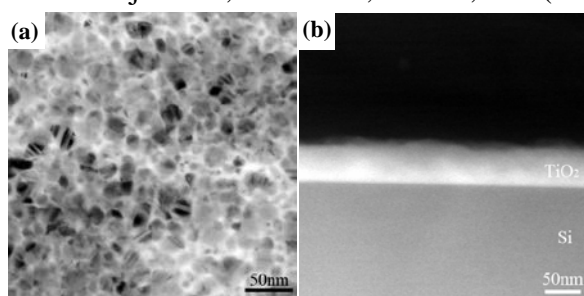3. A. Fujishima, K. Honda, *Nature*, 238 (1972)37-38.

Figure1. (a) Plan-view TEM image and (b) Cross-sectional HAADF-STEM image of the TiO_2 film grown by the atomic layer deposition (ALD) method on Si (111) substrates at 250°C.
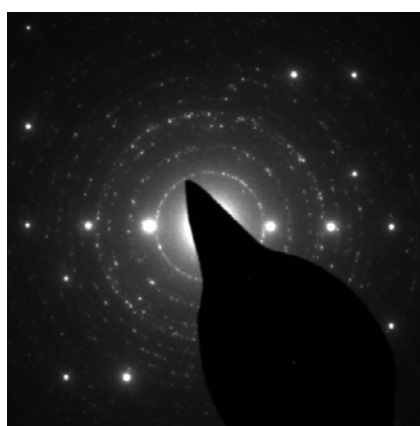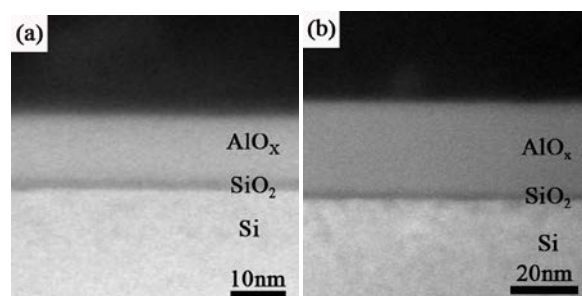

Figure 4. Cross-sectional HAADF-STEM images of ALD Al_2O_3 films after the growth of (a) 100 cycles and (b) 200 cycles.
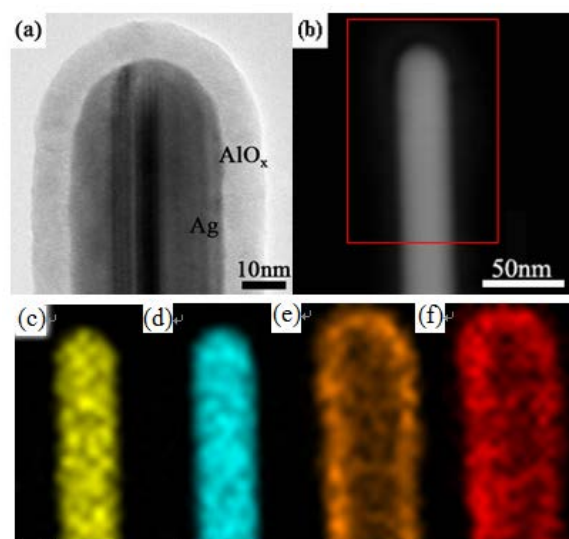

Figure 2. Selected-area diffraction pattern of the ALD TiO_2 film grown at 250 °C.

Figure 5. (a) TEM and (b) STEM images of the Al_2O_3 coated Ag nanowire.(c-f) EDS composition mapping results of the area labeled in (b), using Ag K-line, Ag L-line, O K-line, Al K-line respectively.

Figure 3. Cross-sectional HAADF-STEM image of ALD TiO2 film grown on Si (100) substrate.

KINETICS OF SILICIDE FORMATION IN SI NANOWIRES

CHOU, Yi-Chia(周苡嘉),[1] TU, King-Ning(杜經寧)[2]

[1]Department of Electrophysics, National Chiao-Tung University, Hsinchu, Taiwan
[2]Department of Materials Science and Engineering, University of California Los Angeles, Los Angeles, USA

Recent advances in nanotechnology have offered hope of extending Moore's law of large scale integration of semiconductor device circuits to nanodevices. Nanostructures based on Si and silicides will play an important role in future computer technology. Transition metal silicide nanowires are considered strong candidates for circuit elements in one-dimensional nanodevices, with applications including ohmic contacts, Schottky barriers, gate electrodes and interconnects. I will present in-situ high resolution transmission electron microscopy of solid-state chemical reactions in such nanostructures. Silicidation reactions take place at the point contact between adjacent nanowires or nanoparticles, and high resolution imaging allows the reaction to be followed in real time as each layer of Si is transformed. It is possible to control the formation of the metal silicide accurately enough to fabricate nano-gap heterostructures, where silicide regions are separated by just a few atomic planes of Si. The atomic-level details of the growth process can also be examined directly, and I will show axial epitaxial stepwise growth of $CoSi_2$, $NiSi$, and $NiSi_2$ in silicon nanowires. This growth process is unique, in that each atomic plane of silicide nucleates at the center of the nanowire cross-section in a homogeneous nucleation event that had been theoretically predicted but not observed previously. I will finally discuss the potential applications of these new nanostructures in future nanodevices.

References
1. Y. C. Chou, W. W. Wu, C. Y. Li, C. Y. Liu, L. J. Chen, K. N. Tu, *J. Phys. Chem. C*, 115 (2011) 397.
2. Y. C. Chou, W. W. Wu, L. J. Chen, K. N. Tu, *Nano Lett.*, 9 (2009) 2337.
3. Y. C. Chou, K. N. Tu, Chapter 5 in "One-Dimensional Nanostructures: Principles and Applications" John Wiley & Sons, Inc., Hoboken, New Jersey, U.S.A., 2013.
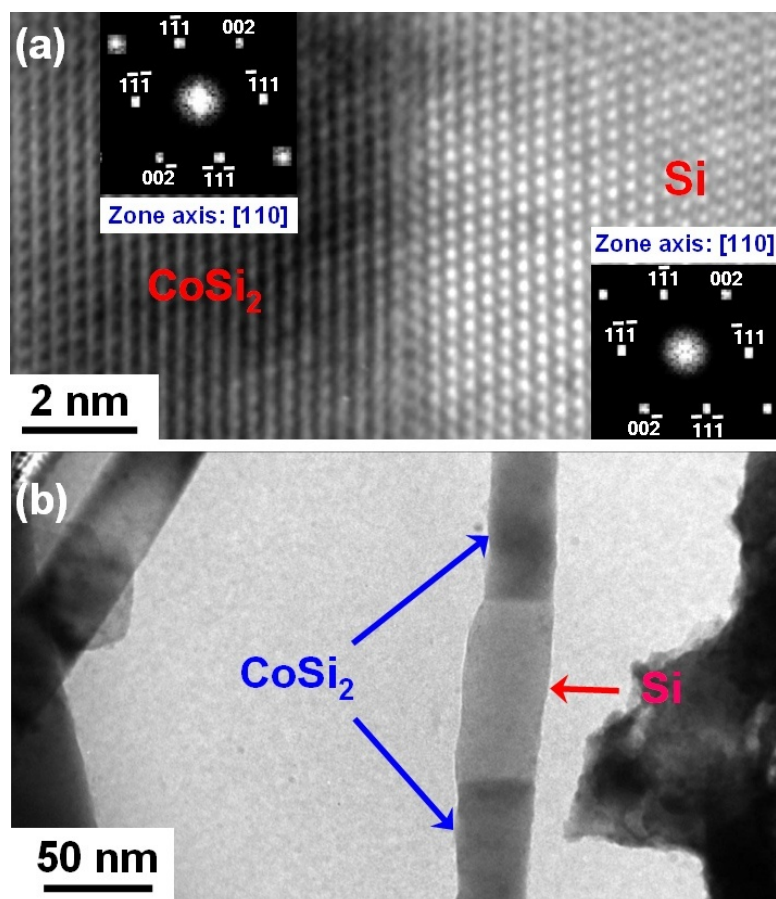
Figure 1. (a) High-resolution TEM image of CoSi$_2$–Si interface. The insets in panel a are the fast Fourier transform pattern confirming the [1 1 0] Si zone axis and the [1 1 0] CoSi$_2$ zone axis, respectively. {0 0 2} spots in the Si pattern are from double diffraction. (b) A TEM image of nanoheterostructure of CoSi$_2$/Si/CoSi$_2$ form within a Si nanowire.
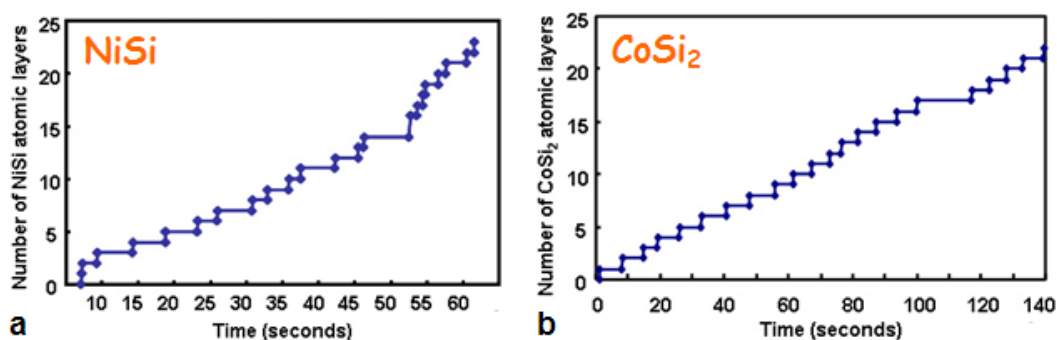

Figure 2. (a and b) The stair-type growth curves showing nucleation and growth periods for NiSi and CoSi$_2$, respectively.

DIRECT OPTICAL CHARACTERIZATIONS FOR GROWTH BEHAVIOR OF GRAPHENE ON COPPER BY CHEMICAL VAPOR DEPOSITION

CHANG, Ren-Jie(張仁頡), TSAI, Yun-Yi(蔡昀嶧), and WEN, Cheng-Yen(溫政彥)

Department of Materials Science and Engineering, National Taiwan University, Taipei, Taiwan

Graphene is a two-dimensional hexagonal lattice structure composed of carbon atoms. It has drawn significant attentions due to its distinctive physical properties. There are several methods for graphene fabrication [1], including mechanical exfoliation, epitaxial growth of graphene on silicon carbide substrate, and the chemical vapor deposition process. Among these methods, the chemical vapor deposition (CVD) method offers a simple and controllable approach to grow graphene. Using the CVD method, the number of stacking graphene layers can be controlled by adjusting the flow ratios of gas reactants. The area of the graphene sheet is the area of the substrate, thus, making large area graphene sheet is very straightforward. However, the drawback of this method is that the graphene layer contains defects, such as the domain boundaries [2], which degrade the carrier transport properties.

In order to fabricate high-quality large-area graphene layers for future applications in electronics and flat panel displays, we study the growth mechanism of graphene on Cu substrates in the chemical vapor deposition process. In this study, optical microscopy is a convenient tool for studying the growth mechanism of graphene. To further enhance the contrast for seeing the morphology of graphene layers on the Cu substrates, annealing the as-grown graphene sample at 200°C is an essential step. Because graphene is an excellent passivation, Cu substrate underneath graphene islands present different contrast from those oxidized [3]. The growth of graphene on the substrates is therefore observable ex-situ under an optical microscope. Experimental observations show nucleation and coalescence of graphene (Fig. 1(a-d)). It is noted that high temperature growth (Fig. 2(a-f)) or a high H_2/CH_4 ratio (Fig. 3(a-h)) during the growth are beneficial for the fabrication of graphene. Moreover, the facets of the graphene islands inside different Cu grains are aligned in different directions, implying a strong effect of the orientation of the Cu grains on the growth of graphene.

References
1. W. Choi,; I. Lahiri,; R. Seelaboyina,; Y. S. Kang, *Crit. Rev. Solid State Mater. Sci.* 35 (2010) 52.
2. H. Wang,; G. Wang,; P. Bao,; S. Yang,; W. Zhu,; X. Xie,; W.-J. Zhang, *J. Am. Chem. Soc.* 134 (2012) 3627.
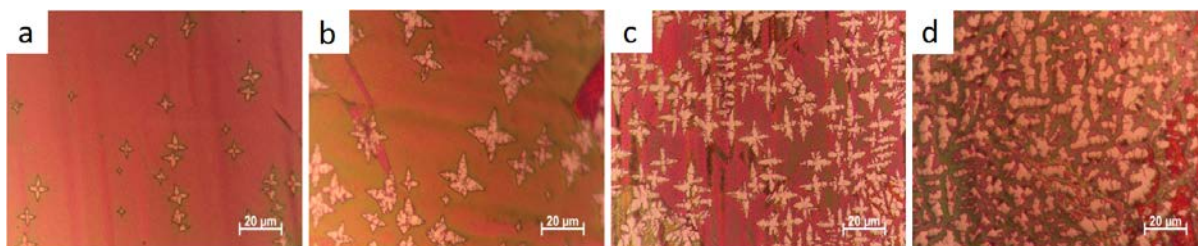3. C. Jia,; J. Jiang,; L. Gan,; X. Guo, *Sci. Rep.* 2 (2012) 707.

Figure 1. Optical microscopy images of graphene growth in the early stage. The growth is at 1000°C with 20 sccm hydrogen and 2 sccm methane flow for (a) 1.5 min, (b) 2 min, (c) 4 min, and (d) 10 min.
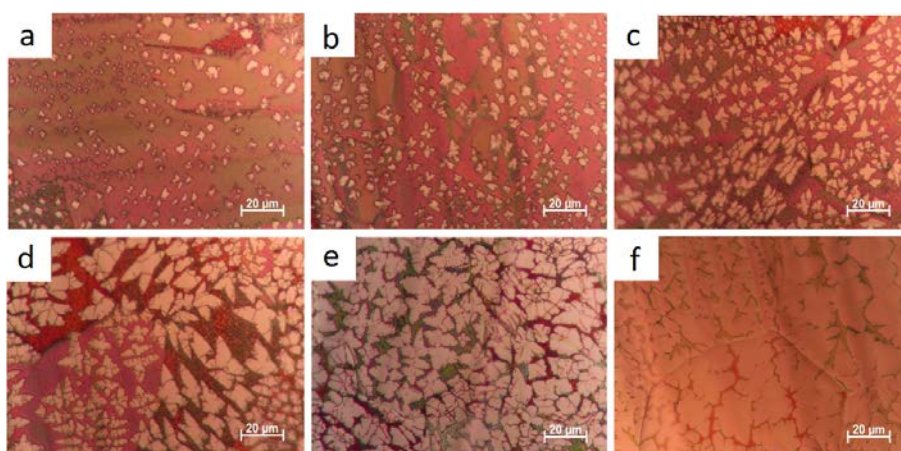

Figure 2. Optical microscopy images showing the temperature effects on the nucleation density of graphene with 40 sccm hydrogen and 2 sccm methane flow for 2 min at (a) 955°C, (b) 970°C, (c) 985°C, (d) 1000°C, (e) 1015°C, and (f) 1030°C.
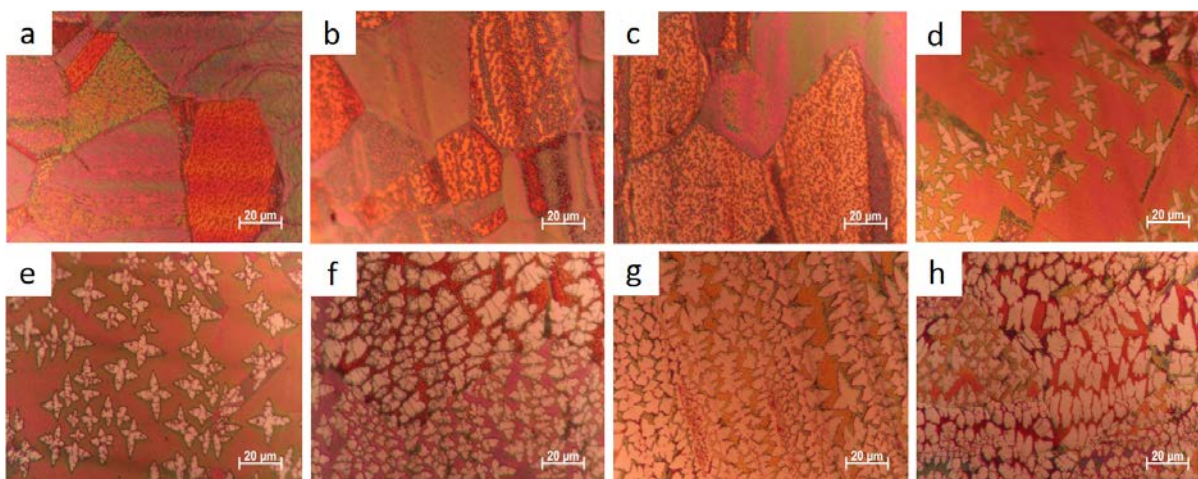

Figure 3. Optical microscopy images showing the hydrogen effects of graphene growth at 1000°C for 2 min with 2 sccm methane flow and the hydrogen flow of (a-h) 0, 5, 10, 15, 20, 40, 60, and 80 sccm, respectively.

IN-SITU TEM STUDY OF THE LITHIATION BEHAVIOR OF A SINGLE SN DOPED ZNO NANOWIRE

Lai, Ming-Wei（賴明偉）, Lo, Shen-Chuan（羅聖全）, Chen, Yu-Hsiang（陳育祥）, and Tsai, Cheng-Ting（蔡承廷）

Material and Chemical Research Laboratories, Industrial Technology Research Institute, Hsinchu, Taiwan

As the advantages of high energy capacity, no memory effect, light weight, and long lifetime, Li-ion batteries have already became the most adopted power source for portable devices. Recently, in-situ transmission electron microscope (TEM) study was adopted to investigate the lithiation behaviors of some anode materials of Li-ion batteries [1-5]. This technique effectively helps to understand the degeneration mechanisms of the electrodes during the battery cycling.

In present study, the assembly of a modal Li-ion nanobattery, constituted by a single Sn doped ZnO (Sn:ZnO) nanowire (NW) as the anode and a native Li_2O covered Li piece as the solid-state electrolyte covered cathode, was realized on a homemade piezo-positioner equipped TEM holder. With applying a -25V charging voltage on this modal nanobattery, a real-time TEM observation of the Sn:ZnO NW lithiation was carried out. Figure 1 depicts the experimental setup of the modal nanobattery.

The appearance evolution of the Sn:ZnO NW during lithiation is shown in figure 2. After intercalation with Li^+ ions, the Sn:ZnO NW became slightly twisted and exhibited a ~40% diametric expansion. The reaction front, in between the lithiated and the pristine region, is noticed showing a taper-like shape, which implies that the lithiation of the Sn:ZnO NW is an outside-toward-inside process.

Figure 3 shows the high magnification TEM images and the selective area electron diffraction (SAED) patterns corresponding to the pristine region, the reaction front, and the lithiated region of the Sn:ZnO NW, respectively. It is found that lithiation amorphizes the nanoscaled anode, and the equations can used to interpret the possibly happened electrochemical reactions here are [3, 5]:

$$(2 + x)e^- + ZnO + (2 + x)Li^+ \rightarrow Li_2O + Li_xZn \quad (1)$$
$$(4 + x)e^- + SnO_2 + (4 + x)Li^+ \rightarrow 2Li_2O + Li_xSn \quad (2)$$
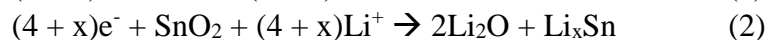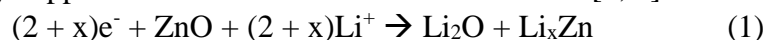
There are many fine cracks scattering inside the lithiated region. According to the discussion of the similar find in studying the lithiation mechanism of pure ZnO NWs [5], these cracks are believed to be originated from the surface lithiation of the Sn:ZnO NW. They then facilitate the diffusion of Li^+ ions toward the inner part of the NW and finally become the amorphous/amorphous interfaces.

References
1. Xiao Hua Liu et al., Nano Lett., 11 (2011) 3312.
2. Xiao Hua Liu et al., Energy Environ. Sci., 4 (2011) 3844.
3. Jian Yu Huang, et al., Science, 330 (2010) 1515
4. Li Zhong, et al., Phys. Rev. Lett., 106 (2011) 248302
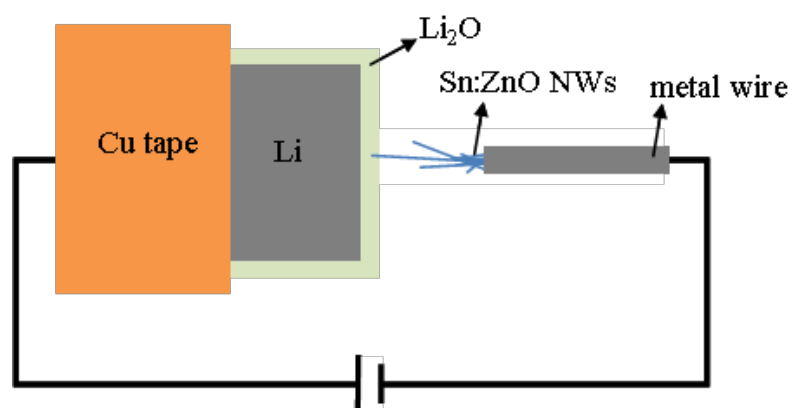5. Akihiro Kushima, et al.,Nano Lett., 11 (2011) 4535

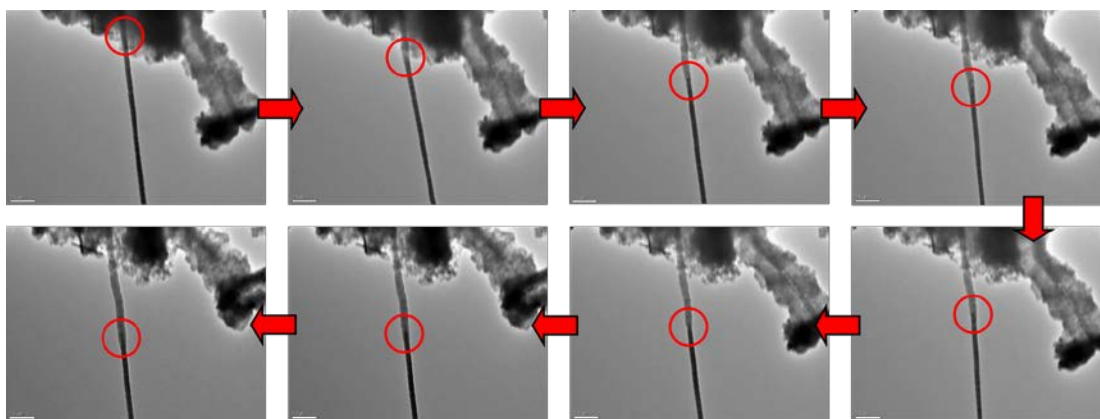Fig. 1 The experimental setup of the modal nanobattery.

Fig. 2 The appearance evolution of the Sn:ZnO NW during lithiation. The red circles indicate the positional progression of the reaction front. (scale bar = 500 nm)
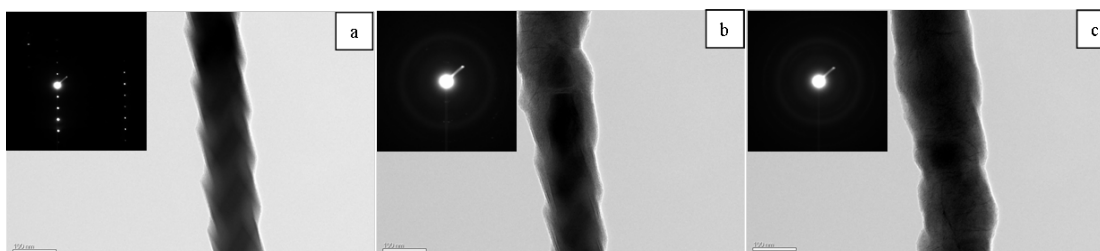

Fig. 3 High magnification TEM image and SAED patterns corresponding to (a) the pristine region, (b) the reaction front, and (c) the lithiated region of the Sn:ZnO NW. (scale bar = 100 nm)

CHARGE DENSITY WAVE STUDY IN DY$_5$IR$_4$SI$_{10}$

M. H. Lee[1,2] (李明浩), C. H. Chen[1,2,3,] (陳正弦), M.-W. Chu[2] (朱明文), H. D. Yang[4] (楊弘敦)

1. Department of Physics, National Taiwan University, Taipei, Taiwan

2. Center for Condensed Matter Sciences, National Taiwan University, Taipei, Taiwan

3. Institute of Atomic and Molecular Sciences, Academia Sinica, Taipei, Taiwan

4. Department of Physics, National Sun Yat-sen University, Kaohsiung, Taiwan

The tetragonal rare-earth transition-metal silicide system, $R_5T_4Si_{10}$, where R is Dy, Ho, Er, Tm, and Lu, and T = Ir and Rh, with seemingly three-dimensional crystallographic structure, has been shown to exhibit fascinating charge density wave (CDW) phase transitions, a phenomenon found largely in low-dimensional systems. In this study we report the investigations of CDW in Dy$_5$Ir$_4$Si$_{10}$ at different temperatures using transmission electron microscopy (TEM) techniques including electron diffraction and dark-field imaging.

Superlattice diffraction spots along c-axis were observed in the electron diffraction pattern when the sample was cooled below the CDW transition temperature (T$_{CDW}$ ~ 200K), indicating the presence of incommensurate CDW state with the modulation wave vector of $\vec{q} = (0,0,\pm 0.25 \pm \delta)$. CDW become commensurate with further cooling below 160K. Configurations of CDW dislocations convincingly show that the CDW phase transition is accompanied by a concomitant cell-doubling crystallographic structural phase transition. Furthermore, symmetry breakdown along c-axis observed by convergent beam electron diffraction (CBED) gives rise to two different type of CDW domains. Detailed characteristics of this unusual behavior will also be discussed.
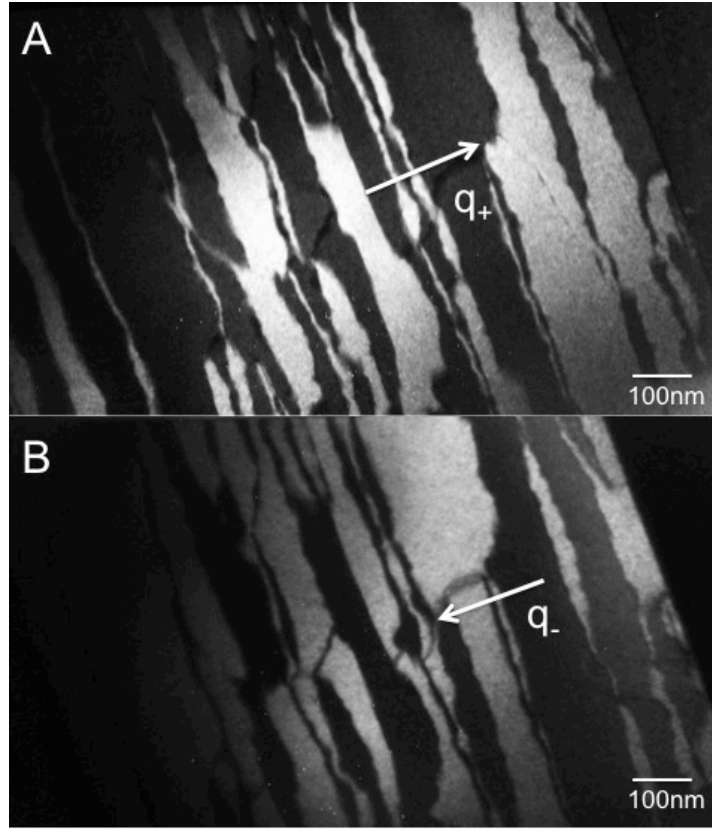
The fig (A) and (B) are dark-field images obtained from $\vec{q}_{+} = (0,0,0.25)$ and $\vec{q}_{-} = (0,0,-0.25)$ superlattice spots in commensurate state, respectively. It is clear that modulation wave vectors $\vec{q}_{+}$ and $\vec{q}_{-}$ actually come from different domains. No chemical inhomogeneity between these two regions by chemical analysis electron nano-probe. The domain contrast results from breakdown of the crystallography symmetry along the c-axis, which is also the CDW modulation wave vector.

ELECTRONICALLY PHASE-SEPARATED CHARGE DENSITY WAVES IN LU$_2$IR$_3$SI$_5$

<u>M. H. Lee</u>[1,2] (李明浩), C. H. Chen[1,2,3,] (陳正弦), M.-W. Chu[2] (朱明文), C. S. Lue[4] (呂欽山), Y. K. Kuo[5] (郭永綱)

1. Department of Physics, National Taiwan University, Taipei, Taiwan

2. Center for Condensed Matter Sciences, National Taiwan University, Taipei, Taiwan

3. Institute of Atomic and Molecular Sciences, Academia Sinica, Taipei, Taiwan

4. Department of Physics, National Cheng Kung University, Tainan, Taiwan

5. Department of Physics, National Dong Hua University, Hualien, Taiwan

We report the investigation of charge density wave (CDW) in Lu$_2$Ir$_3$Si$_5$ by electron diffraction and dark-field imaging using superlattice diffraction spots. The CDW state is confirmed by the presence of superlattice reflections. Most interestingly, the CDW state at low temperatures is found to be electronically phase-separated with the coexistence of CDW domains and low-temperature normal phase domains. Upon change of temperatures, unlike other typical incommensurate CDW systems in which commensurability varies with temperatures, we find that commensurability remains unchanged in the present case and the predominant change is in the redistribution of the area ratio of the two coexisted phases, which is clearly revealed in the dark-field images obtained from the CDW superlattice reflections. The electronic phase separation in the CDW state of Lu$_2$Ir$_3$Si$_5$ is unprecedented in CDW systems, and its temperature dependence is also anomalous.
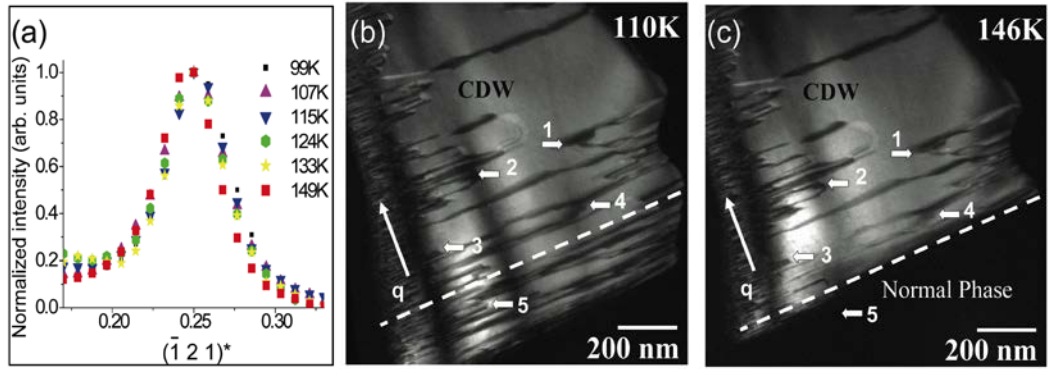
Fig.1 (a) Intensity profile of CDW superlattice reflections showing that the position and width remain largely unchanged as a function of temperature. (b) and (c) show the CDW domains feature recorded at 110 K and 146 K, respectively. With increasing temperature, the domain boundary (dashed line) separating the CDW phase (area with brighter contrast) and the low temperature normal phase (area with dark contrast) moves in a direction along the CDW modulation wave vector such that the area of non-CDW phase grows at the expense of CDW domain. It is noted that detailed configurations of discommensurations in the CDW domain, marked 1 thorugh 5 for reference, remain unchanged with rising temperature.

第三十三屆顯微鏡學會年會研討會攝影比賽影像集

I-01	氧化鋅天堂鳥
	林芯儀
	國立成功大學材料工程學系
I-02	森林中嬉戲的憤怒鳥
	洪麗分
	台灣大學生態學暨演化生物學研究所
I-03	不速之客
	葉侑橋
	台灣大學園藝暨景觀研究所
I-04	冒險者們
	葉侑橋
	台灣大學園藝暨景觀研究所
I-05	進食的魯蛇
	黃柏銘
	台灣大學材料科學與工程學研究所
I-06	飛舞的蝴蝶
	陳伯宇
	台灣大學材料科學與工程學研究所
I-07	河流
	張雅齡
	台灣大學材料科學與工程學研究所
I-08	小黃瓜的素描
	包尚弘
	國立中興大學生命科學系
I-09	雙晶
	張雅齡
	台灣大學材料科學與工程學系
I-10	奈米梯田
	黃彥霖
	中興大學材料所
I-11	電化學結晶形成的柱狀晶組織含有高密度雙晶
	陳黼澤、林招松
	台灣大學材料科學與工程學系
I-12	硬質陶瓷微粒均勻彌散強化的鎳磷-碳化矽複合鍍層
	陳黼澤、林招松
	台灣大學材料科學與工程學系

I-13	忍硅現身
	[1,2] 吳盈瑩
	[1] 國立台灣大學材料科學與工程學系暨研究所
	[2] 國立台灣科技大學材料科學與工程系
I-14	甜甜圈佐珍珠!
	[1,2] 吳盈瑩
	[1] 國立台灣大學材料科學與工程學系暨研究所
	[2] 國立台灣科技大學材料科學與工程系
I-15	火山湖上的倒影（Cu@Ag 核殼奈米顆粒之莫瑞條紋）
	[1] 蔡齊航 [2] 宋振銘 [3] 陳詩芸
	[1] 台灣科技大學應用科技研究所
	[2] 中興大學材料系
	[3] 台灣科技大學材料系
I-16	黃色小精靈
	陳運萱、許秋容
	國立中興大學生命科學系
I-17	孕
	吳業華、許秋容
	國立中興大學生命科學系
I-18	臺灣近海超級鯨魚大發生空照圖
	許秋容
	國立中興大學生命科學系
I-19	差排一條龍
	楊景明
	台灣大學材料科學與工程學系
I-20	剛柔並濟
	劉鑑緯、許秋容
	國立中興大學生命科學系
I-21	夏威夷比薩
	劉鑑緯、許秋容
	國立中興大學生命科學系
I-22	碳化物
	張雅齡
	台灣大學材料科學與工程學研究所
I-23	餓了嗎？來點 Cheese cake 吧！
	蔡昀嶧
	台灣大學材料科學與工程學研究所
I-24	複相組織鋼中薄膜狀殘餘奧氏體

	謝振家
	北京科技大學
I-25	**鈷磷合金高溫退火相變態微結構演變**
	[1,2]陳黼澤、[1]林招松、[2]潘永寧、[3]李春穎
	[1]臺灣大學材料科學與工程學系
	[2]臺灣大學機械工程學系
	[3]臺北科技大學機械工程系
I-26	**低熔點 SiO_2-Na_2O-Al_2O_3 玻璃陶瓷複合塗層微結構解析**
	陳黼澤、林招松
	臺灣大學材料科學與工程學系
I-27	**法國毛毛蟲的領巾**
	李莉姿、林壯宇
	中央研究院細胞與個體生物學研究所
I-28	**美人魚**
	蕭宇成
	臺灣大學應用物理研究所

作品名稱: 氧化鋅天堂鳥

作品內容
以化學氣相沉積法製備之奈米氧化鋅天堂鳥 SEM 圖。

作者姓名: 林芯儀	單位: 國立成功大學 材料工程學系
聯絡電話: 0983089034	E-Mail: limyee_88@hotmail.com
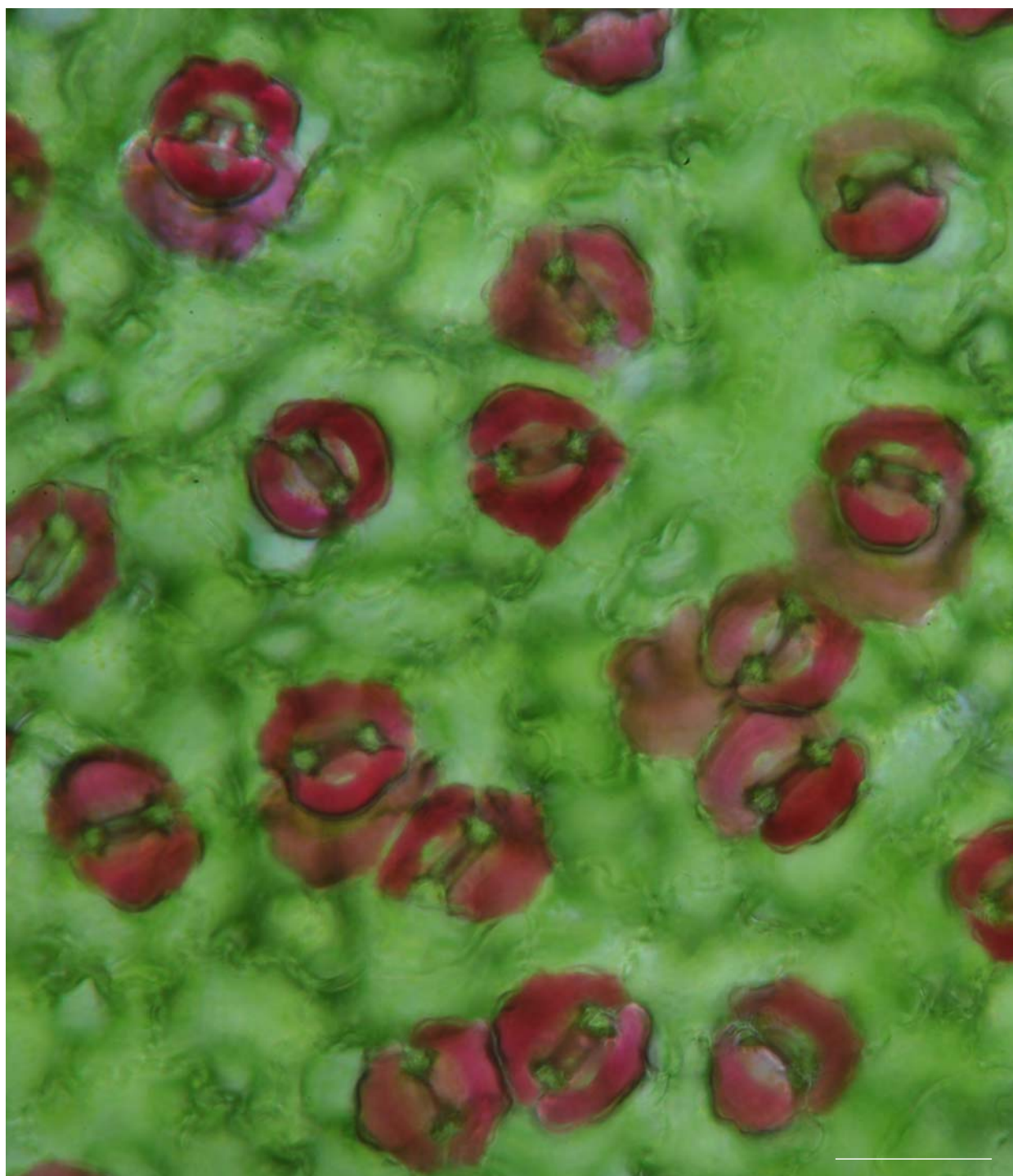
作品名稱：森林中嬉戲的憤怒鳥

作品內容

變葉木葉片未經處理的平表切片，在顯微鏡下觀察到的迷人氣孔複合體

Bar=50μm

作者姓名：洪麗分	單位：臺灣大學生態學與演化生物學研究所
聯絡電話：02-33662510	E-Mail：d97b44007@ntu.edu.tw

作品名稱　不速之客

作品內容

從遙遠的地方而來，陷入泥沼中而無法脫離的神祕載具。

Scale: 4μm 細葉山茶(*Camellia tenuifolia*)花粉

作者姓名　葉侑橋	單位　台灣大學園藝暨景觀研究所
聯絡電話　0937905047	E-Mail r01628103@ntu.edu.tw
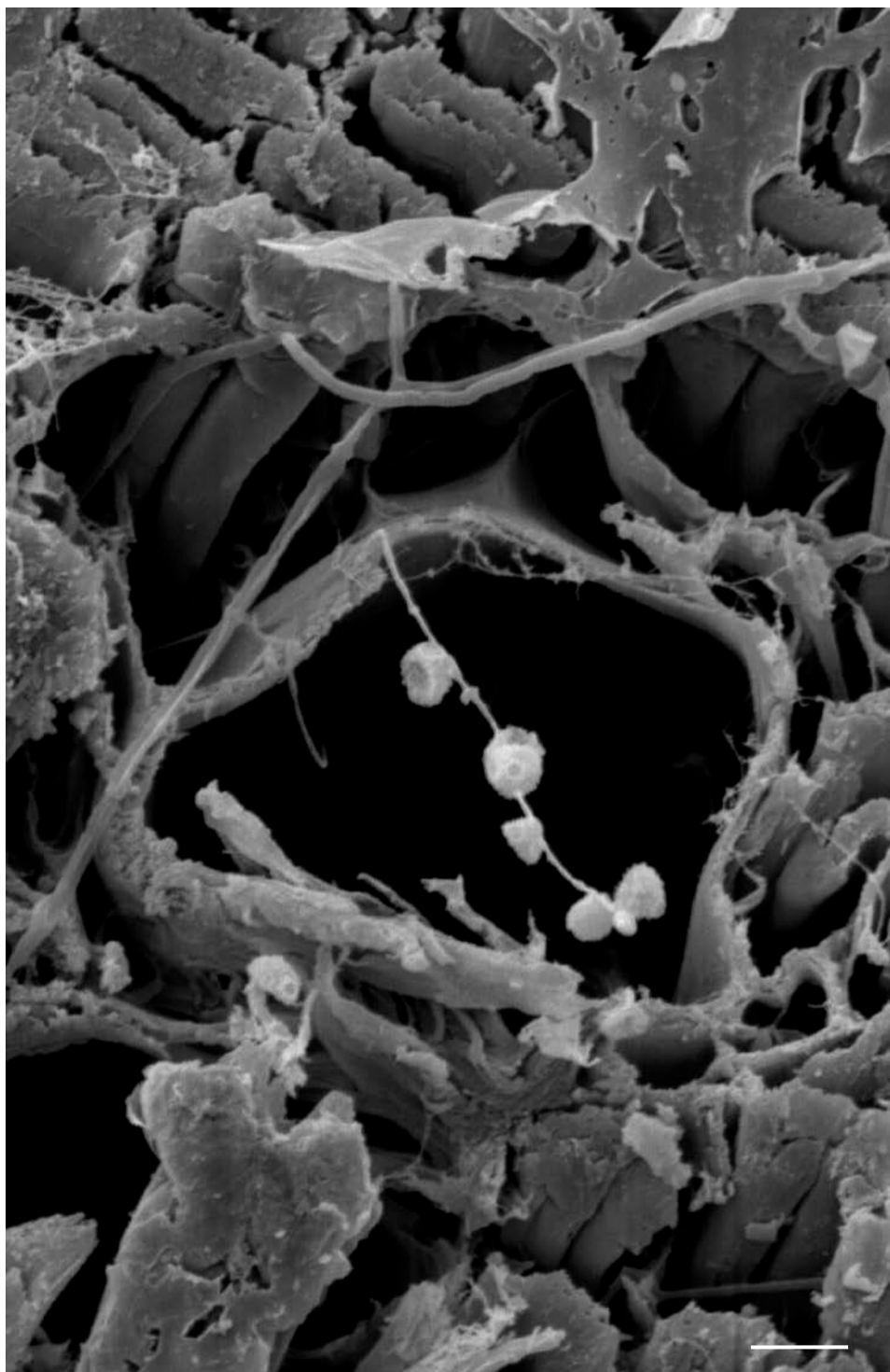
作品名稱　冒險者們

作品內容

五個社會新鮮人朝著未知的寂靜垂降。

Scale: 6.66μm (Stem of *Camellia sinensis*)

作者姓名 葉侑橋	單位 台灣大學園藝暨景觀研究所
聯絡電話 0937905047	E-Mail r01628103@ntu.edu.tw

SEI 15kV WD11mm SS50 x100 100μm
NTUMSE
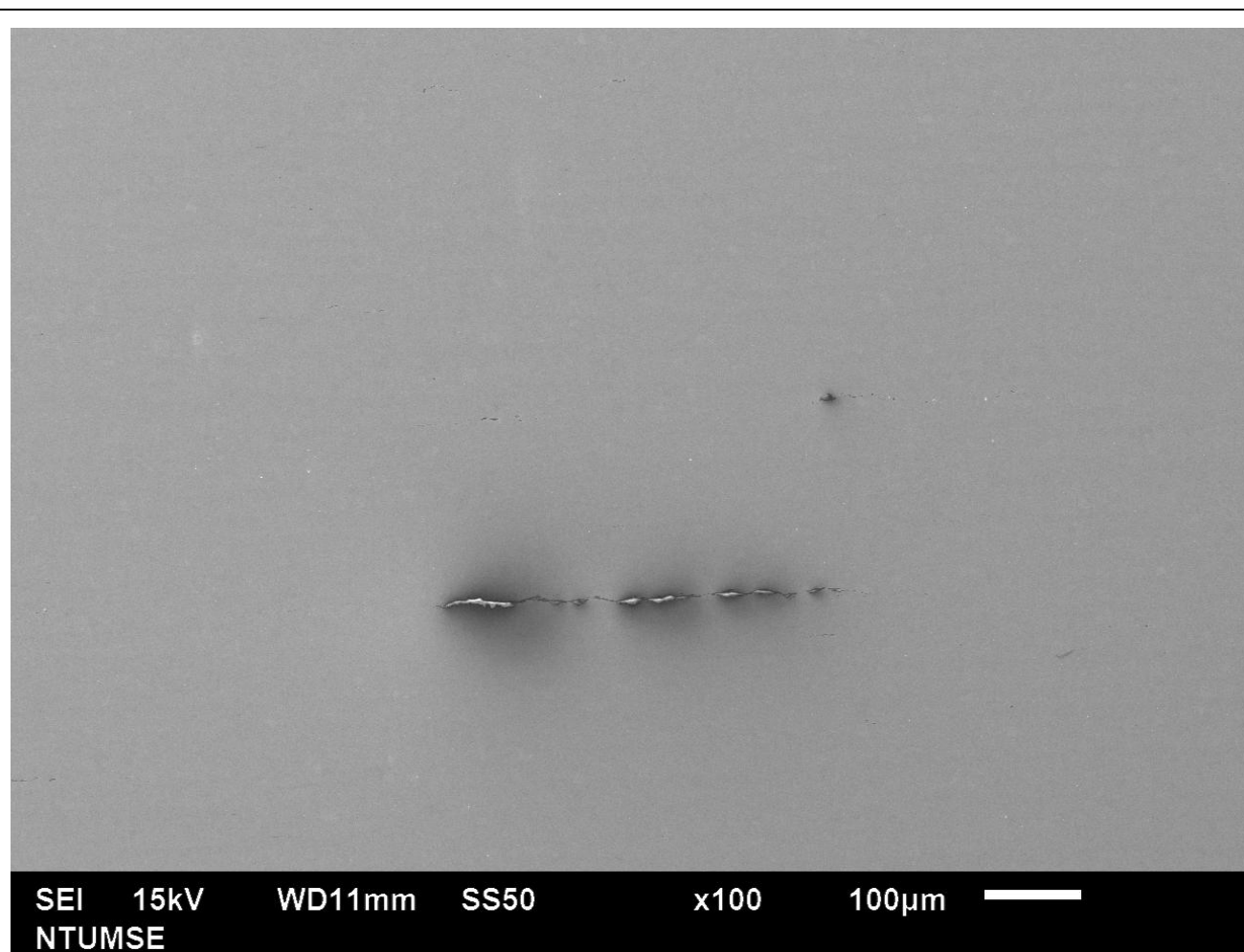
作品名稱	進食的魯蛇

作品內容

正在狼吞虎嚥的魯莽小蛇，未消化的食物使細長的身軀膨脹數倍。

作者姓名　黃柏銘	單位　台灣大學材料科學與工程學研究所
聯絡電話　02-3366-3748	E-Mail:d98527005@ntu.edu.tw

1 µm
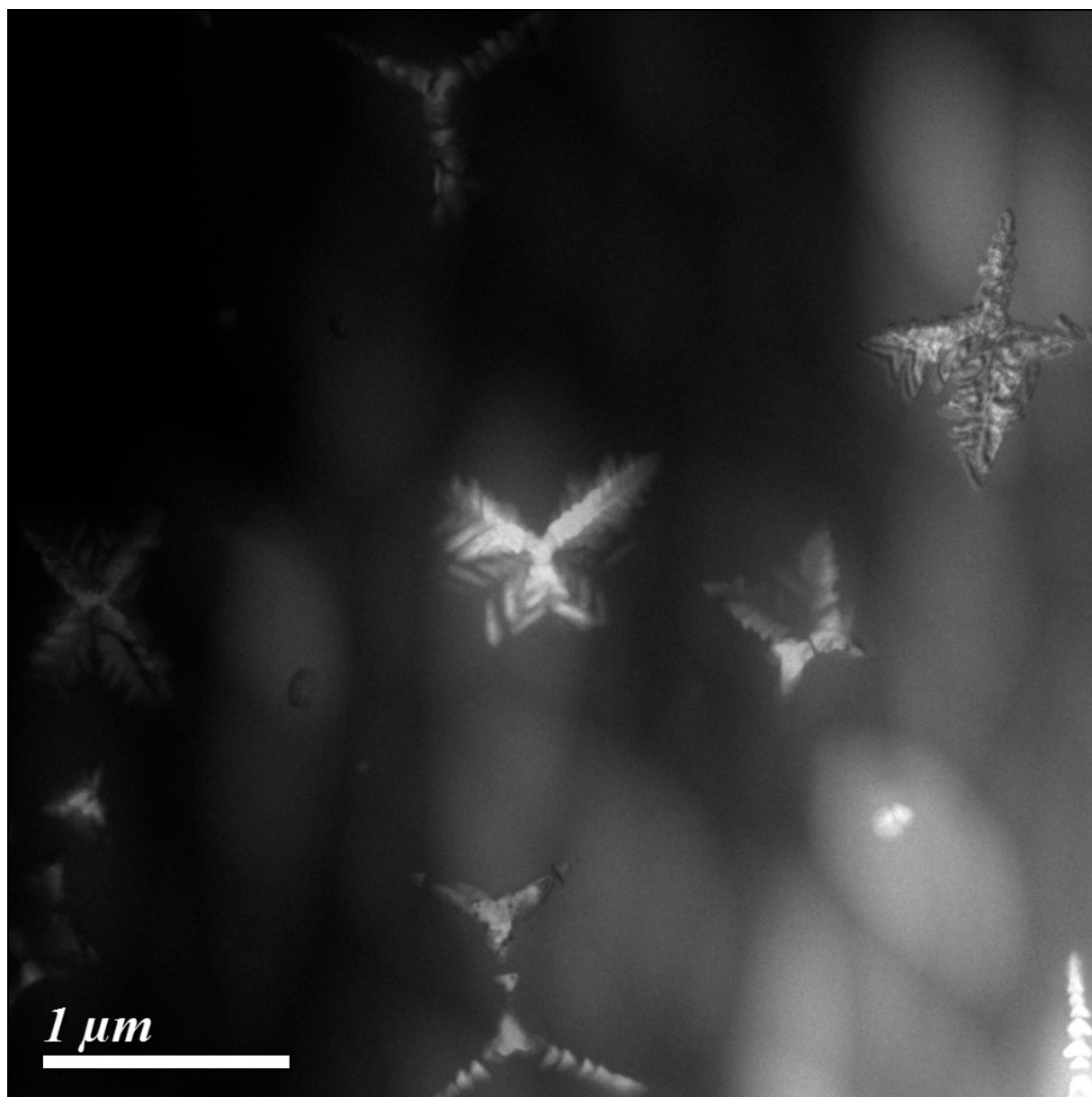
作品名稱　飛舞的蝴蝶

作品內容

鐵系非晶質薄帶經退火後產生之 α-Fe 樹狀晶

作者姓名　陳伯宇	單位　台灣大學材料科學與工程學研究所
聯絡電話　02-3366-1353	E-Mail　d00527002@ntu.edu.tw

100nm
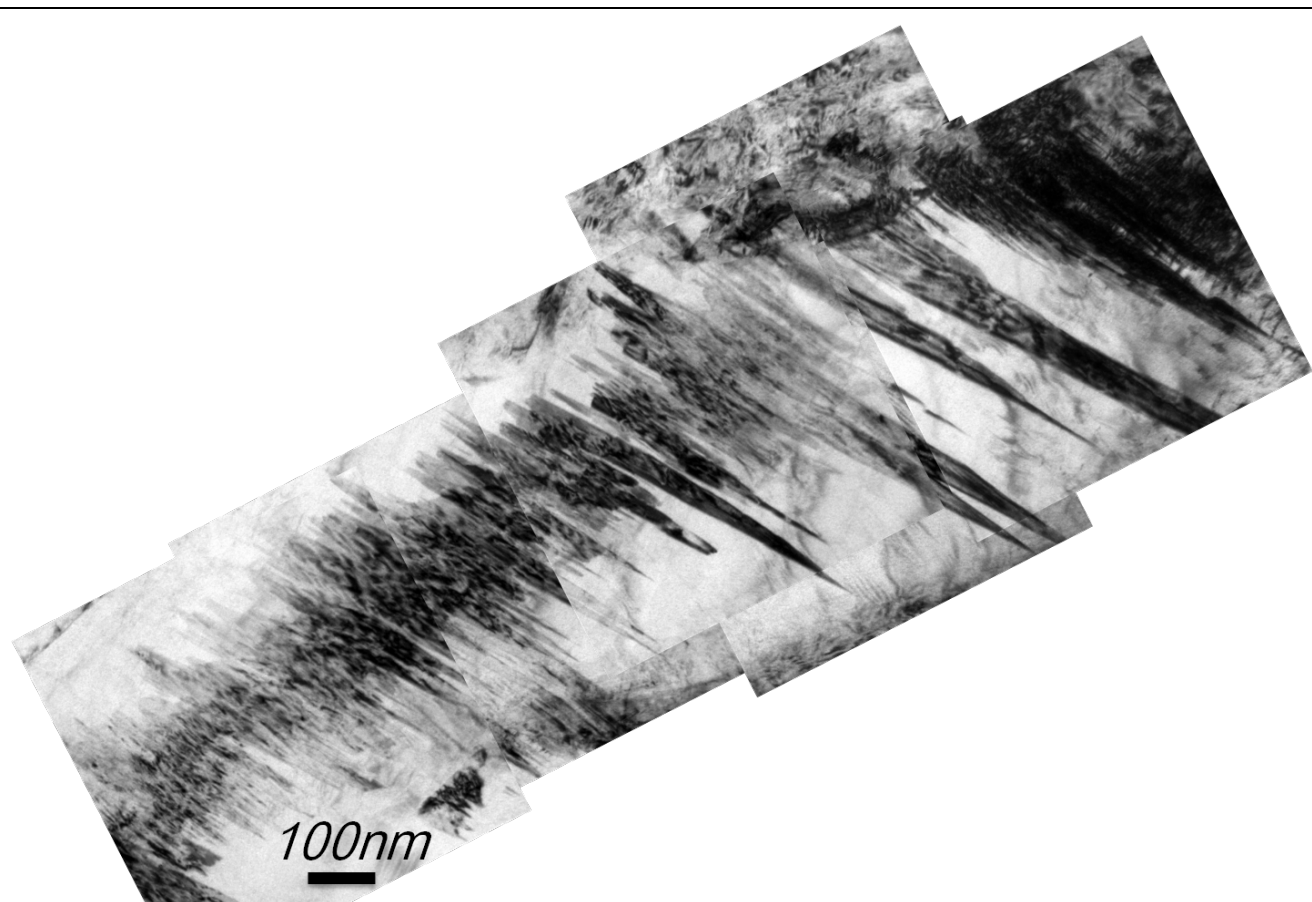
作品名稱：雙晶

作品內容： AISI 440C 中的顯微結構，有如新聞畫面中的地震儀，左右搖擺劃線紀錄地震的過程，原來微觀世界就預知大地震即將來臨!

作者姓名：張雅齡	單位：台灣大學材料科學與工程學研究所
聯絡電話：0933326371	E-Mail：d99527007@ntu.edu.tw

1 µm
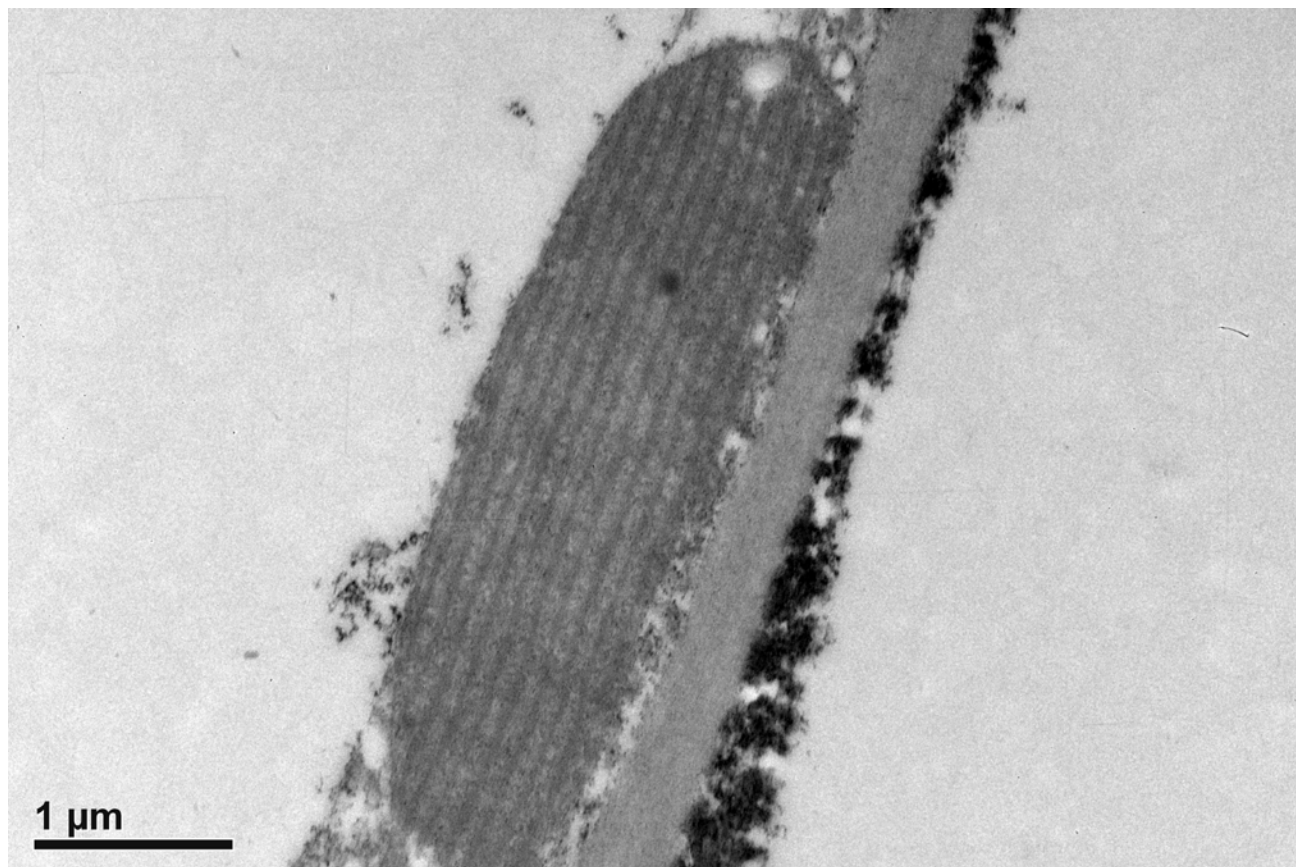
作品名稱	小黃瓜的素描

作品內容

乍看之下，還真以為是一條小黃瓜！其實，這是出現在秋海棠科 *Begonia edulis* 近軸面葉表皮細胞內的特殊葉綠體。

作者姓名　包尚弘	單位　國立中興大學　生命科學系
聯絡電話　0938380892	E-Mail Louiscat9016@gmail.com

100nm
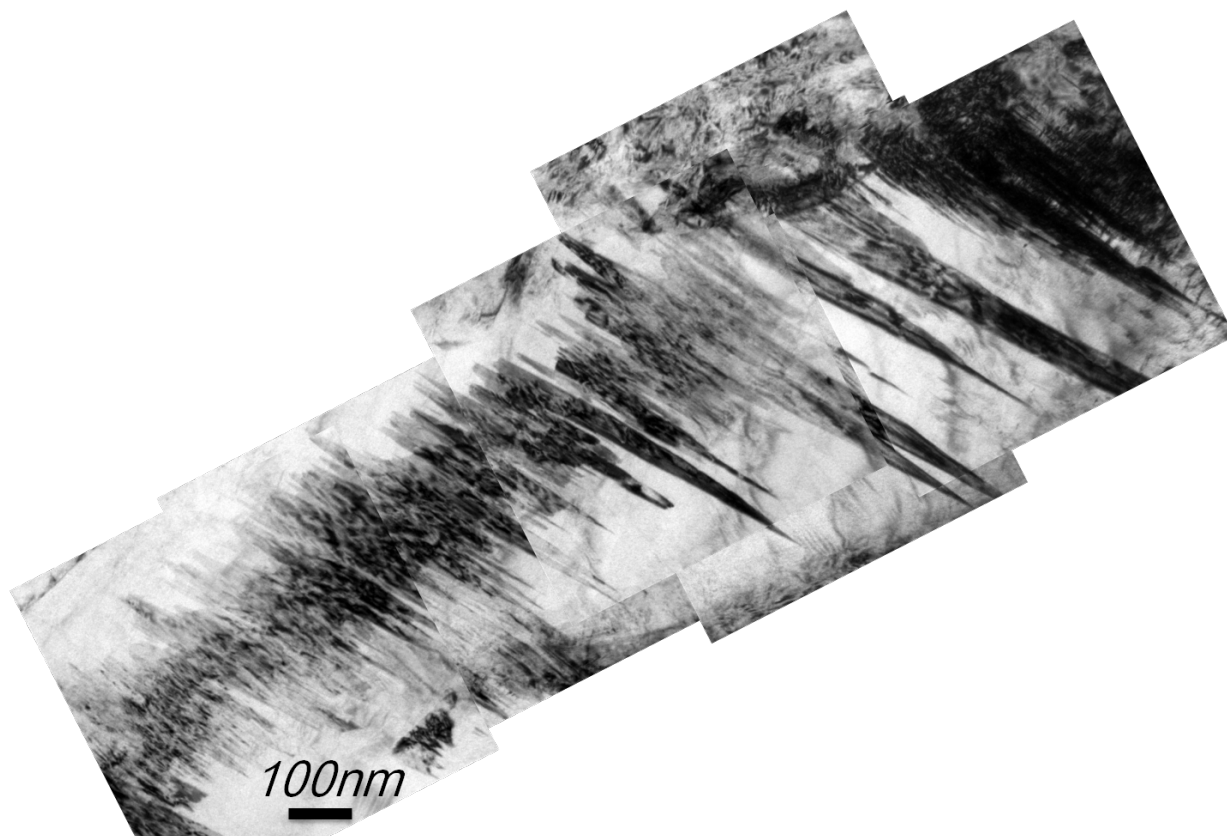
作品名稱：雙晶

作品內容：像河流一般，河流分支。

作者姓名：張雅齡	單位：台灣大學材料科學與工程學系
聯絡電話：0933326371	E-Mail：d99527007@ntu.edu.tw

NCHU02　　　　SEI　　3.0kV　X100,000　WD 3.0mm　100nm
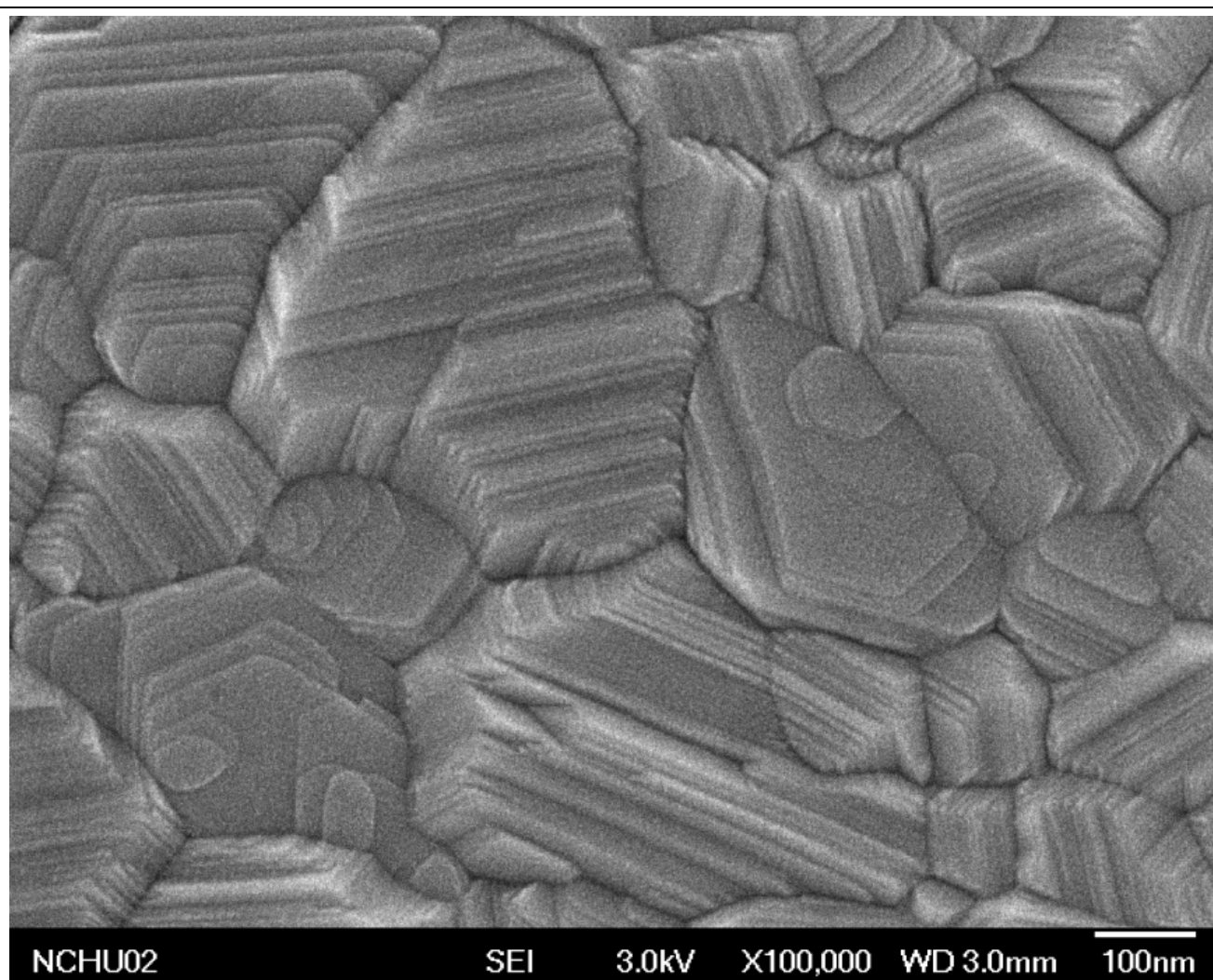
作品名稱　奈米梯田

作品內容
富含疊差及雙晶之面缺陷尖晶石結構的鈦酸鋅薄膜，階梯落差約為 2.8 nm。

作者姓名　黃彥霖	單位　中興大學材料所
聯絡電話 0910733264	E-Mail d9866013@mail.nchu.edu.tw
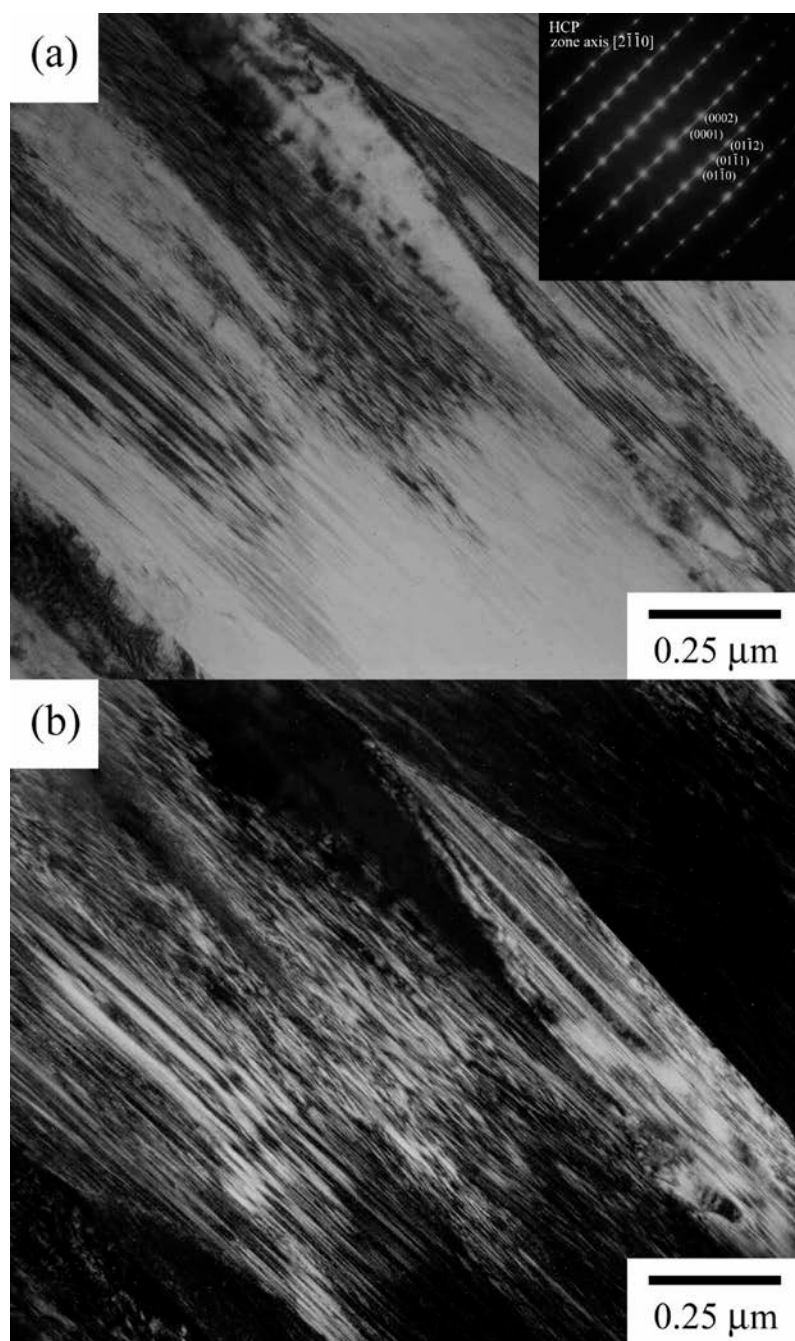
圖說明：直流電鍍鈷磷合金微結構解析：(a)柱狀晶明視野影像，(b)柱狀晶暗視野影像。

作品名稱：電化學結晶形成的柱狀晶組織含有高密度雙晶	

作品內容

直流電鍍鈷磷合金微結構是沿著電場方向成長的 HCP 柱狀晶組織，由於磷元素固溶於鈷晶粒將導致柱狀晶組織含有高密度雙晶的電化學結晶缺陷。

作者姓名：陳齁澤、林招松	單位：臺灣大學 材料科學與工程學系
聯絡電話：(02)33662678；0910797382	E-Mail：fjuge3318@yahoo.com.tw
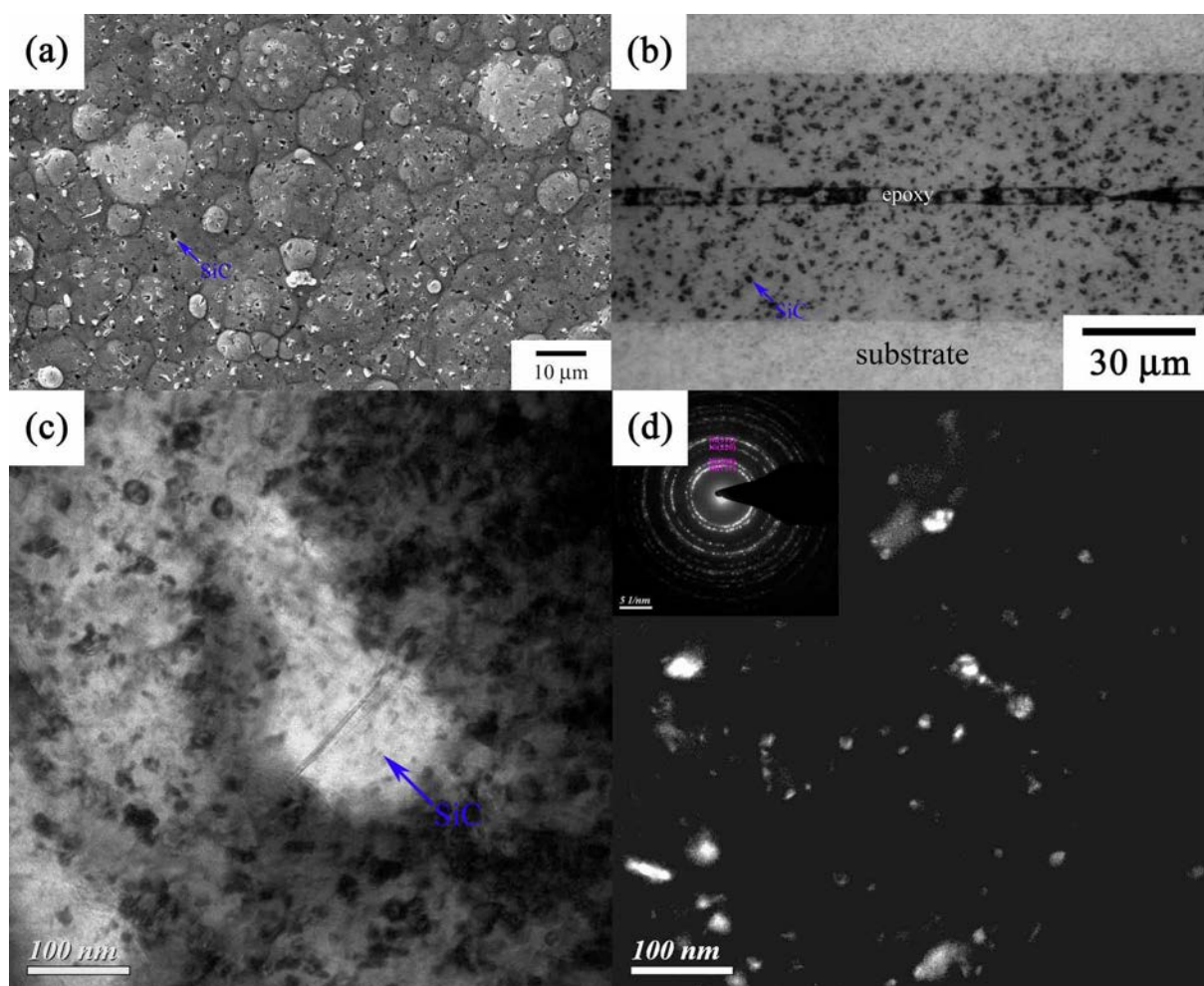
圖說明：鎳磷-碳化矽複合鍍層微結構解析：(a) SEM 表面形貌觀察，(b)橫截面 OM 金相，(c) TEM 明視野影像，(d) TEM 暗視野影像與鎳磷基地繞射分析。

作品名稱：硬質陶瓷微粒均勻彌散強化的鎳磷-碳化矽複合鍍層	
作品內容	
複合電鍍製程使次微米級碳化矽硬質陶瓷微粒均勻共鍍與散佈強化鎳磷鍍層，提升複合鍍層硬度和抗腐蝕磨耗效益。	
作者姓名：陳鼎澤、林招松	單位：臺灣大學 材料科學與工程學系
聯絡電話：(02)33662678；0910797382	E-Mail：fjuge3318@yahoo.com.tw
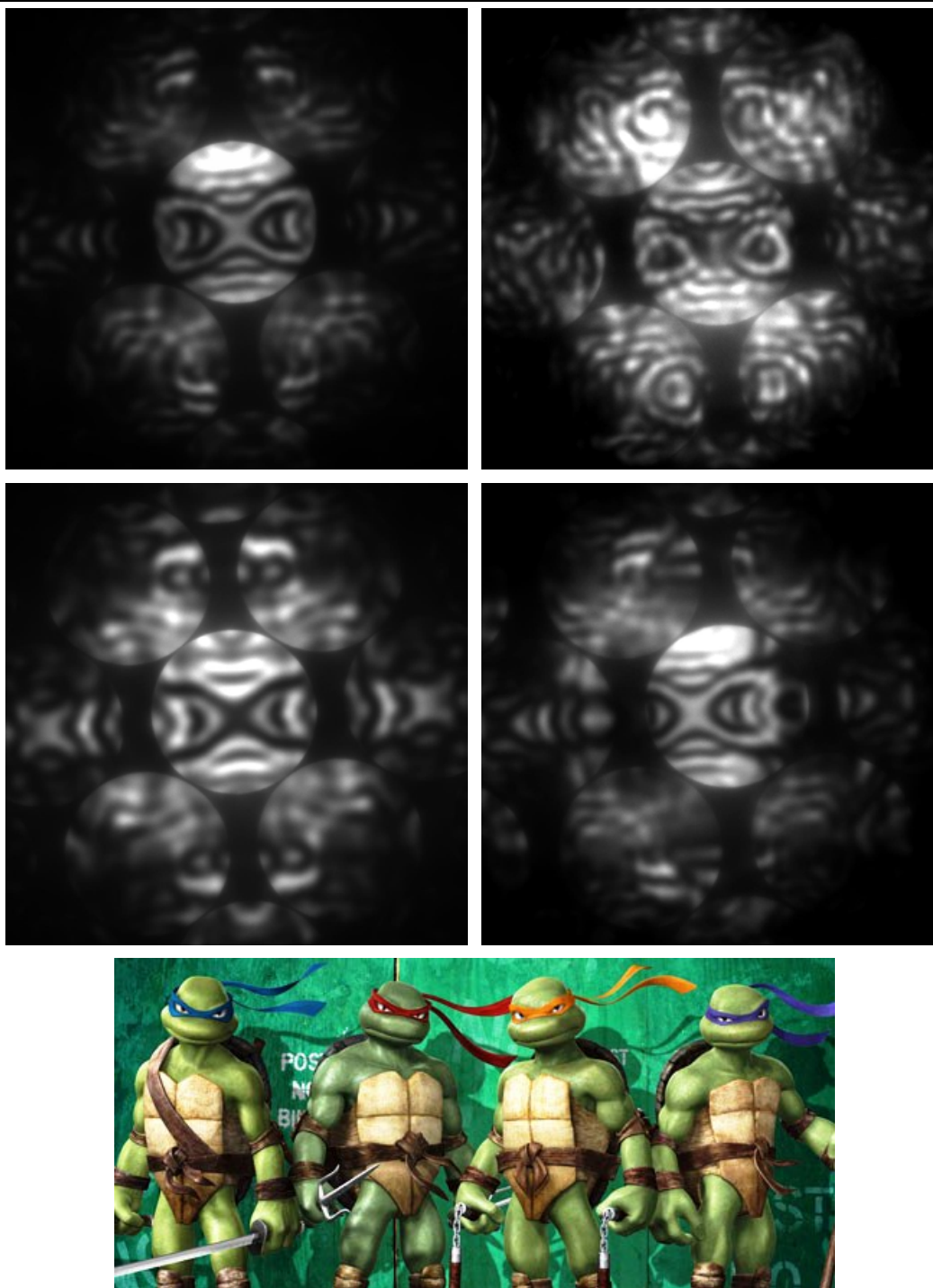
作品名稱	忍硅現身

作品內容

　　Si 試片於<110>方位照射條件下，改變試片厚度對聚束電子繞射圖形的效應。

作者姓名　吳盈瑩	單位　國立台灣大學材料科學與工程學系暨研究所、國立台灣科技大學材料科學與工程系
聯絡電話　0939445548	**E-Mail**　d00527001@ntu.edu.tw
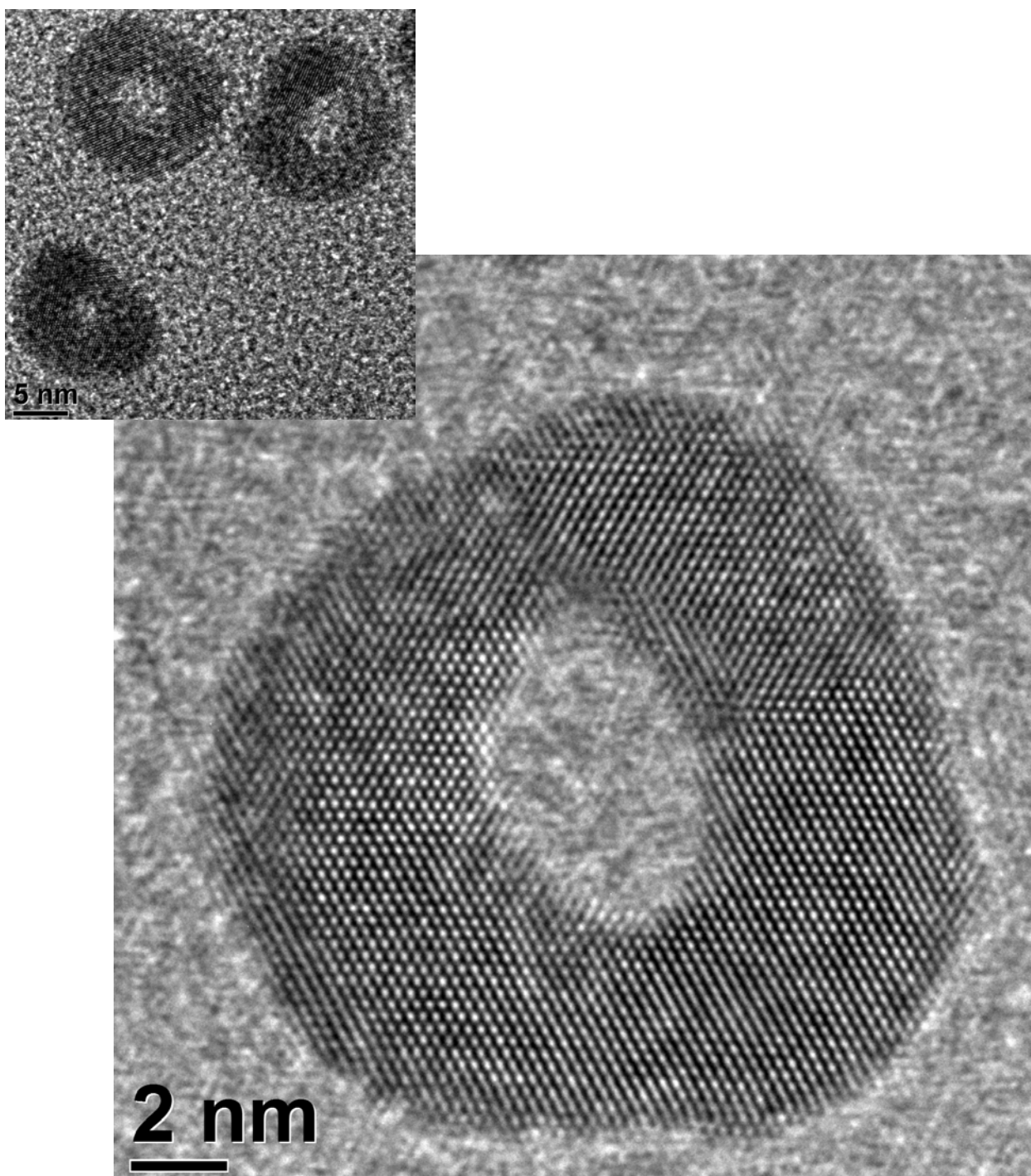
作品名稱	甜甜圈佐珍珠!

作品內容

利用高分辨電鏡影像，觀察複合金屬奈米顆粒的中空環狀結構形貌

作者姓名　吳盈瑩	**單位**　國立台灣大學材料科學與工程學系暨研究所、國立台灣科技大學材料科學與工程系
聯絡電話　0939445548	**E-Mail**　d00527001@ntu.edu.tw
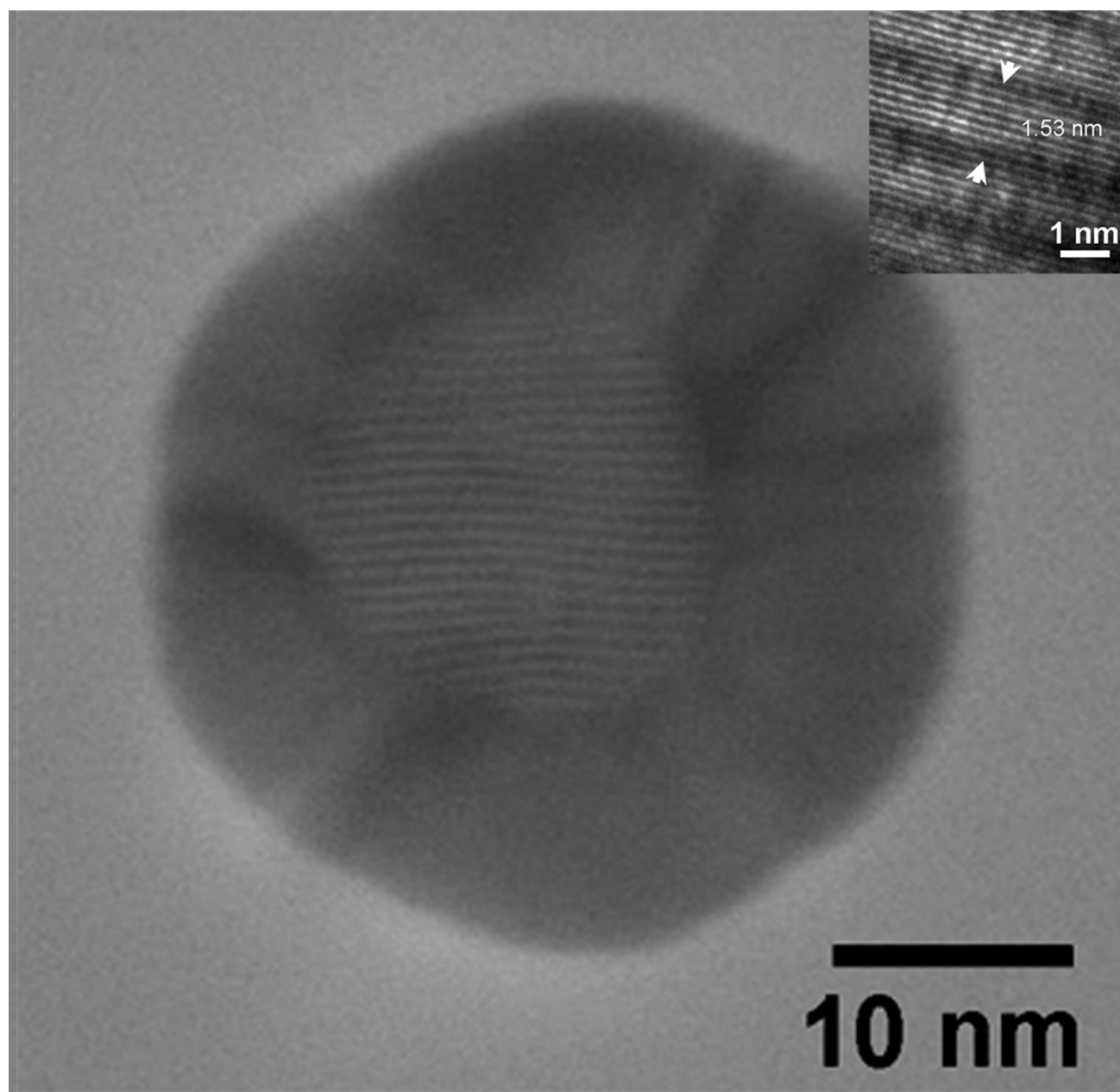
作品名稱: 火山湖上的倒影（Cu@Ag 核殼奈米顆粒之莫瑞條紋）

作品內容:

Cu@Ag 奈米顆粒核殼結構特徵產生之莫瑞條紋(moiré fringe)，宛如火山湖一般，位於中間之莫瑞條紋就像湖泊上水的漣漪抑或是天空上浮雲的倒影投射在湖泊裡。而由高解析度穿透式電子顯微鏡影像顯示，其莫瑞條紋間距為 1.53nm，驗證由 Cu 及 Ag 兩晶體重疊造成。

作者姓名: 蔡齊航 宋振銘 陳詩芸	單位:台灣科技大學應用科技研究所/中興大學材料系/台灣科技大學材料系
聯絡電話: 0912-906-903	E-Mail:d9914003@mail.ntust.edu.tw
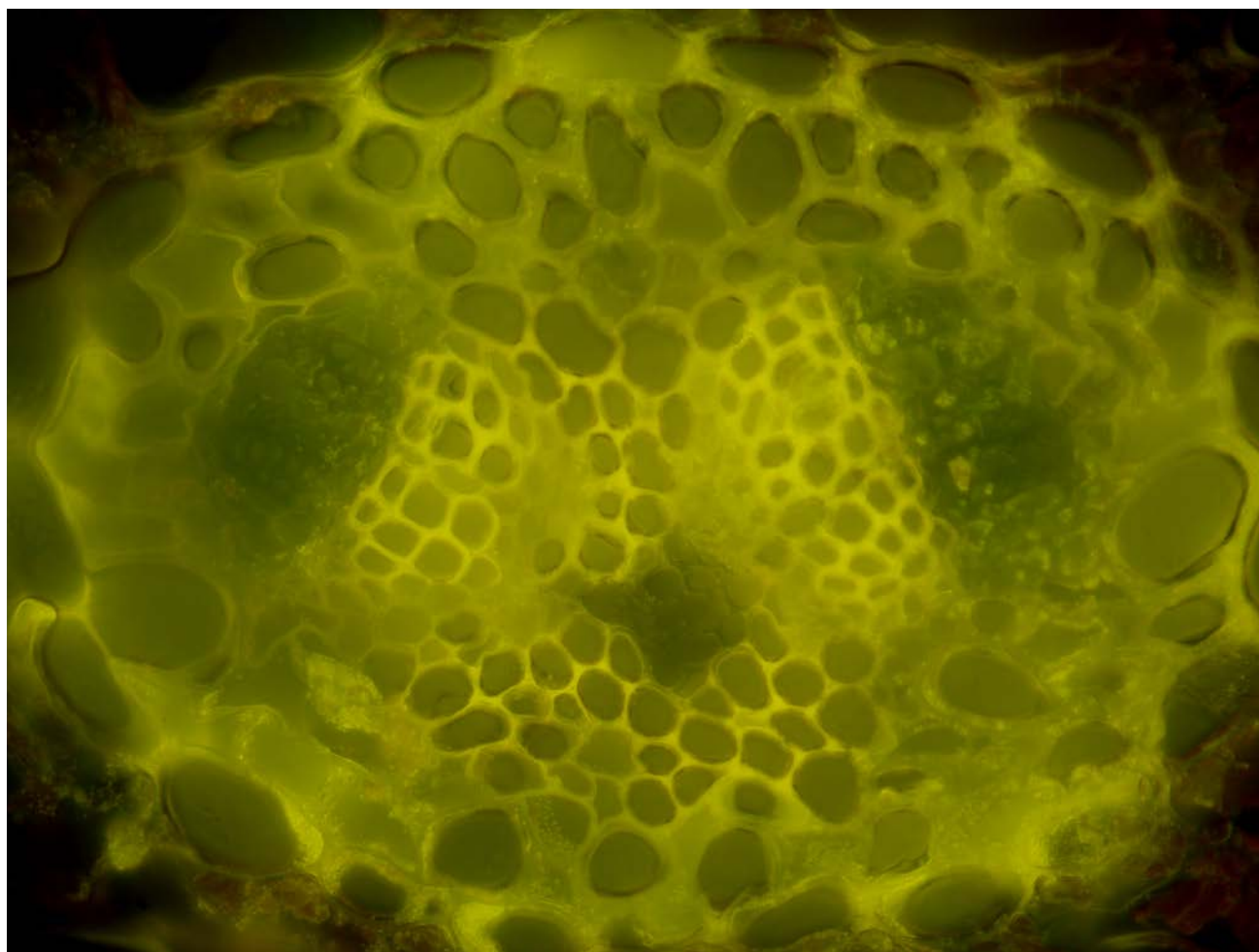
作品名稱　黃色小精靈

作品內容：圓圓的臉龐有著大大的眼睛與小巧的嘴巴，模樣十分的可愛呢！拍攝對象為馬尾松松針的維管束，眼睛部分為維管束跡、嘴巴部分為維管束內松脂管。

作者姓名　陳運萱、許秋容	單位 國立中興大學 生命科學系
聯絡電話　0928486739	E-Mail yschen32@gmail.com
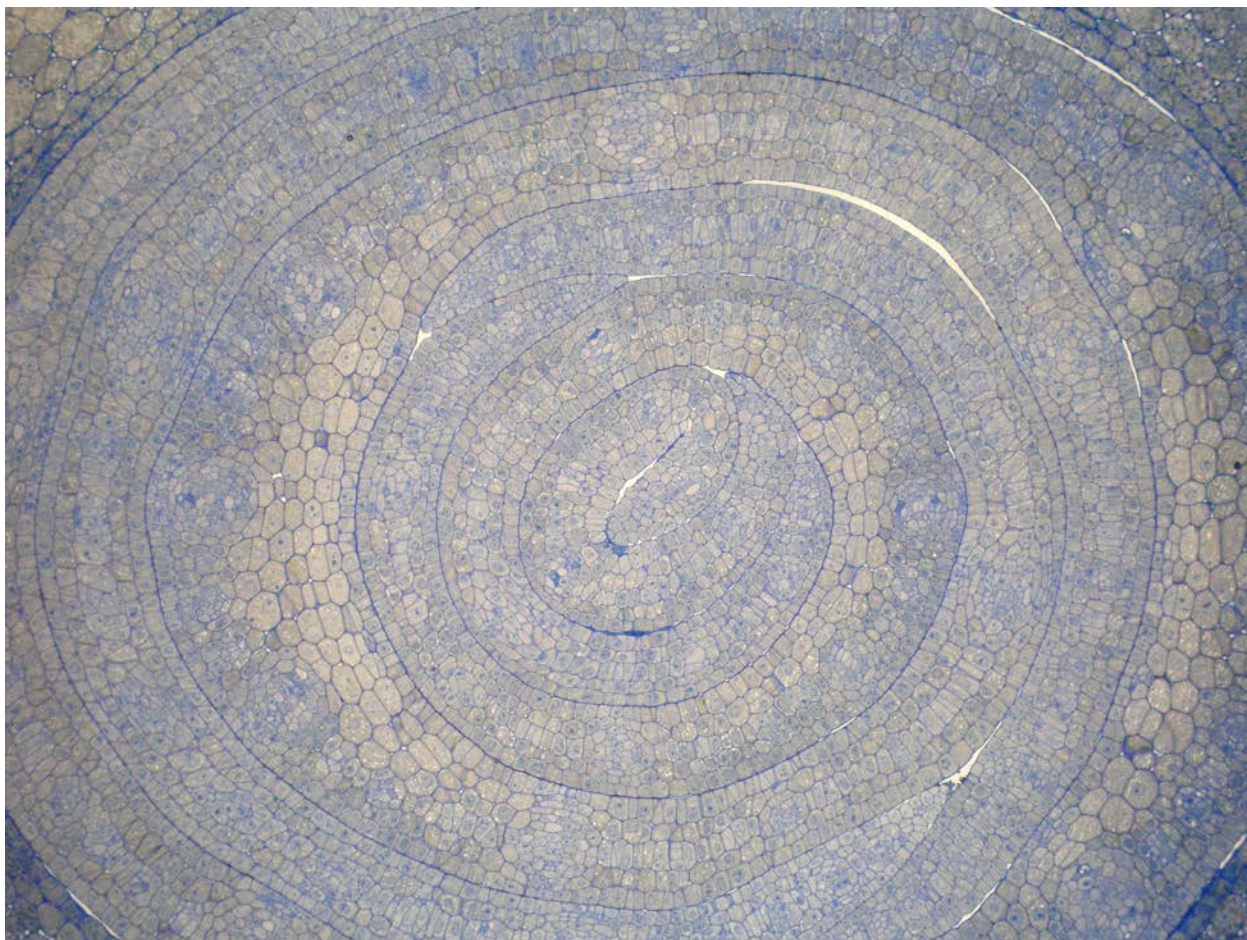
作品名稱　孕

作品內容

玉米胚的部分構造: 您知道在一顆小小的玉米粒內已經發展出 4-5 片幼葉蓄勢待發了嗎?

作者姓名　吳業華、許秋容	單位 國立中興大學 生命科學系
聯絡電話　0918135735	E-Mail ted2301636@gmail.com

作品名稱	臺灣近海超級鯨魚大發生空照圖

作品內容

臺灣近海超級鯨魚大發生？真得嗎？原來這是被你我吃下肚的柿子果肉細胞和其澱粉粒呢 (此澱粉粒似臺灣地圖)！

作者姓名 許秋容	單位 國立中興大學 生命科學系
聯絡電話 0978079776	E-Mail crsheue@gmail.com
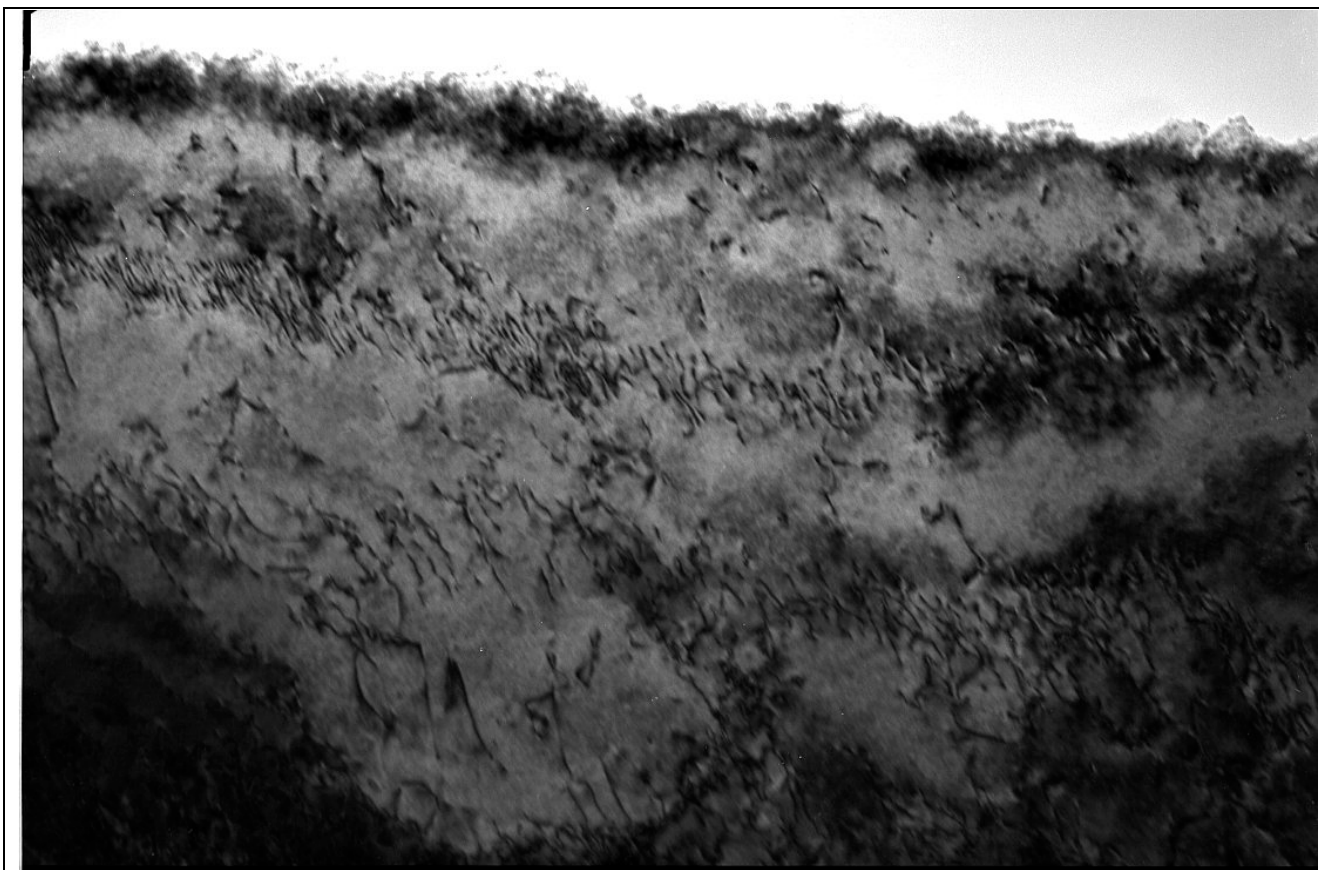
作品名稱 差排一條龍

作品內容

在肥粒鐵基地中看到整齊排列的差排

作者姓名 楊景明	**單位** 台大材料所
聯絡電話 33663748	**E-Mail** r00527047@neu.edu.tw
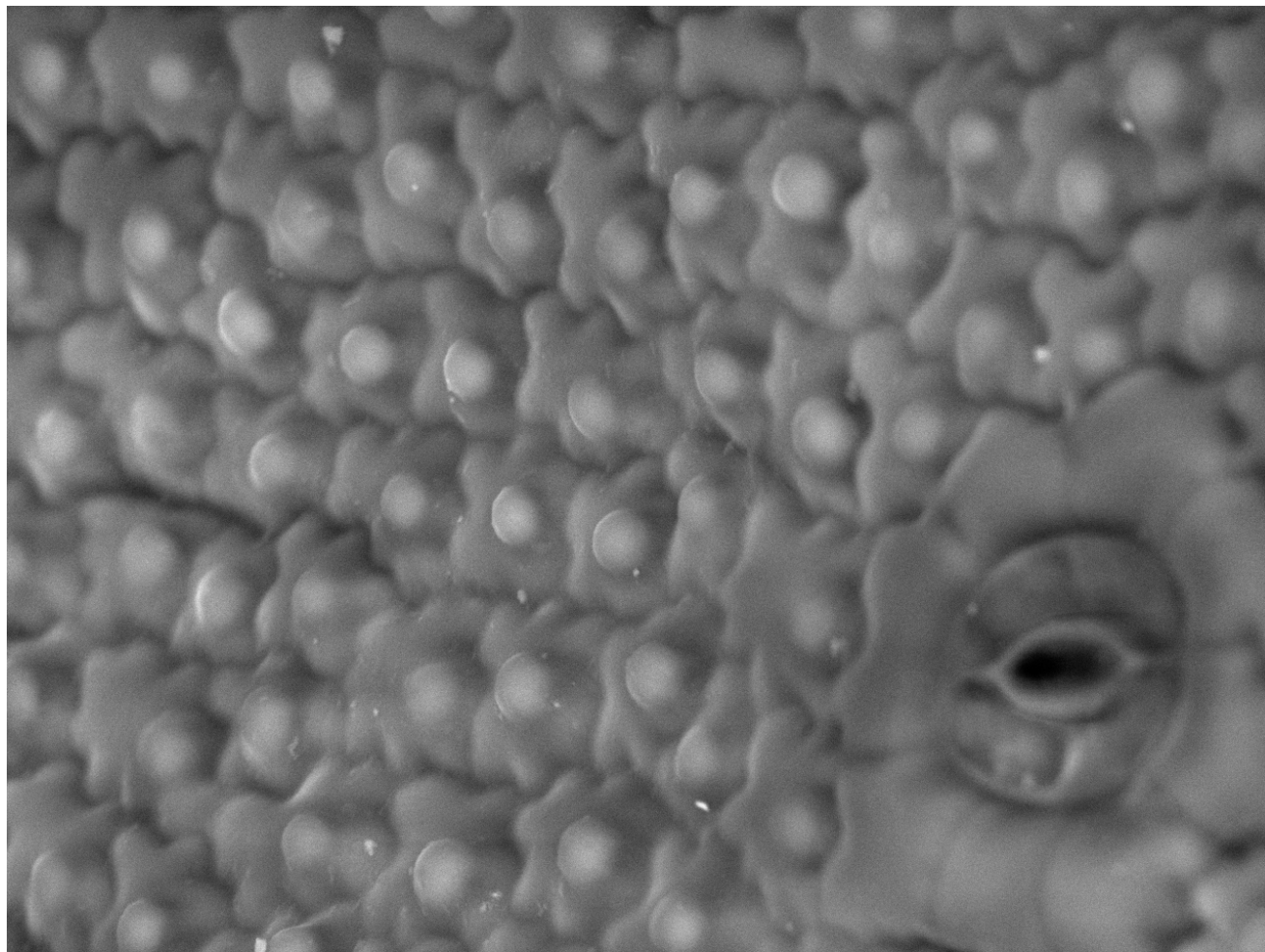
TM3000_　　　　　2013/06/21　16:17 NL　　　　x2.5k　　30 um

作品名稱	剛柔並濟

作品內容

拍攝對象為卷柏(*Selaginella*)植物的葉片表面，細胞上凸起的圓點與玻璃同為矽的氧化物，彷彿在警告膽敢來犯的敵人。

作者姓名　劉鑑緯、許秋容	單位　國立中興大學　生命科學系
聯絡電話　0918135735	E-Mail ted2301636@gmail.com
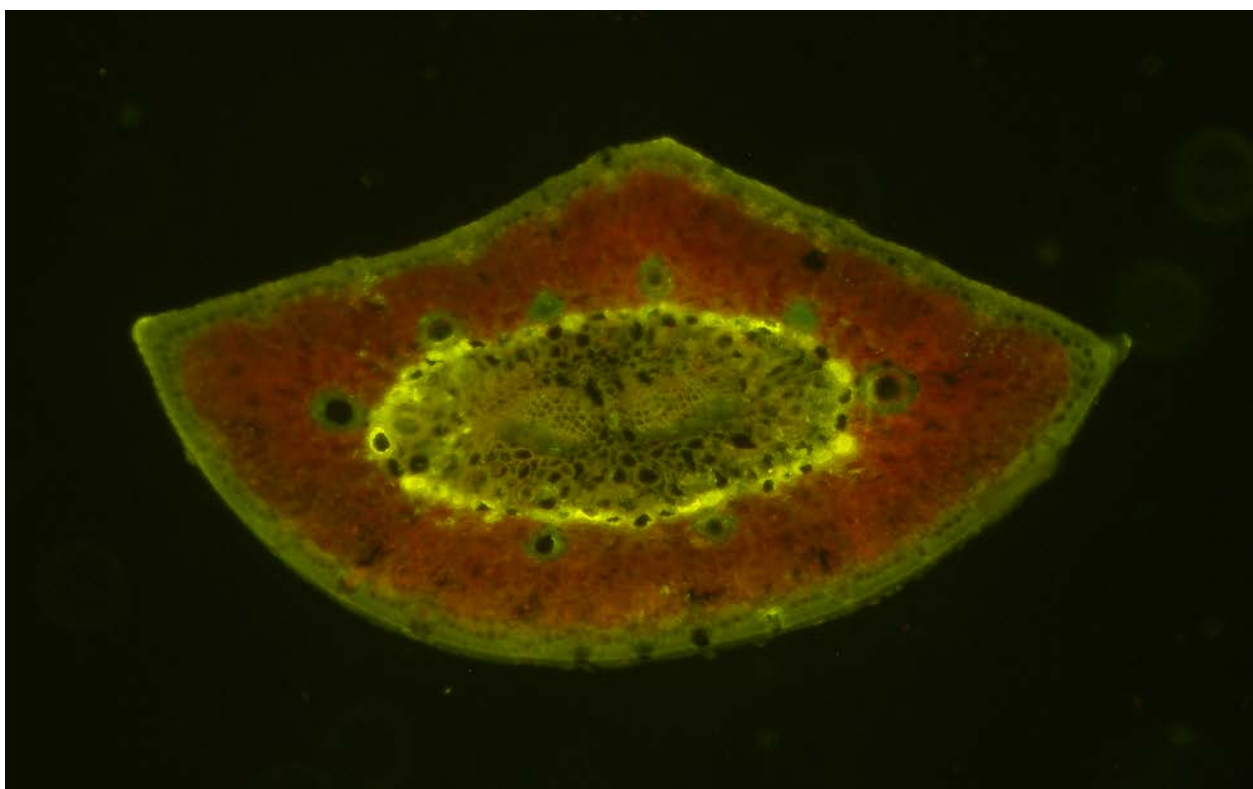
作品名稱　夏威夷比薩

作品內容

利用徒手切片與螢光顯微鏡,呈現松樹的松針橫切面,貼近畫面中間維管束的綠色圓環狀構造為其松脂管。

作者姓名　劉鑑緯、許秋容	單位　國立中興大學　生命科學系
聯絡電話　0918135735	E-Mail ted2301636@gmail.com

1 μm
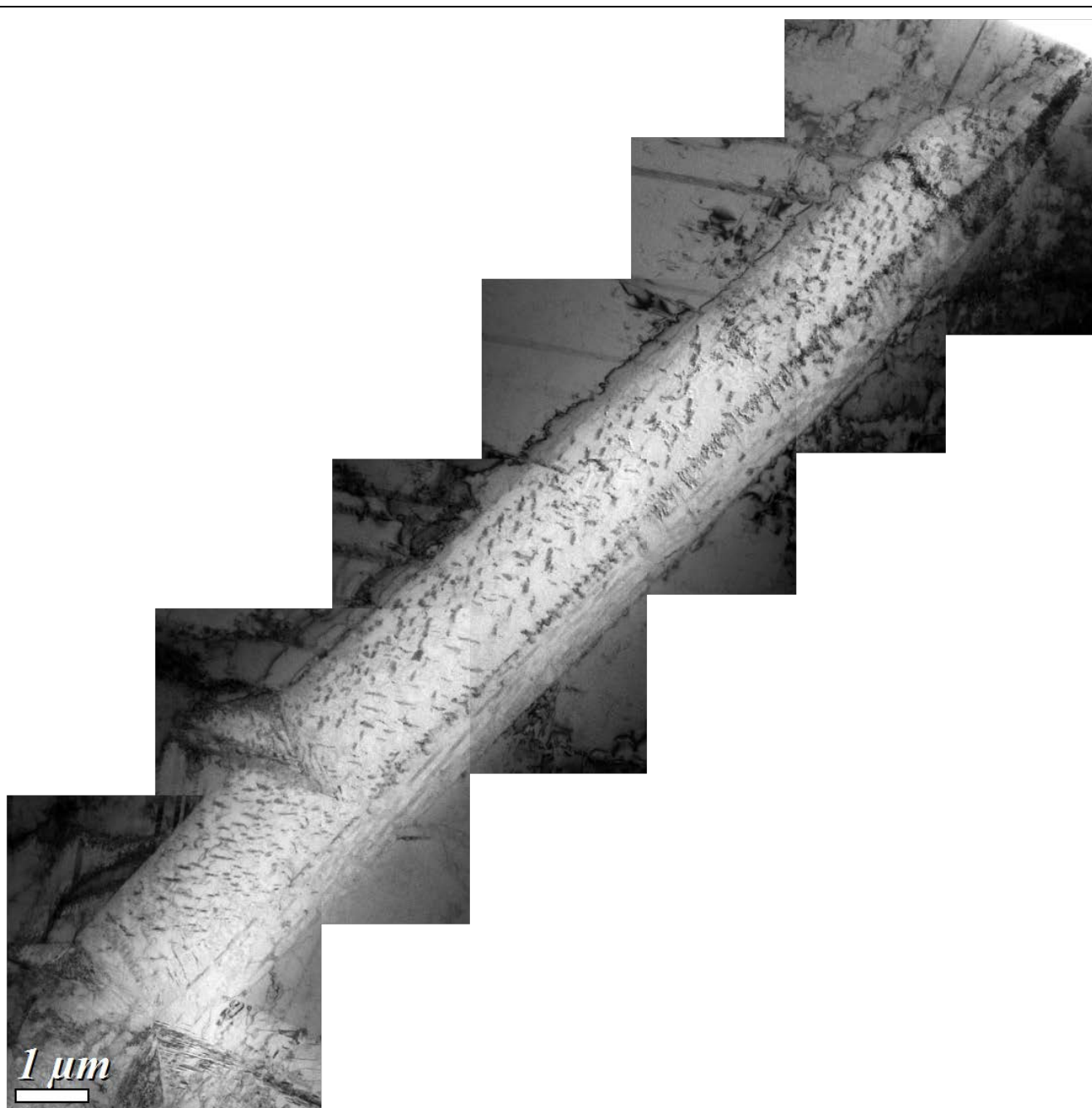
| 作品名稱 | 碳化物 |

作品內容：快壞掉的香蕉

| 作者姓名：張雅齡 | 單位：台灣大學材料科學與工程學研究所 |
| 聯絡電話：33661353 | E-Mail：d99527007@ntu.edu.tw |
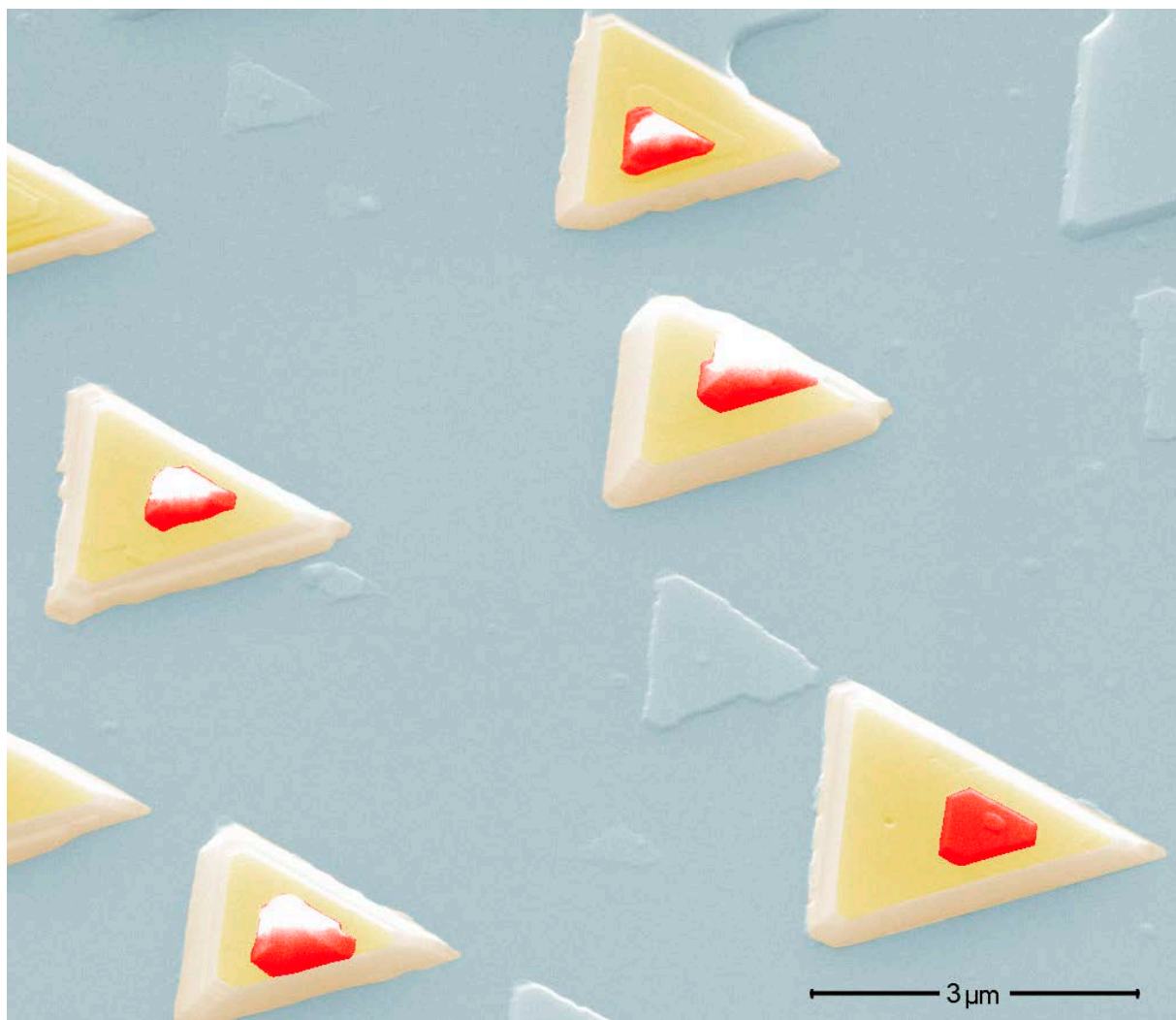
作品名稱	餓了嗎？來點 Cheese cake 吧！

作品內容

藉由金屬催化，以層狀磊晶成長，形成單晶矽奈米結構之 SEM 照片。

作者姓名 蔡昀嶧	單位　國立台灣大學材料所
聯絡電話 02-3366 3296	**E-Mail**　r01527008@ntu.edu.tw
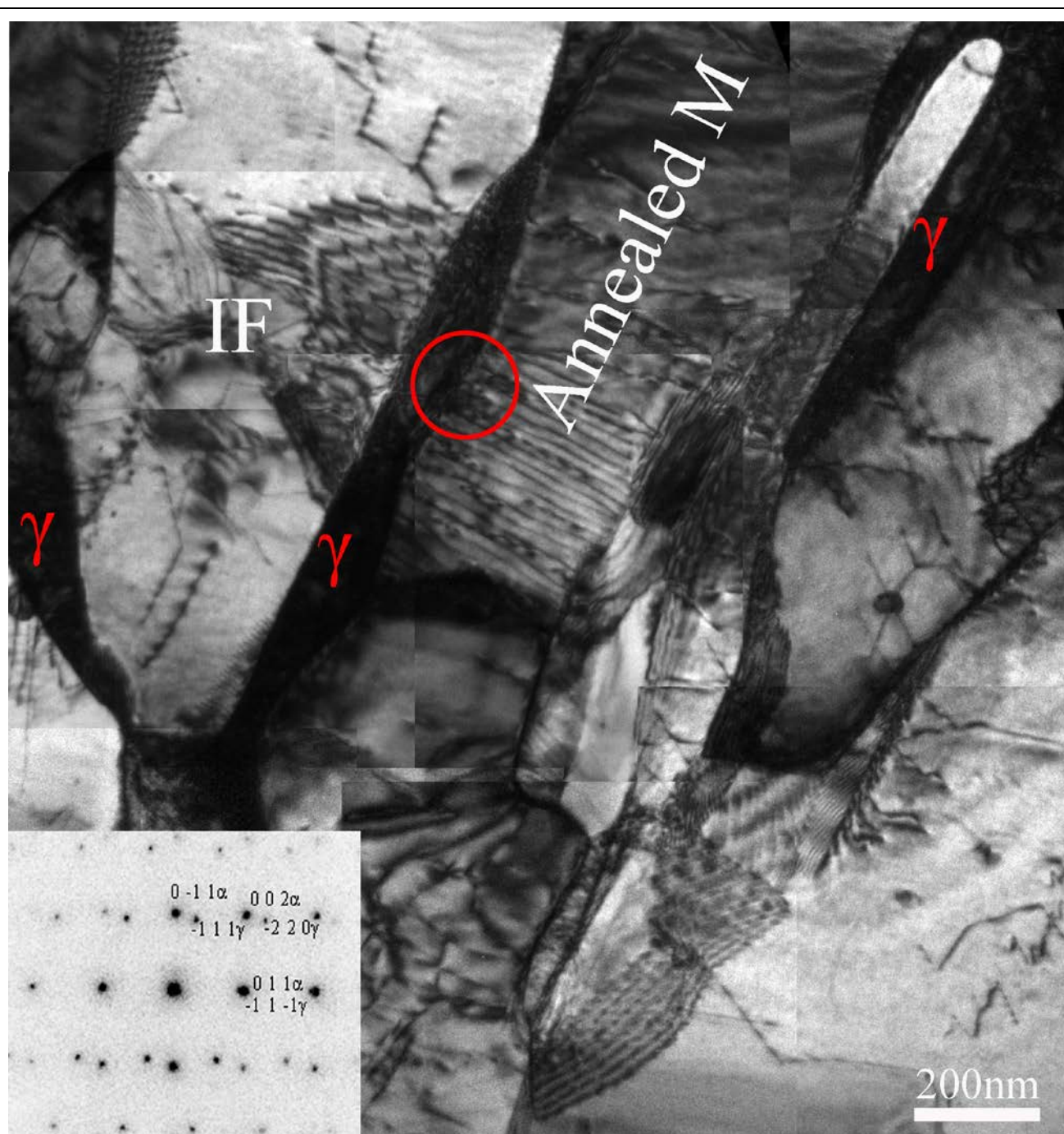
作品名稱　複相組織鋼中薄膜狀殘餘奧氏體

作品內容

薄膜狀的奧氏體在臨界鐵素體（intercritical ferrite）和退火馬氏體（annealed martensite）之間且在馬氏體中形成，其與退火馬氏體之間呈 N-W 位向關係。

作者姓名　謝振家	單位　北京科技大學
聯絡電話　+86 15652934868	E-Mail xiezj01@gmail.com
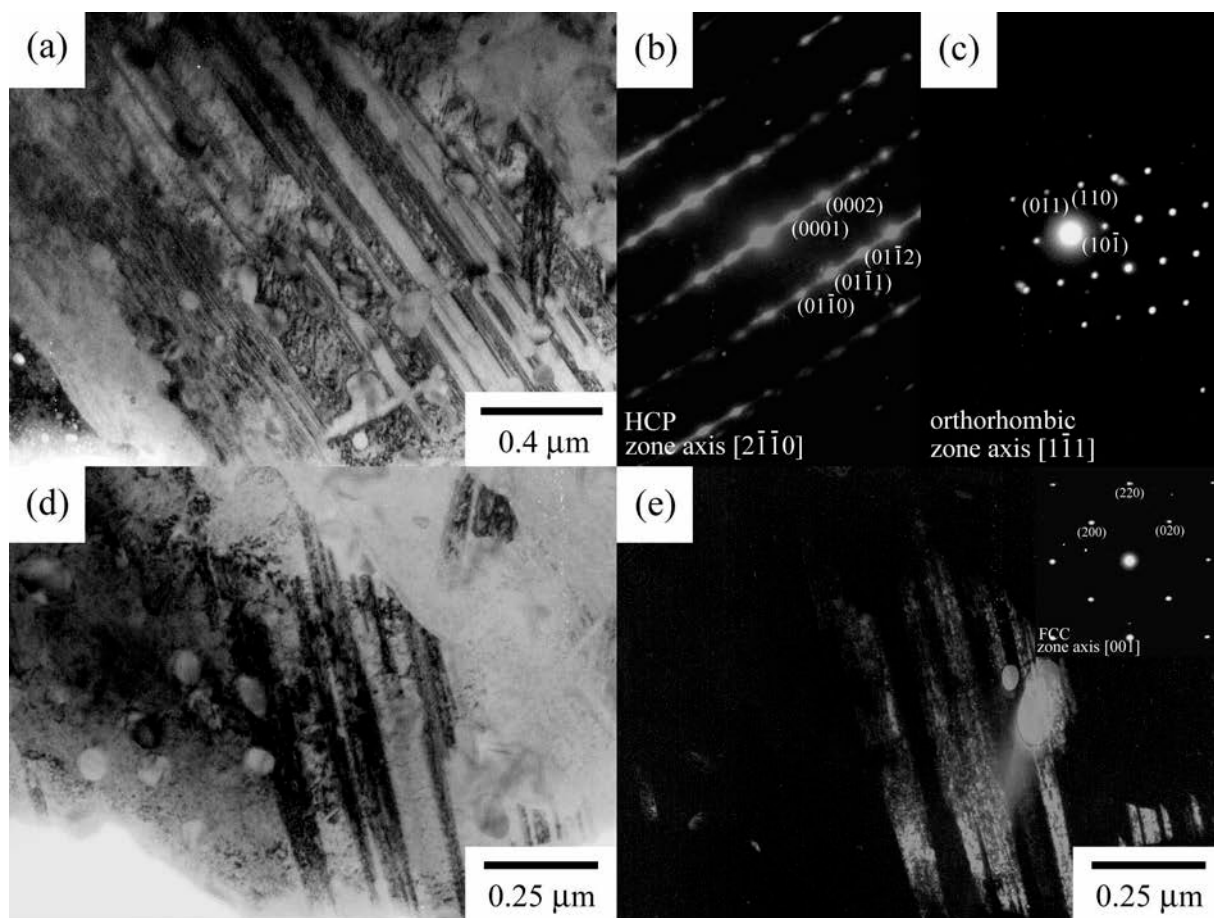
圖說明：電鍍鈷磷合金 500℃恆溫熱處理後的微結構分析：(a) HCP 結構的柱狀鈷晶粒退火雙晶明視野影像，(b)柱狀鈷晶粒退火雙晶擇區繞射圖，(c) Co_2P 析出物的擇區繞射圖，(d) FCC 結構的柱狀鈷晶粒明視野影像，(e) FCC 結構的柱狀鈷晶粒暗視野影像。

作品名稱：鈷磷合金高溫退火相變態微結構演變

作品內容：

鈷磷合金高溫退火不單只有析出硬化效益，鈷晶粒亦會有退火雙晶生成和麻田散體變態造成晶粒內部含有高密度的疊差，這類結晶缺陷都將造成結晶區塊(crystalline domain)尺寸降低，有效提升鈷磷合金高溫強度。

作者姓名：
[1,2]陳鷁澤、[1]林招松、
[2]潘永寧、[3]李春穎

單位：
[1] 臺灣大學 材料科學與工程學系
[2] 臺灣大學 機械工程學系
[3] 臺北科技大學 機械工程系

聯絡電話：0910797382；(02)33662678

E-Mail：fjuge3318@yahoo.com.tw
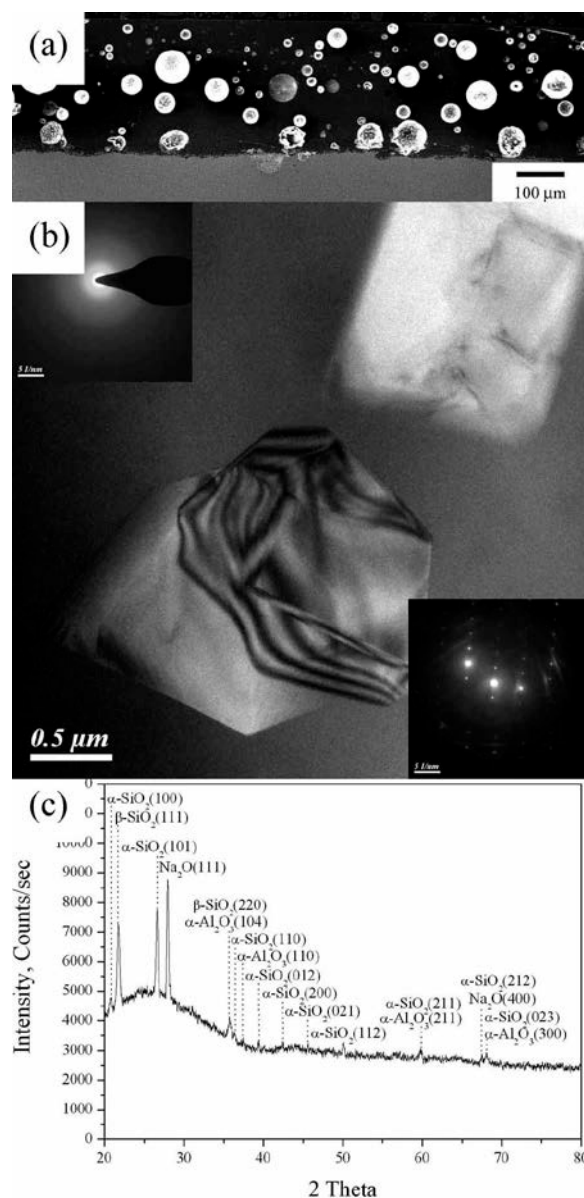
圖說明：SiO$_2$-Na$_2$O-Al$_2$O$_3$ 玻璃陶瓷複合保護塗層微結構解析：(a)複合塗層橫截面 SEM 觀察，(b)複合塗層橫截面 TEM 分析與擇區繞射圖，(c)複合塗層 XRD 結構解析與相的鑑定。

作品名稱：低熔點 SiO$_2$-Na$_2$O-Al$_2$O$_3$ 玻璃陶瓷複合塗層微結構解析

作品內容：

玻璃基塗層是指具有非晶玻璃相與結晶相共存的多晶材料複合塗層，其製作程序是熔融材料經由過冷液體急速固化形成非晶相的玻璃，再透過適當熱處理使非晶玻璃產生相分離並析出結晶質晶粒，藉以調控複合塗層的結晶量，使塗層兼具玻璃與陶瓷的複合性質。

作者姓名：陳鬝澤、林招松	單位：臺灣大學 材料科學與工程學系
聯絡電話：0910797382；(02)33662678	E-Mail：fjuge3318@yahoo.com.tw
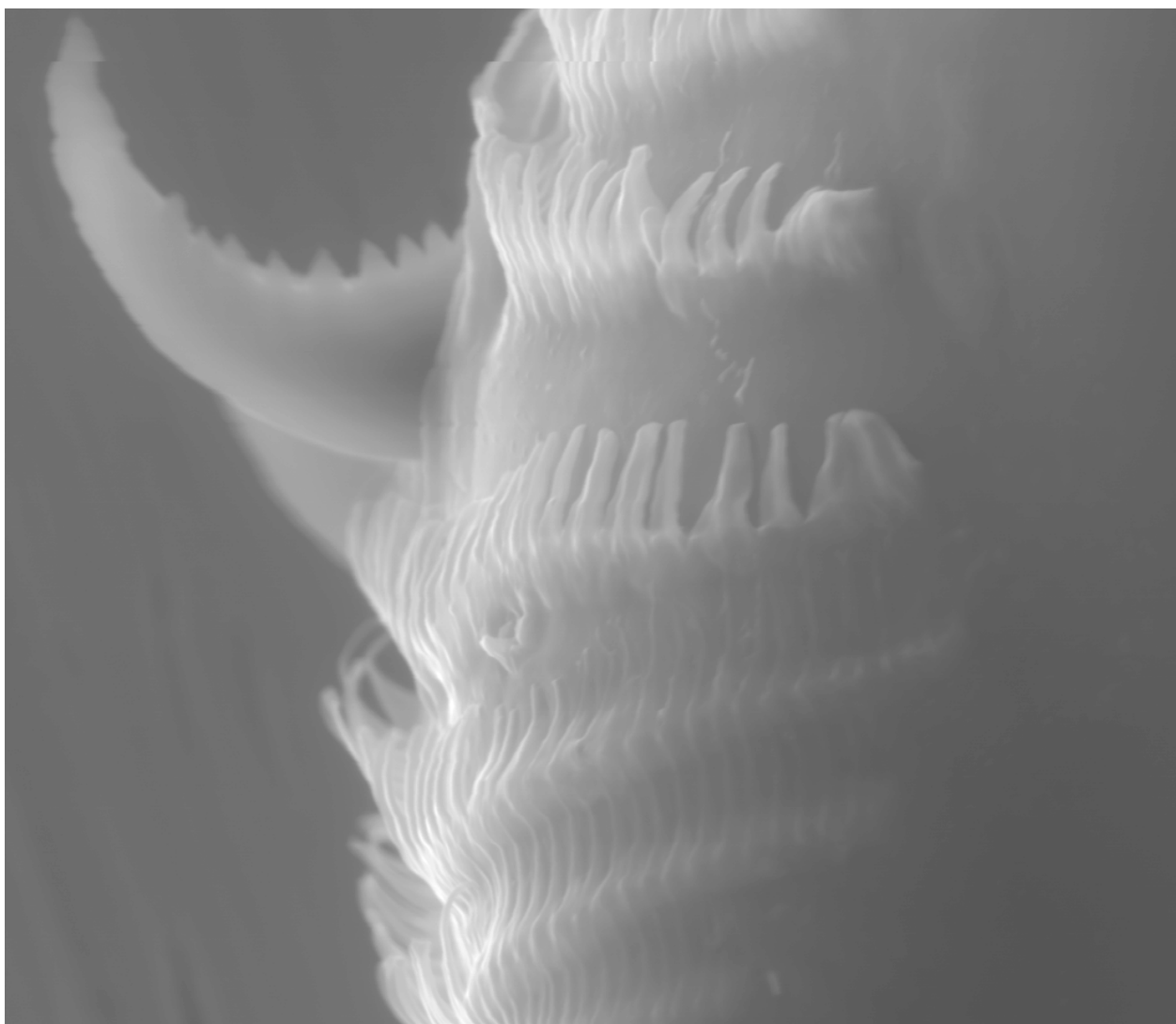
HV	Mag	WD	Spot	Pressure	Temp	20.0μm
25.0 kV	1500x	5.6 mm	6.0	6.50 Torr	10.0 ℃	

作品名稱：法國毛毛蟲的領巾

作品內容

利用 ESEM 拍攝果蠅幼蟲的進食口器影像，呈現其飽滿多汁的飽足感。

作者姓名: 李莉姿、林壯宇	單位:中央研究院細胞與個體生物學研究所
聯絡電話: 02-27899526	E-Mail: litzuli@gate.sinica.edu.tw
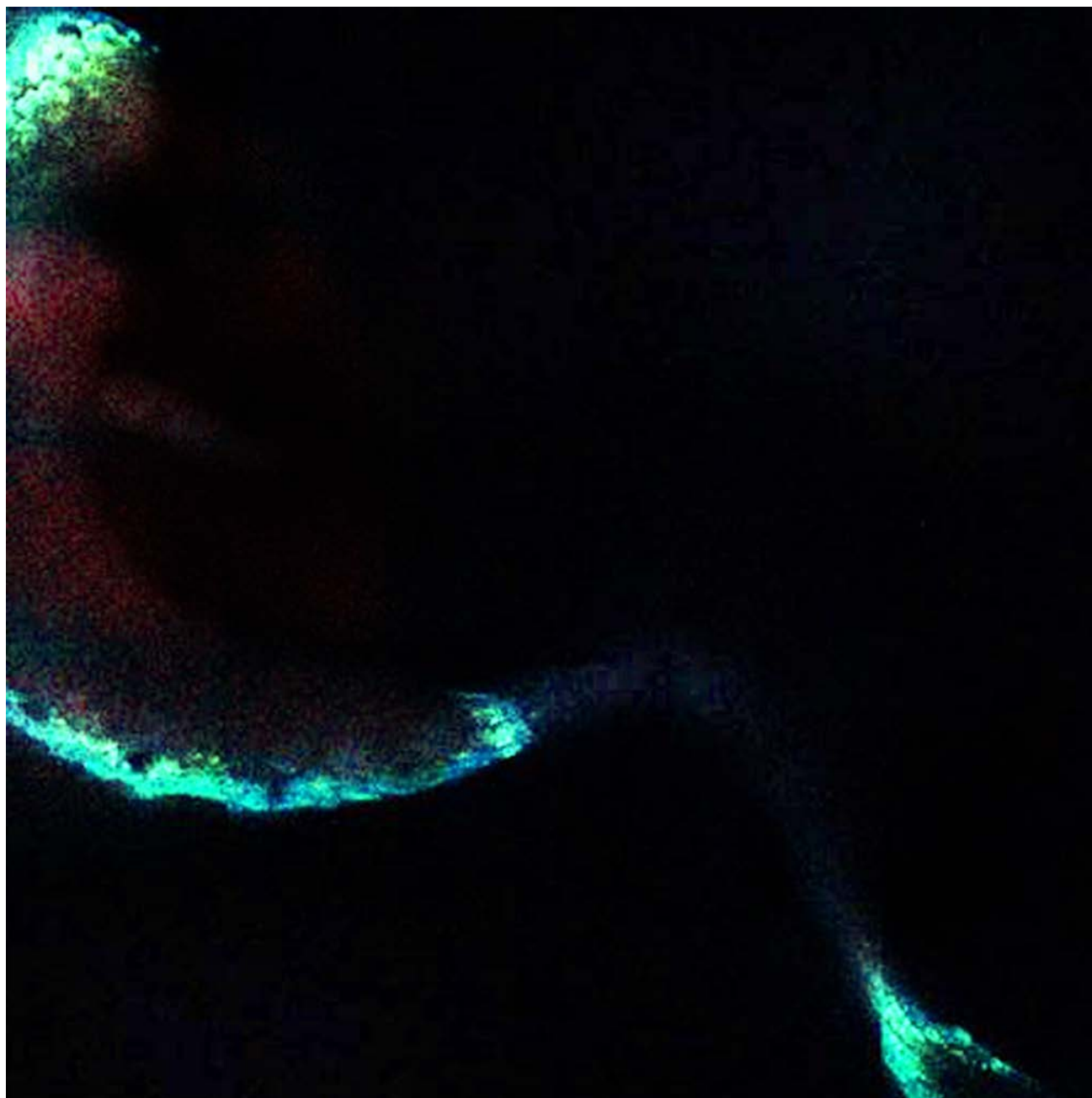
作品名稱　美人魚

作品內容

圖中為阿拉伯芥的胚乳多光子螢光影像，葉綠體的紅光勾畫出人的形貌，藍綠光的保衛細胞恰巧形成美人魚的尾部、背鰭與秀髮，末端的根部為生動的尾鰭徜徉於大海中。

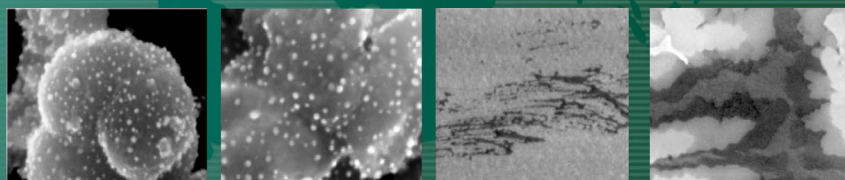| 作者姓名　蕭宇成	單位　台大應用物理研究所
聯絡電話　0921521931	E-Mail a3808625@yahoo.com.tw

NOTE

Hitachi High-Technologies
HITACHI

HITACHI High-Technology.

SU8000 Series
Ultra High Resolution FE-SEM
STEM / EDS / EBSD

Excellent imaging performance
For a wide range of application

Ultra High Resolution   **Surface Voltage contrast**

HD-2700A
Ultra High Accurate
CDM system
Cs-Corrected STEM

HF-3300
UHR-EELS
analysis system
Cold-FE-TEM

NB5000
Ultra High Speed
Milling system
FIB-SEM System

HT7700
Viewing samples at
ultra-low intensities
120kV TEM/STEM

益弘儀器股份有限公司
EH **E HONG** INSTRUMENTS CO., LTD.

台北：02-27552266　新竹：03-5782020
台中：04-22452181　台南：06-2095135
高雄：07-3340407　www.ehong.com.tw

佳佑儀器有限公司
Jia Yu Apparatus CO., LTD

服務地址：新竹市牛埔東路1-2號13樓
電話：(03)530-2385 E-mail：konica@jja.com.tw
傳真：(03)530-6186 Web：www.jja.com.tw

產品簡介

TEM/SEM/金相試片前處理設備耗材

1. 鑽石刀切割機＆砂輪刀切割機
2. 單盤＆雙盤 研磨拋光機
3. 熱鑲埋成型機
4. 冷鑲埋＆熱鑲埋 專用耗材
5. 3M研磨砂紙＆3M鑽石拋光膜
6. 拋光用氧化鋁粉＆拋光絨布
7. 鑽石刀片＆砂輪刀片
8. TEM專用銅環＆銅網系列
9. SEM專用桌上型鍍金機＆濺鍍靶材
10. TEM＆SEM試片代測服務

光學顯微鏡組＆影像擷取量測設備

1. 客製化架設CCD觀測鏡頭
2. 長工作距離光學變焦顯微鏡
3. 立體顯微鏡
4. 金相觀測光學顯微鏡
5. 三次元工具量測顯微鏡
6. 彩色＆黑白 數位式CCD（USB系統）
7. 影像擷取＆2.5D量測模組
8. LED＆鹵素光纖光源
9. 各式載物平台設計規劃

實驗室儀器＆客製化設備

1. 特殊冶具加工設計
2. ITO玻璃切割機
3. 旋轉塗佈機
4. 各類型烘箱＆管型高溫爐
5. 不鏽鋼材質手套箱
6. 電子分析天秤＆電磁加熱攪拌機
7. 實驗儀器客製化設計開發
8. 實驗室專用實驗桌＆排煙櫃體設計規劃

電性量測＆液晶量測設備

1. 四點探針量測系統／Probe Station
2. 太陽能矽晶薄膜量測系統
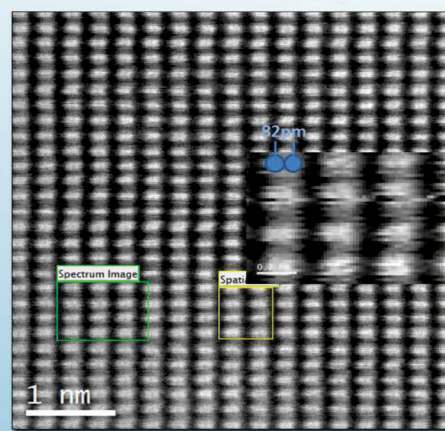3. 半導體元件電性量測系統
4. 鎢鋼探針・彈簧針桿＆訊號傳輸線材

優 惠 專案

A. 單盤研磨拋光機

B. 雙盤研磨拋光機

NTD 45,500

NTD 55,500